

DomainCQA: Crafting Knowledge-Intensive QA from Domain-Specific Charts

Yujing Lu^{1*}, Ling Zhong^{1*}, Jing Yang^{1*}, Weiming Li^{1*}, Peng Wei², Yongheng Wang¹,
Manni Duan^{1†}, Qing Zhang^{1†}

¹Zhejiang Lab, Hangzhou, China

²National Astronomical Observatories, Chinese Academy of Sciences, Beijing, China
 {luyujing, zhongling, yangjing0128, liwm, wangyh, duanmanni, qing.zhang}@zhejianglab.org,
 weipeng01@nao.cas.cn

Abstract

Chart Question Answering (CQA) evaluates Multimodal Large Language Models (MLLMs) on visual understanding and reasoning over chart data. However, existing benchmarks mostly test surface-level parsing, such as reading labels and legends, while overlooking deeper scientific reasoning. We propose DomainCQA, a framework for constructing domain-specific CQA benchmarks that emphasize both visual comprehension and knowledge-intensive reasoning. It integrates complexity-aware chart selection, multtier QA generation, and expert validation. Applied to astronomy, DomainCQA yields AstroChart, a benchmark of 1,690 QA pairs over 482 charts, exposing persistent weaknesses in fine-grained perception, numerical reasoning, and domain knowledge integration across 21 MLLMs. Fine-tuning on AstroChart improves performance across fundamental and advanced tasks. Pilot QA sets in biochemistry, economics, medicine, and social science further demonstrate DomainCQA’s generality. Together, our results establish DomainCQA as a unified pipeline for constructing and augmenting domain-specific chart reasoning benchmarks.

Code — <https://github.com/LingZhong01/DomainCQA>
Datasets —
<https://huggingface.co/datasets/yangjing0128/AstroChart>
Extended version — <https://arxiv.org/abs/2503.19498>

Introduction

The success of Multimodal Large Language Models (MLLMs) has sparked growing interest in their ability to process and analyze scientific charts, which play a crucial role in conveying complex research data (Team et al. 2024; OpenAI 2024). Among various chart-related tasks, Chart Question Answering (CQA) has emerged as a fundamental challenge, requiring MLLMs to extract, interpret, and reason about chart-based information in response to natural language queries.

Although recent benchmarks in CQA, such as ChartQA (Masry et al. 2022), PlotQA (Methani et al. 2020), CharXiv (Wang et al. 2024), and SciCap (Hsu, Giles, and Huang 2021), have greatly advanced the field, all of them are deliberately *knowledge-agnostic*. Their

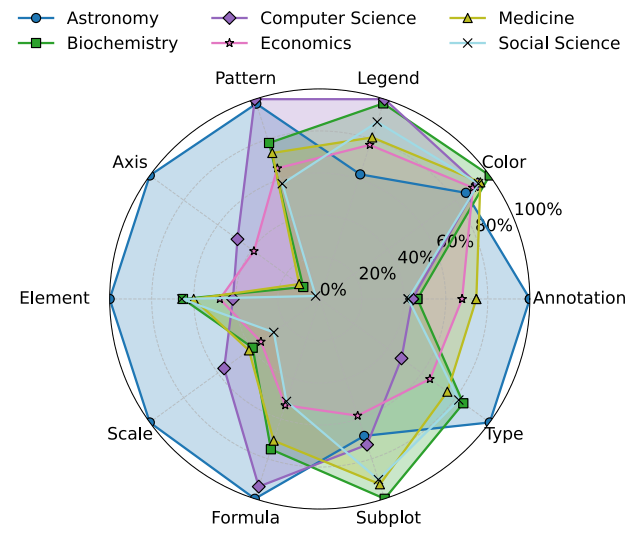


Figure 1: Radar plot of chart complexity across domains by comparing various visual design features, computed from 500 sampled charts per domain. Each axis represents a normalized design element contributing to overall chart complexity (formally defined later as the Chart Complexity Vector, or CCV). The domain-specific differences motivate our complexity-aware chart selection strategy.

question-answer (QA) pairs probe a model’s ability to parse axes, legends and visual layouts, yet never require *domain-specific reasoning*. Consequently, we still do not know whether modern MLLMs can truly integrate visual cues and scientific knowledge.

Simply extending existing benchmark-building pipelines is inadequate for two reasons: (1) **Chart selection**: current pipelines choose charts either randomly or by ad-hoc manual curation, overlooking the fact that the mix of visual elements differs sharply from one scientific field to another, as Figure 1 shows that astronomy charts emphasize annotation and formula usage, biochemistry charts lean on color and subplot, etc. In short, the charts selected in these benchmarks are *not domain-representative*; (2) **Question design**: existing CQA datasets still focus on superficial visual cues; they rarely ask questions that demand domain knowledge, for in-

*Equal contribution.

†Corresponding author.

stance, in astronomy charts correlating oscillation-frequency histograms with stellar classifications or interpreting how a redshift-magnitude scatter plot reflects cosmic expansion. In short, the questions designed in these benchmarks are *not knowledge-intensive*.

To address the two gaps identified above, we present **DomainCQA**, a framework for building domain-specific CQA benchmarks that integrates chart selection, QA generation, and expert QA validation into one seamless process. We encode each candidate chart with a 10-dimensional *Chart Complexity Vector (CCV)* and apply non-parametric Gibbs sampling to select the subset of charts used for questions that test basic understanding. For domain knowledge probing, we propose a chart abstract selector using chain-of-thought (CoT) reasoning to identify the most representative chart, along with a voting validator that enhances robustness through cross-model majority voting. Across both chart pools, we construct two tiers of QA: *Fundamental QA (FQA)* and *Advanced QA (AQA)*, and pass every QA pair through a multi-stage human review. The resulting benchmark is both domain-representative in its visuals and genuinely knowledge-intensive in its questions.

As a concrete application of DomainCQA, we construct **AstroChart**, the first CQA benchmark for astronomy. Leveraging our pipeline, we select 482 representative charts and generate 1,690 QA pairs. Of these, 1,509 are FQA pairs that test the understanding of the chart itself, while 181 are AQA pairs that require extra astronomical knowledge beyond the chart. Evaluating 21 state-of-the-art MLLMs on AstroChart exposes three persistent weaknesses: (i) chart reasoning – inferring trends and relationships from visual encodings; (ii) numerical computation – extracting values and performing arithmetic reliably; and (iii) domain-fact integration – combining chart evidence with astronomy-specific knowledge. Fine-tuning these models on data generated by DomainCQA yields notable gains, confirming the framework’s value for both evaluation and data creation.

Beyond astronomy, we create pilot sets in biochemistry, economics, medicine and social science, each with domain specific charts and QA pairs showing that DomainCQA generalizes well across disciplines. These results confirm that the framework effectively addresses the two key gaps: selecting representative charts and generating knowledge-intensive questions.

Our key contributions are as follows: (1) DomainCQA, a three-phase framework for building domain-specific CQA benchmarks; (2) CCV, a 10-dimensional descriptor that captures domain-dependent visual traits and guides chart selection; (3) Chart abstracts, defined as charts summarizing articles’ main findings, are ideal anchors for knowledge-intensive question generation; (4) AstroChart, the first CQA benchmark for astronomy; we evaluate 21 state-of-the-art (SOTA) MLLMs in zero-shot and fine-tuned settings to probe their domain-specific chart understanding.

Related Work

MLLMs for Chart Understanding Recent progress in MLLMs has substantially advanced chart understanding. Proprietary models such as GPT-4o (OpenAI 2024), Claude

3.5 (Anthropic 2024), Qwen-VL (Qwen Team 2023), and Gemini-2.5 (Google 2025) have demonstrated strong multimodal reasoning capabilities. Meanwhile, open-source MLLMs are rapidly evolving, offering accessible and customizable alternatives. Many models primarily focus on enhancing general vision-language ability through improved alignment, stronger representations, and more efficient inference, which improves performance on chart-related tasks. Notable examples include LLaVA (Liu et al. 2023b, 2024c,d), mPLUG-Owl (Ye et al. 2023a,b, 2024), SPHINX (Liu et al. 2024a), InternVL (Dong et al. 2024), CogVLM (Zhipu AI 2024), MiniCPM (OpenBMB 2024), and Pixtral (Mistral AI 2024a). In contrast, other models are specifically fine-tuned on chart-related tasks to better support structured data understanding, such as UniChart (Masry et al. 2023), Matcha (Liu et al. 2023a), ChartAssistant (Meng et al. 2024), and TinyChart (Zhang et al. 2024).

Benchmarks for CQA Evaluation A CQA benchmark consists of two key components: charts and corresponding QA pairs, both essential for evaluating a model’s chart comprehension capabilities (Huang et al. 2025). Early datasets like DVQA (Kafle et al. 2018) and FigureQA (Kahou et al. 2018) utilized synthetic charts alongside templated QA pairs, whereas later efforts such as PlotQA (Methani et al. 2020), LEAF-QA (Chaudhry et al. 2020), and LEAF-QA++(Singh and Shekhar 2020) incorporated real numerical data with synthetic visualizations. More recent benchmarks, such as ChartQA(Masry et al. 2022), OpenCQA (Kantharaj et al. 2022), and MMC-Benchmark (Liu et al. 2024b), introduced charts sourced from real-world datasets. Among these, OpenCQA pioneered open-ended CQA tasks. The growing capabilities of LLMs have enabled recent studies such as Sci-GraphQA(Li and Tajbakhsh 2023), ChartX(Xia et al. 2025), and CharXiv(Wang et al. 2024) to generate more diverse QA pairs. Nevertheless, existing benchmarks mainly focus on general or broad scientific domains and lack the domain-specific focus required for detailed chart interpretation.

DomainCQA Framework

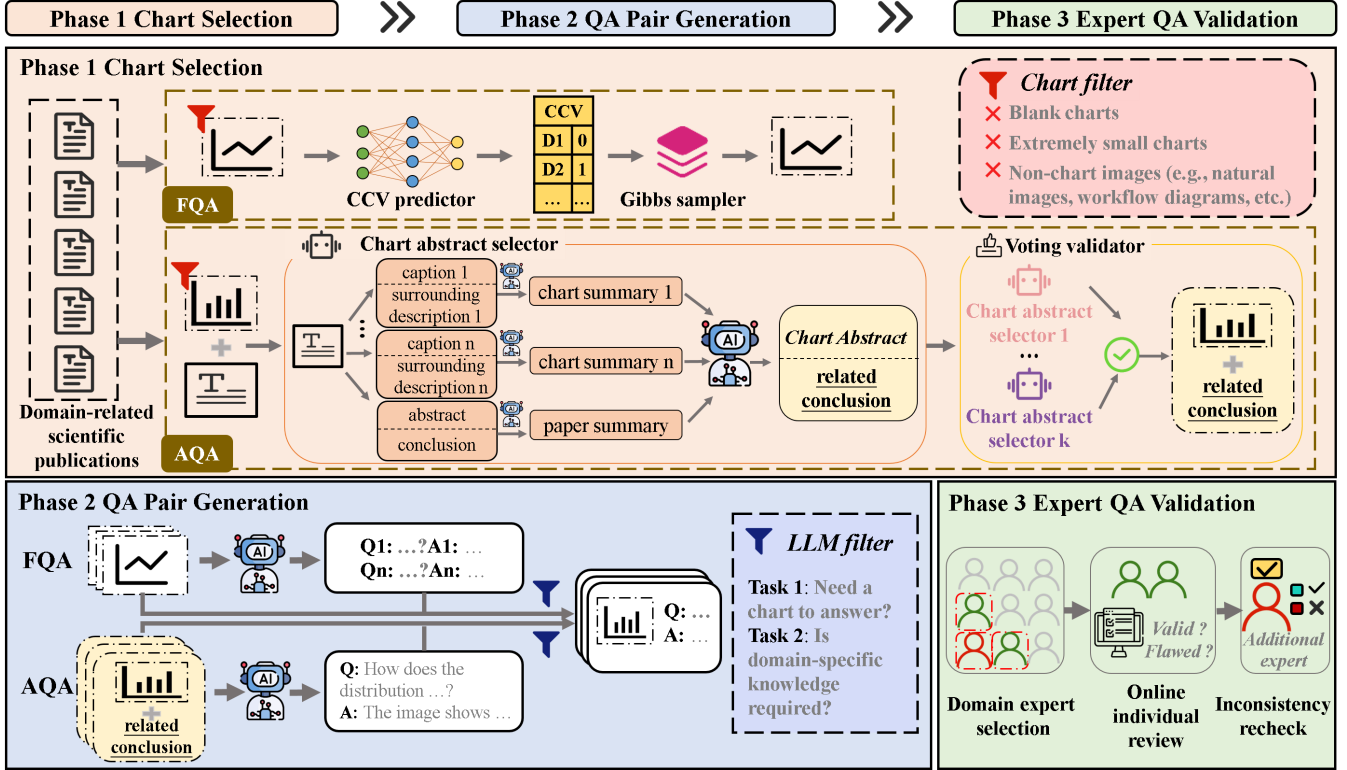
DomainCQA (see Figure 2) offers a systematic framework to build domain-specific CQA benchmarks that test both general visual understanding and specialized reasoning. It defines two types of QA tasks:

- **Fundamental QA (FQA):** testing chart comprehension via basic visual reasoning like label recognition, color differentiation, and simple comparisons.
- **Advanced QA (AQA):** requiring domain knowledge beyond the chart, including interpreting specialized symbols, terms, or concepts.

Together, questions from both tasks enable the benchmark to evaluate chart understanding across a spectrum from surface-level comprehension to discipline-specific insight.

Chart Selection

DomainCQA selects the charts separately for the FQA pairs and the AQA pairs, ensuring that each set is aligned with the specific evaluation requirements of its type of question.



Charts for FQA Our goal is to build an FQA-chart pool whose visual variety matches the unknown, true distribution of charts in a scientific domain. We operate on a pre-compiled corpus of domain charts and focus on two ingredients: a Chart Complexity Vector (CCV) that embeds each chart in a ten-dimensional feature space, and a non-parametric Gibbs sampler that draws a subset whose joint CCV statistics closely match those of the corpus.

Each CCV dimension measures a distinct aspect of visual difficulty, such as plot elements, color diversity, annotation density, and visual clutter. We train a ResNet-50 classifier on an annotated subset to predict the ten CCV attributes for the remaining charts, yielding 10-dimensional representations that capture domain-specific patterns (see Appendix A for more details on CCV).

Random sampling disregards the structured distribution of visual complexity within each domain, producing samples that do not faithfully reflect domain-specific patterns. Instead, we treat the CCV collection as an empirical distribution and perform non-parametric Gibbs sampling (Casella and George 1992) to preserve marginal distributions and inter-dimensional dependencies (see Appendix B for the Gibbs sampling pseudocode).

Let $\mathcal{C} = \{\mathbf{c}^{(1)}, \dots, \mathbf{c}^{(N)}\} \subset \mathbb{R}^{10}$ be the set of CCV vectors for all candidate charts. Each $\mathbf{c}^{(n)} = (c_1^{(n)}, \dots, c_{10}^{(n)})$ encodes the visual, structural, and interpretive attributes of a

chart. At each iteration t , we:

1. Randomly choose a dimension $k_t \in \{1, \dots, 10\}$;
2. Sample a target value $\zeta \sim \hat{p}_{k_t}$, the empirical marginal distribution of dimension k_t ;
3. Search for a new chart $\mathbf{c}^{(t)} \in \mathcal{C}$ that best matches the current state $\mathbf{c}^{(t-1)}$ on the remaining 9 dimensions and is closest to ζ in dimension k_t .

The resulting chart subset approximates the latent domain distribution in CCV space and serves as our FQA chart pool.

Charts for AQA Selecting charts for AQA requires more than visual diversity, instead it demands charts that meaningfully reflect domain knowledge. A naive approach would be to reuse charts from the FQA set and pose domain-specific questions on them. However, this often results in noisy inputs that dilute question quality. Many visually complex charts are tangentially related to the paper’s core findings, making them poor candidates for knowledge-intensive tasks.

We address this by targeting a chart that directly reflects a paper’s main scientific conclusions, commonly referred to as *chart abstract*. To identify them, we design a lightweight two-stage LLM-based method: a *chart abstract selector* that leverages CoT to identify the chart most relevant to a paper’s abstract and conclusion, and a *voting validator*, which aggregates reasoning outputs from multiple LLMs via cross-model majority voting to enhance selection reliability (see

Appendix C for the pseudocode of AQA chart selection).

This approach yields semantically meaningful charts that support deeper reasoning, as demonstrated by our later experiments across five scientific domains (see Sec. 5.5). QA pairs constructed from chart abstracts consistently outperform those from our FQA method in both domain relevance and QA validity.

QA Pair Generation

From selected charts, we design two types of questions: FQA and AQA. FQA covers four categories of tasks: *Visual* (recognizing graphical elements), *Data* (retrieving and computing values), *Inference* (inferring patterns and relations), and *Chart Description* (summarizing the visual content). AQA is formulated as a knowledge-based inference (*KB-Inference*) task, requiring integration of external scientific knowledge with visual content.

To ensure quality, we apply a secondary LLM-based validation filter to all generated QA pairs. This verifier checks two key criteria: (1) whether the QA pair is grounded in the visual content of the chart, and (2) for AQA, whether it requires domain-specific knowledge to answer (see Appendices D and E for prompt templates and validation criteria.)

Expert QA Validation

To ensure benchmark quality, each QA pair undergoes expert review to validate both its clarity and factual correctness. Reviewers label each item as either: *Valid* (the question is well-posed and the answer is accurate); *Flawed* (the question is ambiguous, misleading, or the answer is incorrect). All QA pairs are independently assessed by domain experts. Disagreements are resolved through additional review rounds until consensus is reached.

AstroChart: A Benchmark for Astronomy

We present a complete benchmark instantiation, AstroChart, in the astronomy domain, comprising 1,690 QA pairs grounded in 482 charts. We also conducted partial experiments in other domains to validate key steps, chart selection and QA pair generation for AQA, as detailed in Evaluation.

Chart Selection To construct the FQA chart portion of AstroChart, we collected figures from arXiv astronomy papers published between 2007 and 2023. A ResNet-18 classifier, trained to detect non-scientific or low-quality visuals, was used to filter out irrelevant figures. For each remaining chart, we computed its CCV and applied non-parametric Gibbs sampling to select 305 charts whose CCV distribution approximates the overall domain distribution, ensuring a diverse and representative subset.

To assess the representativeness of our selected charts, we further compared the visual complexity of AstroChart with existing CQA benchmarks. Specifically, we computed the CCV for each chart in several public datasets (CharXiv, ChartQA, OpenCQA, PlotQA), and summed the ten CCV dimensions to obtain an overall complexity score. As illustrated in Figure 3, the charts in these benchmarks are mainly

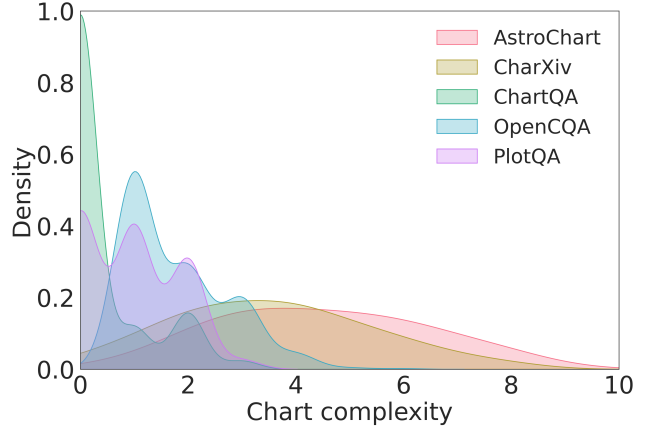


Figure 3: Chart complexity calculated from CCVs across benchmarks, where AstroChart shows a broader and higher complexity distribution than other benchmarks, with more domain-specific charts in the 6–10 range (see Appendix A.2 for CCV score details).

clustered in the 1 to 4 range, indicating simple visual structures. In contrast, AstroChart centers around 4 to 6 and exhibits a broader spread across the complexity spectrum. This suggests that AstroChart offers richer and more varied visual content, better aligned with real-world scientific charts.

For AQA, we targeted the high-impact literature by selecting the top 1% most-cited articles each year in the six main subfields of astronomy (See Appendix F). After applying the same filtering process, we identify *chart abstracts* using a consensus-based approach from GPT-4o and Claude 3.5. This results in 178 high-quality charts suitable for domain-specific reasoning.

In total, AstroChart includes 482 distinct charts with one in both (see Appendix G for visualizations).

QA Pair Generation We employ Claude 3.5 to generate QA pairs using category-specific prompts, ensuring that each question is well aligned with its associated chart. To refine quality, GPT-4o is used to automatically filter out QA pairs that either lack a clear connection to the chart or do not require external domain knowledge for answering.

We further assessed the reliability of GPT-4o’s filtering by comparing its judgments against human annotations on 200 randomly sampled QA pairs. Beyond achieving 96.5% overall accuracy, GPT-4o demonstrated substantial agreement with human reviewers, with a Cohen’s Kappa (Cohen 1960) of 0.77, indicating strong consistency in identifying deletable items. Most discrepancies were conservative false positives, underscoring GPT-4o’s cautious filtering style and practical reliability at scale (see Appendix H for details).

The final dataset comprises 1,690 QA pairs, including 1,509 FQA pairs and 181 AQA pairs, as summarized in Table 1 (see Appendix I for examples).

Expert QA Validation We conducted a comprehensive verification of the entire AstroChart benchmark to ensure its accuracy and reliability. A team of eight astronomy ex-

Type	Category	Aspect	Count
FQA	Visual	Color	211
		Style	133
		Text	213
		Layout	45
FQA	Data	Point	130
		Interval	102
		Calculation	84
AQA	Inference		289
	Chart Description		302
	KB-Inference		181
Total			1690

Table 1: Distribution of question types in AstroChart

perts independently reviewed all 1,690 QA pairs using our custom online assessment platform, with a total annotation time exceeding 160 hours. Each pair of QAs was evaluated by two randomly assigned reviewers and any disagreements were resolved through additional review rounds until consensus was reached (details in Appendix J). This rigorous expert validation process reinforces the credibility of AstroChart as a high-quality benchmark for evaluating MLLMs in astronomical chart understanding.

Evaluation

To assess the utility and difficulty of AstroChart, we design three experiments. First, we benchmark 21 SOTA MLLMs under a zero-shot setting to assess their capabilities across question categories. Second, we construct a training set using the same pipeline as AstroChart (excluding expert validation), fine-tune a representative model, and test its performance on both AstroChart and other benchmarks to assess generalization. Third, we compare AstroChart with CharXiv to evaluate relative difficulty. Finally, we also verify that the DomainCQA framework can produce high-quality AQA pairs in other scientific domains.

Setup and Metrics

Zero-Shot Setup We evaluated 21 MLLMs, including both proprietary and open-source variants. Proprietary models were accessed via API, and open-source models were run locally on a single Nvidia A100-80GB GPU. Under the zero-shot protocol, each model received only the chart and its corresponding question, without any in-context examples or prior training. Four astronomy researchers were also invited to establish a human baseline by answering 10% of questions from each category using the same prompts as the models to ensure fairness.

Fine-Tuning Setup To evaluate training effectiveness, we constructed a fine-tuning dataset using the same pipeline as AstroChart, omitting the final expert QA validation step. This yielded 9,857 training and 8,729 validation scientific charts, from which we generated 86,681 and 21,738 QA pairs, respectively. We fine-tuned an open-source model, MiniCPM-V2.6-8B, using the parameter-efficient LoRA (Hu et al. 2021) method. Training was conducted on 8

Nvidia A100-80GB GPUs with BF16 mixed precision and DeepSpeed ZeRO-2 (Rajbhandari et al. 2021) optimization for scalability and efficiency.

Evaluation Metrics We assess the accuracy of model outputs for both numerical and open-ended questions (details in Appendix K). For numerical responses, we computed relative error normalized by the axis range for retrieval tasks, and required an exact match for derivation tasks such as counting or arithmetic. For open-ended responses, an LLM judge (DeepSeek-V3) assigned scores from 0 to 1 based on relevance, correctness, and completeness, following Liu et al. (2023c). To verify scoring reliability, we compared DeepSeek-V3’s scores with human annotations on 176 samples, yielding a Pearson correlation of 0.816, Spearman correlation of 0.817, and MAE of 0.096. ROUGE-L (Lin 2004), BLEU-4 (Papineni et al. 2002), and L3Score (Pramanick, Chellappa, and Venugopalan 2024) show similar trends to LLM scoring (see Appendix L).

Benchmarking 21 MLLMs on AstroChart

We report the performance of 21 MLLMs on AstroChart across FQA and AQA categories, as shown in table 2.

In FQA, models performed strongly on visual understanding tasks—top performers such as Gemini-2.5-Pro and GPT-4o achieved over 85% accuracy across categories like color, style, and layout, indicating mature capabilities in recognizing and interpreting visual elements. In contrast, data-centric tasks, especially those involving interval comparison and numerical calculation, remained more challenging. Although leading models exceeded 60% on interval questions, calculation accuracy typically stayed below 50%, exposing a gap in quantitative reasoning.

For AQA, which focuses on knowledge-based inference, performance declined further. Even top models scored below 75%, showing the challenge of integrating chart evidence with astronomy knowledge. In the human baseline, researchers achieved only 39%, far lower than leading VLMs, suggesting that even experts face limits beyond their sub-fields. These results confirm AstroChart as a valuable benchmark for assessing MLLMs’ scientific reasoning ability.

Fine-Tuning a Representative MLLM

To further assess AstroChart’s value as a training resource, we fine-tuned MiniCPM-V2.6-8B, the strongest performer among mid-sized open-source models, using a training set generated by the same pipeline as AstroChart (excluding expert validation). As shown in Table 2, the fine-tuned model achieves consistent improvements across all FQA and AQA categories, with an overall gain of 5.02%, confirming the effectiveness of our training data in enhancing both visual understanding and scientific reasoning.

To evaluate generalization, we tested the fine-tuned MiniCPM on three existing CQA benchmarks: CharXiv, ChartQA, and MMC-Benchmark. As shown in Table 3, performance changes are minimal, i.e., some metrics slightly increase while others slightly drop. This suggests that the model has not overfitted AstroChart and that its learned reasoning skills remain largely transferable across domains.

Model	FQA										AQA			
	Visual/602					Data/316					Infer./289	Chart Desc./302	KB-Infer./181	All/1690
	All	Color	Style	Text	Layout	All	Point	Interval	Calculation					
Human Baseline(10% Sample)	98.60	98.54	98.40	98.63	99.53	96.40	98.62	93.86	96.50	91.82	70.00	39.00	85.56	
Proprietary Multimodal Large Language Models														
Gemini-2.5-Pro(Google 2025)	88.22	87.37	87.70	90.23	84.67	72.66	81.22	75.10	56.43	81.31	81.09	73.65	81.30	
Gemini-2.5-flash(Google 2025)	87.21	87.04	87.04	88.73	81.78	64.15	68.34	63.40	58.57	82.01	82.65	72.49	79.62	
GPT-4o(OpenAI 2024)	86.23	88.92	84.15	85.31	84.67	53.19	53.78	60.35	43.57	75.40	80.96	73.04	75.84	
Qwen-VL-Max(Qwen Team 2023)	83.13	87.79	76.78	83.43	77.78	50.96	52.27	56.55	42.14	75.16	76.62	68.23	72.99	
Open-source Multimodal Large Language Models														
TinyChart-3B(Zhang et al. 2024)	29.41	47.75	25.15	13.71	27.11	12.22	18.80	9.39	5.48	23.94	1.56	20.83	19.36	
Llava1.5-7B(Liu et al. 2024c)	31.04	49.39	27.70	14.34	33.33	8.47	8.88	7.98	8.45	42.53	13.94	45.36	27.26	
Llava1.6-Mistral-7B(Liu et al. 2024d)	46.45	61.36	41.96	33.00	50.89	13.77	17.74	14.18	7.14	49.24	23.84	48.23	36.97	
Qwen-VL-Chat-7B(Qwen Team 2023)	44.47	55.73	41.04	32.68	54.44	10.47	16.11	6.72	6.31	38.89	22.05	45.19	33.23	
Janus-Pro-7B(DeepSeek 2024)	66.69	74.74	67.26	56.62	74.67	32.27	35.10	38.09	20.83	56.37	51.23	54.75	54.45	
MiniCPM-V2.6-8B(OpenBMB 2024)	70.31	75.92	61.89	71.92	61.78	33.30	34.87	43.74	18.21	55.16	55.60	54.20	56.44	
InternVL3-8B(OpenGVLab 2025)	66.64	72.72	62.04	62.23	71.78	35.41	38.89	42.87	20.95	54.33	49.57	54.09	54.30	
mPLUG-Owl2-8.2B(Ye et al. 2023b)	28.54	39.95	27.70	16.48	32.00	9.48	11.15	12.20	3.57	38.41	9.37	42.21	24.70	
Pixtral-12B(Mistral AI 2024a)	79.27	83.00	75.70	78.26	76.89	51.54	53.63	60.64	37.26	71.90	78.74	69.28	71.66	
Llava1.6-Vicuna-13B(Liu et al. 2024d)	49.45	66.43	44.74	34.84	50.89	13.23	17.77	10.40	9.64	44.36	23.44	50.77	37.30	
SPHINX-v2-13B(Liu et al. 2024a)	31.68	48.40	29.41	18.26	21.11	7.23	13.36	1.47	4.76	37.27	6.13	44.25	24.84	
Llama4-Maverick-17B(Meta 2025)	84.27	86.01	78.59	86.20	83.56	56.30	55.14	58.27	55.71	77.02	76.42	74.64	75.37	
CogVLM2-19B(Zhipu AI 2024)	66.29	74.81	54.52	64.04	71.78	29.27	29.82	37.48	18.45	51.90	54.90	50.66	53.20	
Gemma-3-27B(Gemma 2025)	69.93	69.30	68.44	69.06	80.89	37.21	38.22	47.63	22.98	58.72	66.23	62.54	60.44	
Llava1.6-Yi-34B(Liu et al. 2024d)	50.63	66.34	44.37	37.93	53.56	18.19	17.60	25.30	10.48	47.09	36.19	55.36	41.89	
Qwen2.5-VL-72B(Qwen Team 2025)	83.21	85.31	77.04	86.34	76.22	53.46	54.57	56.36	48.21	72.46	77.52	68.34	73.20	
Pixtral-large-124B(Mistral AI 2024b)	86.11	86.76	82.59	88.22	82.44	59.38	63.67	63.51	47.74	78.65	80.93	70.83	77.23	
Fine-tuned														
MiniCPM-V2.6-8B-fine-tuned	78.15↑	81.08↑	76.26↑	76.76↑	76.00↑	37.47↑	37.66↑	47.78↑	24.64↑	56.30↑	60.89↑	57.02↑	61.46↑	

Table 2: Accuracy (%) on the AstroChart benchmark. ‘‘Infer.’’ denotes Inference, and ‘‘Chart Desc.’’ denotes Chart Description, and ‘‘KB-Infer.’’ denotes KB-Inference. Bold numbers indicate the best-performing model among proprietary and open-source MLLMs, respectively (see Appendix M for model architecture details).

CharXiv			
	Descriptive	Reasoning	Overall
MiniCPM-V2.6-8B	54.06	29.15	49.08
MiniCPM-V2.6-8B-fine-tuned	54.58	29.30	49.52↑
ChartQA			
	Human	Augmented	Overall
MiniCPM-V2.6-8B	57.12	83.84	70.48
MiniCPM-V2.6-8B-fine-tuned	58.24	80.80	69.52↓
MMC-Benchmark			
	MCQ	T/F	Overall
MiniCPM-V2.6-8B	66.46	77.56	74.40
MiniCPM-V2.6-8B-fine-tuned	62.38	77.42	73.28↓

Table 3: Performance of MiniCPM-V2.6-8B before and after fine-tuning on various CQA benchmarks.

Difficulty Comparison with CharXiv

Figure 4 compares model performance on AstroChart and CharXiv. We choose CharXiv for this comparison because, among existing benchmarks, it contains charts with the second-highest overall visual complexity after AstroChart (see Figure 3). To ensure fairness, we randomly sample 1,600 QA pairs from CharXiv to match AstroChart in size. Despite this, we observe a consistent performance drop across multiple MLLMs on AstroChart, highlighting its greater difficulty. All evaluations follow a unified metric framework for consistency.

This gap stems not only from complex visual structures but also from domain-specific questions that require deeper scientific reasoning rather than shallow visual interpretation.

Evaluation of AQA Generation on Domains

To evaluate the generalizability of DomainCQA across disciplines, we conduct a pilot study in four additional scientific

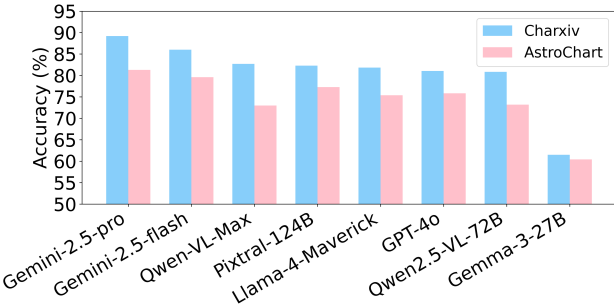


Figure 4: Performance comparison of MLLMs on Charxiv and AstroChart.

Domain	Relevance (R/A)	Validity (R/A)
Astronomy	3.27 / 3.84	0.73 / 0.76
Biochemistry	3.48 / 3.80	0.86 / 0.98
Economics	3.48 / 3.78	0.95 / 0.98
Medicine	3.21 / 3.77	0.89 / 0.96
Social Science	3.23 / 3.46	0.95 / 0.93

Table 4: Expert validation scores for QA pairs generated from randomly sampled charts from the FQA pool (R) vs. AQA-selected charts (A).

domains: biochemistry, economics, medicine, and social science. While the full benchmark includes both FQA and AQA components, we focus on AQA, which selects chart abstracts and generates knowledge-intensive questions. In contrast, FQA involves domain-aware sampling and requires minimal downstream evaluation. This study examines whether AQA can reliably identify knowledge-centric charts and generate high-quality, domain-relevant QA pairs across diverse fields.

Domain experts independently assess each QA pair along two dimensions. Domain relevance is scored on a 1–5 scale, with higher scores indicating deeper and more precise use of domain-specific knowledge beyond what is directly shown in the chart. QA validity is scored as 1 (correct), 0 (cannot determine), or -1 (incorrect), based on clarity of the question and factual correctness of the answer.

As shown in Table 4, AQA-generated QA pairs generally receive higher scores in both relevance and validity compared to those from randomly sampled FQA charts across all domains (see Appendix O for rating criteria). This expert validation confirms the robustness and adaptability of the DomainCQA methodology, supporting its application to a broad range of scientific fields.

Discussion

Limitations Revealed by AstroChart AstroChart highlights key weaknesses in current MLLMs when handling scientific charts. Most models do well on visual tasks like identifying layouts or chart types, but struggle with detailed perception, especially in distinguishing similar colors or reading small labels. Their numerical reasoning is also weak, that is, models often misread axis values or return full axis ranges

instead of specific intervals. On calculation tasks, such issues are made worse by OCR errors and limited math skills.

AQA evaluation reveals deeper challenges in domain understanding. Many models give vague, generic responses, confuse scientific ideas, or misuse technical terms. This shows a clear gap in vision-language alignment and the lack of embedded scientific knowledge. A major reason is that most vision-language pretraining relies on generic image-caption pairs, which fail to expose models to the structured layouts and domain-specific terminology found in scientific charts (see Appendix N for failure cases).

Effectiveness of DomainCQA Our results demonstrate the effectiveness of DomainCQA as both a benchmark construction framework and a practical training pipeline. By reusing the same generation methodology to build a fine-tuning set without targeting specific weaknesses, we cover challenging tasks like data interpretation, visual discrimination, and domain-informed inference. Fine-tuning on this dataset consistently improves performance on both FQA and AQA tasks, showing the QA pairs’ informativeness and training value. The fine-tuned model also performs well on external benchmarks such as CharXiv, ChartQA, and MMC-Benchmark, indicating it has not overfit to AstroChart and that its reasoning skills transfer across domains. Moreover, DomainCQA can be easily applied to other scientific fields, highlighting its generalizability as a domain-independent CQA construction pipeline.

Conclusion & Future Work

Conclusion We present **DomainCQA**, a structured methodology for building domain-specific chart QA benchmarks, and demonstrate its effectiveness through *AstroChart*, the first CQA benchmark for astronomy. AstroChart captures both basic chart understanding and domain-informed reasoning. Through extensive evaluation of 21 MLLMs, we reveal consistent weaknesses in chart understanding, especially when models integrate visual features with domain-specific knowledge. In addition to AstroChart, we apply DomainCQA to four scientific fields, such as biochemistry, economics, medicine, and social science, conducting pilot AQA studies with expert validation. These results confirm the generality and effectiveness of our methodology in producing high-quality, relevant, and challenging QA pairs. Furthermore, using data generated by DomainCQA for fine-tuning significantly improves MLLM performance across diverse chart reasoning tasks without overfitting, highlighting the training utility of our pipeline.

Future Work Building on our preliminary exploration across multiple scientific domains, we plan to extend DomainCQA into a broader suite of benchmarks in multiple scientific domains. Our long-term goal is to establish DomainCQA as a standard framework for chart-based scientific reasoning in real-world MLLM applications.

Ethical Statement

This work does not involve human or animal subjects. All data used in this work are chart-based and originate from

publicly available scientific publications. These materials were accessed solely for research purposes, and no proprietary, confidential, or human-related information is involved. No ethical concerns were identified in the construction of the benchmarks and experiments.

Acknowledgments

We sincerely thank the anonymous reviewers and contributing researchers for their valuable feedback. This research was supported by the National Natural Science Foundation of China (U22A2032), the Leading Innovation and Entrepreneurship Team of Zhejiang Province of China (Grant No. 2023R01008), Zhejiang Provincial Science and Technology Plan Project (2023C01120), Key R&D Program of Zhejiang (2024SSYS0012), and the China Manned Space Project (CMS-CSST-2025-A21).

References

- Anthropic. 2024. Claude 3 Model Family: Opus, Sonnet, Haiku. https://www-cdn.anthropic.com/de8ba9b01c9ab7cbabf5c33b80b7bbc618857627/Model_Card_Claude_3.pdf.
- Casella, G.; and George, E. I. 1992. Explaining the Gibbs Sampler. *The American Statistician*, 46: 167–174.
- Chaudhry, R.; Shekhar, S.; Gupta, U.; Maneriker, P.; Bansal, P.; and Joshi, A. 2020. LEAF-QA: Locate, Encode & Attend for Figure Question Answering. In *2020 IEEE Winter Conference on Applications of Computer Vision (WACV)*, 3501–3510.
- Cohen, J. 1960. A coefficient of agreement for nominal scales. *Educational and psychological measurement*, 20(1): 37–46.
- DeepSeek. 2024. DeepSeek-VL: Towards Real-World Vision-Language Understanding. arXiv:2403.05525.
- Dong, X.; Zhang, P.; Zang, Y.; Cao, Y.; Wang, B.; Ouyang, L.; Wei, X.; Zhang, S.; Duan, H.; Cao, M.; Zhang, W.; Li, Y.; Yan, H.; Gao, Y.; Zhang, X.; Li, W.; Li, J.; Chen, K.; He, C.; Zhang, X.; Qiao, Y.; Lin, D.; and Wang, J. 2024. InternLM-XComposer2: Mastering Free-form Text-Image Composition and Comprehension in Vision-Language Large Model. arXiv:2401.16420.
- Gemma, G. T. 2025. Gemma 3 technical report. arXiv:2503.19786.
- Google, G. T. 2025. Gemini 2.5: Pushing the Frontier with Advanced Reasoning, Multimodality, Long Context, and Next Generation Agentic Capabilities. arXiv:2507.06261.
- Hsu, T.-Y.; Giles, C. L.; and Huang, T.-H. 2021. SciCap: Generating Captions for Scientific Figures. In *Findings of the Association for Computational Linguistics: EMNLP 2021*, 3258–3264. Association for Computational Linguistics.
- Hu, E. J.; Shen, Y.; Wallis, P.; Allen-Zhu, Z.; Li, Y.; Wang, S.; Wang, L.; and Chen, W. 2021. LoRA: Low-Rank Adaptation of Large Language Models. arXiv:2106.09685.
- Huang, K.-H.; Chan, H. P.; Fung, M.; Qiu, H.; Zhou, M.; Joty, S.; Chang, S.-F.; and Ji, H. 2025. From Pixels to Insights: A Survey on Automatic Chart Understanding in the Era of Large Foundation Models. *IEEE Transactions on Knowledge and Data Engineering*, 37(5): 2550–2568.
- Kafle, K.; Price, B.; Cohen, S.; and Kanan, C. 2018. Dvqa: Understanding data visualizations via question answering. In *Proceedings of the IEEE conference on computer vision and pattern recognition*, 5648–5656.
- Kahou, S. E.; Michalski, V.; Atkinson, A.; Kadar, A.; Trischler, A.; and Bengio, Y. 2018. FigureQA: An Annotated Figure Dataset for Visual Reasoning. arXiv:1710.07300.
- Kantharaj, S.; Do, X. L.; Leong, R. T.; Tan, J. Q.; Hoque, E.; and Joty, S. 2022. OpenCQA: Open-ended Question Answering with Charts. In Goldberg, Y.; Kozareva, Z.; and Zhang, Y., eds., *Proceedings of the 2022 Conference on Empirical Methods in Natural Language Processing*, 11817–11837. Abu Dhabi, United Arab Emirates: Association for Computational Linguistics.
- Li, S.; and Tajbakhsh, N. 2023. SciGraphQA: A Large-Scale Synthetic Multi-Turn Question-Answering Dataset for Scientific Graphs. arXiv:2308.03349.
- Lin, C.-Y. 2004. ROUGE: A Package for Automatic Evaluation of Summaries. In *Text Summarization Branches Out*, 74–81. Barcelona, Spain: Association for Computational Linguistics.
- Liu, D.; Zhang, R.; Qiu, L.; Huang, S.; Lin, W.; Zhao, S.; Geng, S.; Lin, Z.; Jin, P.; Zhang, K.; Shao, W.; Xu, C.; He, C.; He, J.; Shao, H.; Lu, P.; Qiao, Y.; Li, H.; and Gao, P. 2024a. SPHINX-X: Scaling Data and Parameters for a Family of Multi-modal Large Language Models. In Salakhutdinov, R.; Kolter, Z.; Heller, K.; Weller, A.; Oliver, N.; Scarlett, J.; and Berkenkamp, F., eds., *Proceedings of the 41st International Conference on Machine Learning*, volume 235 of *Proceedings of Machine Learning Research*, 32400–32420. PMLR.
- Liu, F.; Piccinno, F.; Krichene, S.; Pang, C.; Lee, K.; Joshi, M.; Altun, Y.; Collier, N.; and Eisenschlos, J. 2023a. MatCha: Enhancing Visual Language Pretraining with Math Reasoning and Chart Derendering. In Rogers, A.; Boyd-Graber, J.; and Okazaki, N., eds., *Proceedings of the 61st Annual Meeting of the Association for Computational Linguistics (Volume 1: Long Papers)*, 12756–12770. Toronto, Canada: Association for Computational Linguistics.
- Liu, F.; Wang, X.; Yao, W.; Chen, J.; Song, K.; Cho, S.; Yacoob, Y.; and Yu, D. 2024b. MMC: Advancing Multimodal Chart Understanding with Large-scale Instruction Tuning. In Duh, K.; Gomez, H.; and Bethard, S., eds., *Proceedings of the 2024 Conference of the North American Chapter of the Association for Computational Linguistics: Human Language Technologies (Volume 1: Long Papers)*, 1287–1310. Mexico City, Mexico: Association for Computational Linguistics.
- Liu, H.; Li, C.; Li, Y.; and Lee, Y. J. 2024c. Improved Baselines with Visual Instruction Tuning. In *2024 IEEE/CVF Conference on Computer Vision and Pattern Recognition (CVPR)*, 26286–26296.
- Liu, H.; Li, C.; Li, Y.; Li, B.; Zhang, Y.; Shen, S.; and Lee, Y. J. 2024d. LLaVA-NeXT: Improved reasoning, OCR, and

- world knowledge. <https://llava-vl.github.io/blog/2024-01-30-llava-next/>.
- Liu, H.; Li, C.; Wu, Q.; and Lee, Y. J. 2023b. Visual instruction tuning. *Advances in neural information processing systems*, 36: 34892–34916.
- Liu, Y.; Iter, D.; Xu, Y.; Wang, S.; Xu, R.; and Zhu, C. 2023c. G-Eval: NLG Evaluation using Gpt-4 with Better Human Alignment. In Bouamor, H.; Pino, J.; and Bali, K., eds., *Proceedings of the 2023 Conference on Empirical Methods in Natural Language Processing*, 2511–2522.
- Masry, A.; Do, X. L.; Tan, J. Q.; Joty, S.; and Hoque, E. 2022. ChartQA: A Benchmark for Question Answering about Charts with Visual and Logical Reasoning. In Mure-
san, S.; Nakov, P.; and Villavicencio, A., eds., *Findings of the Association for Computational Linguistics: ACL 2022*, 2263–2279. Dublin, Ireland: Association for Computational Linguistics.
- Masry, A.; Kavehzadeh, P.; Do, X. L.; Hoque, E.; and Joty, S. 2023. UniChart: A Universal Vision-language Pre-trained Model for Chart Comprehension and Reasoning. In Bouamor, H.; Pino, J.; and Bali, K., eds., *Proceedings of the 2023 Conference on Empirical Methods in Natural Language Processing*, 14662–14684. Singapore: Association for Computational Linguistics.
- Meng, F.; Shao, W.; Lu, Q.; Gao, P.; Zhang, K.; Qiao, Y.; and Luo, P. 2024. ChartAssistant: A Universal Chart Multimodal Language Model via Chart-to-Table Pre-training and Multitask Instruction Tuning. In *Findings of the Association for Computational Linguistics: ACL 2024*, 7775–7803. Bangkok, Thailand: Association for Computational Linguistics.
- Meta. 2025. Llama 4: A New Era of Natively Multimodal AI Innovation. <https://ai.meta.com/blog/llama-4-multimodal-intelligence/>. Accessed: 2025-06-26.
- Methani, N.; Ganguly, P.; Khapra, M. M.; and Kumar, P. 2020. PlotQA: Reasoning over Scientific Plots. In *The IEEE Winter Conference on Applications of Computer Vision (WACV)*.
- Mistral AI. 2024a. Pixtral 12B. arXiv:2410.07073.
- Mistral AI. 2024b. Pixtral Large: A 124B Open-Weights Multimodal Model. Mistral AI blog and model page.
- OpenAI. 2024. GPT-4 Technical Report. arXiv:2303.08774.
- OpenBMB. 2024. MiniCPM-V: A GPT-4V Level MLLM on Your Phone. arXiv:2408.01800.
- OpenGVLab. 2025. InternVL3: Exploring Advanced Training and Test-Time Recipes for Open-Source Multimodal Models. arXiv:2504.10479.
- Papineni, K.; Roukos, S.; Ward, T.; and Zhu, W.-J. 2002. Bleu: a Method for Automatic Evaluation of Machine Translation. In Isabelle, P.; Charniak, E.; and Lin, D., eds., *Proceedings of the 40th Annual Meeting of the Association for Computational Linguistics*, 311–318. Philadelphia, Pennsylvania, USA: Association for Computational Linguistics.
- Pramanick, S.; Chellappa, R.; and Venugopalan, S. 2024. Spiqa: A dataset for multimodal question answering on scientific papers. *Advances in Neural Information Processing Systems*, 37: 118807–118833.
- Qwen Team, A. G. 2023. Qwen-VL: A Versatile Vision-Language Model for Understanding, Localization, Text Reading, and Beyond. arXiv:2308.12966.
- Qwen Team, A. G. 2025. Qwen2.5-VL Technical Report. arXiv:2502.13923.
- Rajbhandari, S.; Ruwase, O.; Rasley, J.; Smith, S.; and He, Y. 2021. Zero-infinity: Breaking the gpu memory wall for extreme scale deep learning. In *Proceedings of the international conference for high performance computing, networking, storage and analysis*, 1–14.
- Singh, H.; and Shekhar, S. 2020. STL-CQA: Structure-based Transformers with Localization and Encoding for Chart Question Answering. In *Proceedings of the 2020 Conference on Empirical Methods in Natural Language Processing (EMNLP)*, 3275–3284.
- Team, R.; Ormazabal, A.; Zheng, C.; de Masson d'Autume, C.; Yogatama, D.; Fu, D.; Ong, D.; Chen, E.; Lamprecht, E.; Pham, H.; Ong, I.; Aleksiev, K.; Li, L.; Henderson, M.; Bain, M.; Artetxe, M.; Relan, N.; Padlewski, P.; Liu, Q.; Chen, R.; Phua, S.; Yang, Y.; Tay, Y.; Wang, Y.; Zhu, Z.; and Xie, Z. 2024. Reka Core, Flash, and Edge: A Series of Powerful Multimodal Language Models. arXiv:2404.12387.
- Wang, Z.; Xia, M.; He, L.; Chen, H.; Liu, Y.; Zhu, R.; Liang, K.; Wu, X.; Liu, H.; Malladi, S.; Chevalier, A.; Arora, S.; and Chen, D. 2024. CharXiv: Charting Gaps in Realistic Chart Understanding in Multimodal LLMs. arXiv:2406.18521.
- Xia, R.; Zhang, B.; Ye, H.; Yan, X.; Liu, Q.; Zhou, H.; Chen, Z.; Ye, P.; Dou, M.; Shi, B.; Yan, J.; and Qiao, Y. 2025. ChartX & ChartVLM: A Versatile Benchmark and Foundation Model for Complicated Chart Reasoning. arXiv:2402.12185.
- Ye, J.; Xu, H.; Liu, H.; Hu, A.; Yan, M.; Qian, Q.; Zhang, J.; Huang, F.; and Zhou, J. 2024. mPLUG-Owl3: Towards Long Image-Sequence Understanding in Multi-Modal Large Language Models. arXiv:2408.04840.
- Ye, Q.; Xu, H.; Xu, G.; Ye, J.; Yan, M.; Zhou, Y.; Wang, J.; Hu, A.; Shi, P.; Shi, Y.; Jiang, C.; Li, C.; Xu, Y.; Chen, H.; Tian, J.; Qian, Q.; Zhang, J.; and Huang, F. 2023a. mPLUG-Owl: Modularization Empowers Large Language Models with Multimodality. arXiv:2304.14178.
- Ye, Q.; Xu, H.; Ye, J.; Yan, M.; Hu, A.; Liu, H.; Qian, Q.; Zhang, J.; Huang, F.; and Zhou, J. 2023b. mPLUG-Owl2: Revolutionizing Multi-modal Large Language Model with Modality Collaboration. arXiv:2311.04257.
- Zhang, L.; Hu, A.; Xu, H.; Yan, M.; Xu, Y.; Jin, Q.; Zhang, J.; and Huang, F. 2024. TinyChart: Efficient Chart Understanding with Visual Token Merging and Program-of-Thoughts Learning. arXiv:2404.16635.
- Zhipu AI. 2024. CogVLM2: Visual Language Models for Image and Video Understanding. arXiv:2408.16500.

Appendix

A. Details of Chart Complexity Vector (CCV)

A.1. The Definition of CCV

To quantify the complexity of scientific charts, we introduce the Chart Complexity Vector (CCV), table 5 defines the Chart Complexity Vector (CCV), which quantifies chart complexity across ten attributes categorized into visual complexity (annotation, color, legend, pattern), data interpretation complexity (axis, element, formula, scale), and structural complexity (subplot, type). Each attribute is assigned a binary score of 0 (simple) or 1 (complex) based on specific criteria.

#	Attributes	Complexity Definition (0 or 1)
Visual Complexity		
1	Annotation Complexity	0: No annotations are used. 1: Extensive annotations such as descriptive text, arrows, or markers.
2	Color Complexity	0: Monochrome or up to two distinct colors. 1: More than two distinct colors or employs a color bar.
3	Legend Complexity	0: Contains no legend or a minimal legend (no more than three categories). 1: Contains a complex legend (more than three categories or intricate representations).
4	Pattern Complexity	0: No more than two distinct graphical patterns. 1: More than two distinct graphical patterns.
Data Interpretation Complexity		
5	Axis Complexity	0: Single axis. 1: Multiple dependent axes (e.g., secondary y-axis, dual x-axis).
6	Element Complexity	0: Contains a single graphical element. 1: Contains more than two graphical elements.
7	Scale Complexity	0: Employs a linear scale. 1: Utilizes logarithmic, power-law, or mixed scales.
8	Formula Complexity	0: Does not contain any mathematical formulas. 1: Includes mathematical formulas.
Structural Complexity		
9	Subplot Complexity	0: A single-panel chart. 1: Multiple interrelated subplots are present.
10	Type Complexity	0: Uses basic chart types (e.g., bar, line, scatter, histogram, pie) with a sparse dataset. 1: Uses complex chart types (e.g., heatmaps, network graphs, mixed-element charts, multiple chart combinations) and/or handles high-density data (e.g., dense bar, line, scatter, or histogram charts).

Table 5: Definitions of CCV Attributes

A.2. Proportion of Complexity Aspects in AstroChart

We proposed a multi-label chart classification model aimed at predicting the 10 complexity dimensions defined by the CCV framework. The model is built upon a ResNet-50 backbone, followed by 10 parallel binary classification heads corresponding to each complexity dimension. To address significant class imbalance, we employed Focal Loss, weighted random sampling, and a range of data augmentation strategies. Training was conducted on a human-annotated, multi-domain dataset covering 6 domains, consisting of 2,474 training samples, 246 validation samples and 248 testing samples. The model achieved a Macro F1 score of 61.50%, Macro Precision of 58.15%, and Macro Recall of 65.95% on the testing set.

Building upon this classifier, we further analyze the CCV complexity distribution of charts in the AstroChart benchmark. As summarized in table 6, the distribution of simple versus complex charts across the ten CCV dimensions reveals distinct structural characteristics of astronomical visualizations. The results indicate that Color Complexity (78%) and Type Complexity (68%) are the most frequently observed complex attributes, suggesting a prevalence of multi-colored and structurally diverse charts. In contrast, Axis Complexity (92%) and Element Complexity (65%) are predominantly simple, implying that most charts use a single axis and contain limited graphical elements. These statistics provide insight into the complexity characteristics of charts in AstroChart.

#	Attributes	Simple	Complex
Visual Complexity			
1	Annotation Complexity	59%	41%
2	Color Complexity	22%	78%
3	Legend Complexity	53%	47%
4	Pattern Complexity	49%	51%
Data Interpretation Complexity			
5	Axis Complexity	92%	8%
6	Element Complexity	65%	35%
7	Scale Complexity	58%	42%
8	Formula Complexity	63%	37%
Structural Complexity			
9	Subplot Complexity	58%	42%
10	Type Complexity	32%	68%

Table 6: The proportion of simple/complex charts across different complexity aspects in AstroChart

A.3. Examples of CCV in AstroChart

To illustrate how CCV attributes are applied in practice, we provide concrete examples from the AstroChart dataset, fig. 5 and fig. 6 illustrate the process of computing CCV for each astronomical chart.

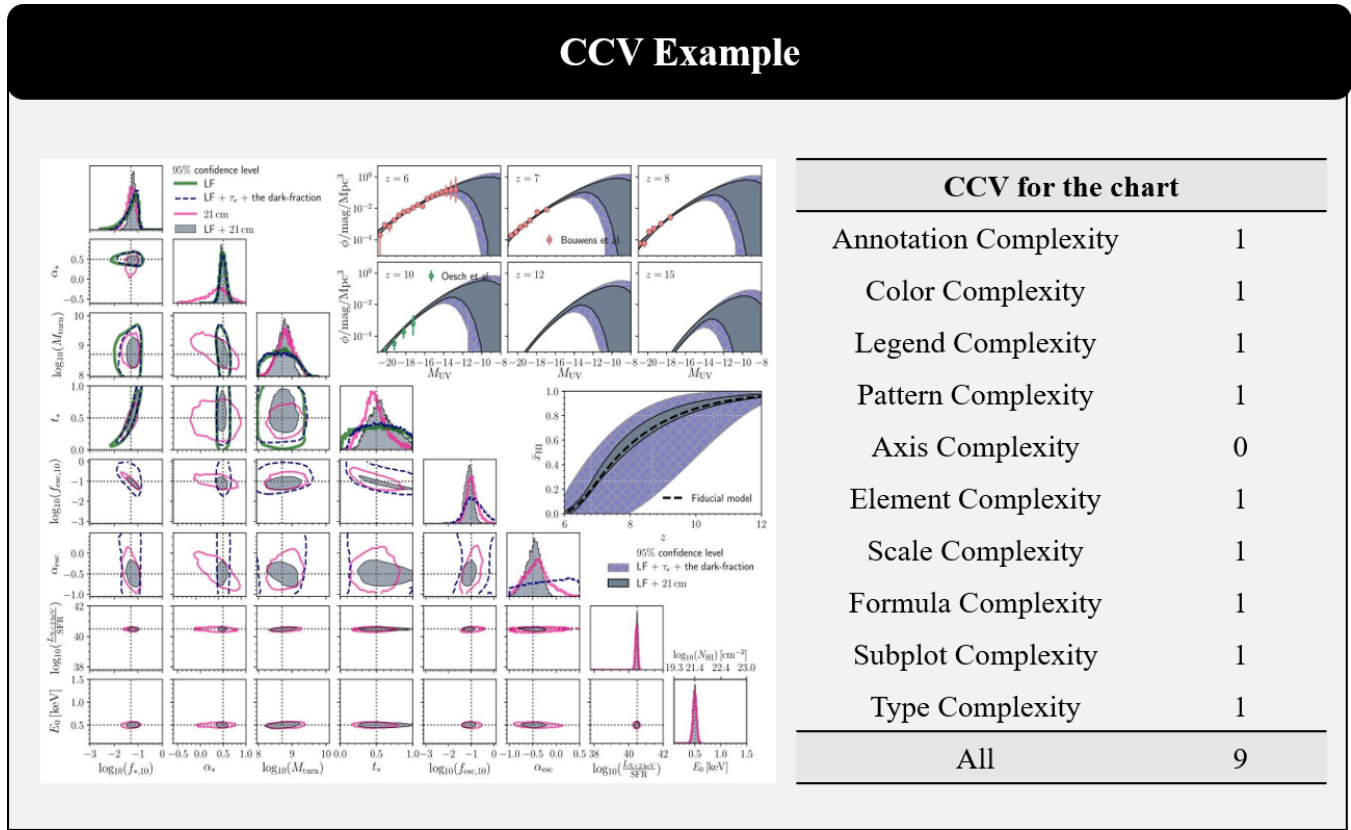
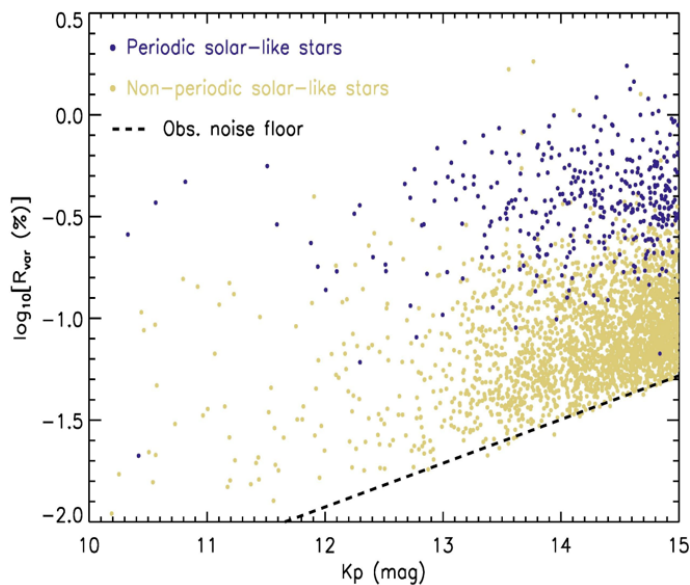


Figure 5: Example for CCV in AstroChart

CCV Example



CCV for the chart	
Annotation Complexity	0
Color Complexity	1
Legend Complexity	1
Pattern Complexity	1
Axis Complexity	0
Element Complexity	1
Scale Complexity	0
Formula Complexity	0
Subplot Complexity	0
Type Complexity	0
All	4

Figure 6: Example for CCV in AstroChart

A.4. Representative Charts by CCV Score Ranges

To better illustrate how the Chart Complexity Vector (CCV) reflects real-world chart variation, we present example charts from the AstroChart dataset corresponding to three distinct CCV score ranges: low (0–3), medium (4–7), and high (8–10). These examples demonstrate increasing levels of visual, structural, and data interpretation complexity.

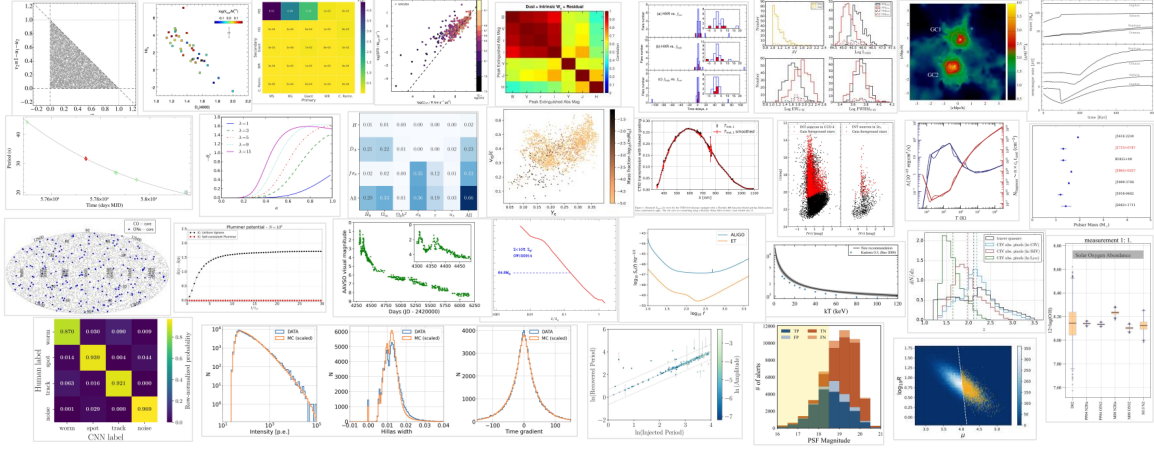


Figure 7: Example chart with low CCV score (0–3): Simple structure with minimal annotations and basic data patterns.

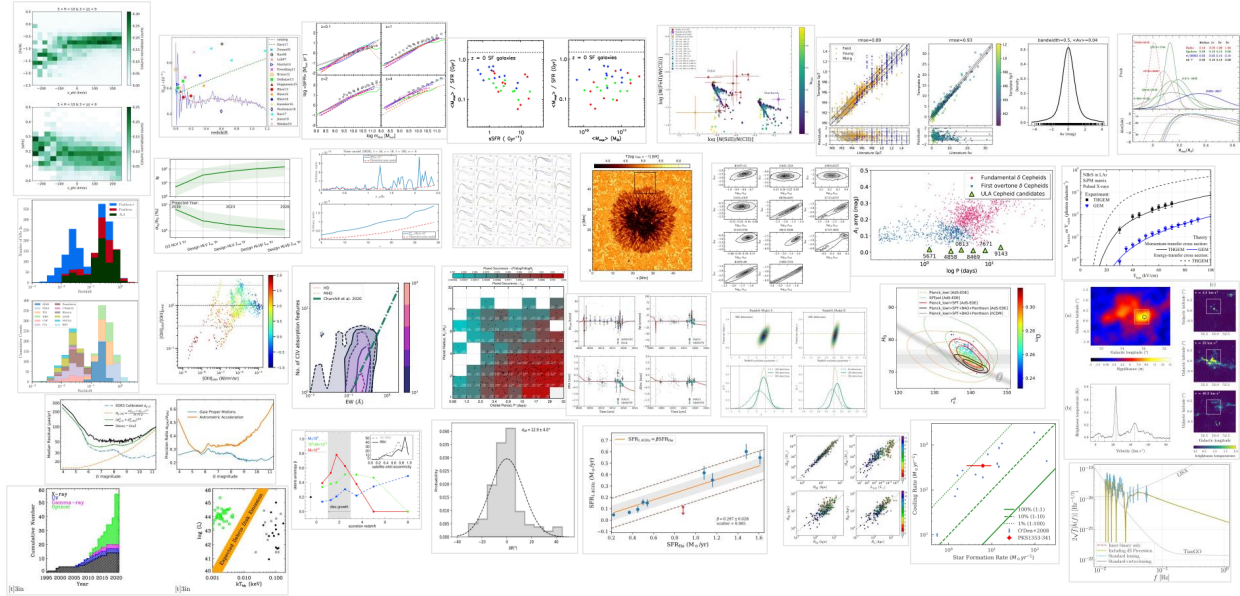


Figure 8: Example chart with medium CCV score (4–7): Moderate use of visual and structural complexity such as subplots or multiple legends.

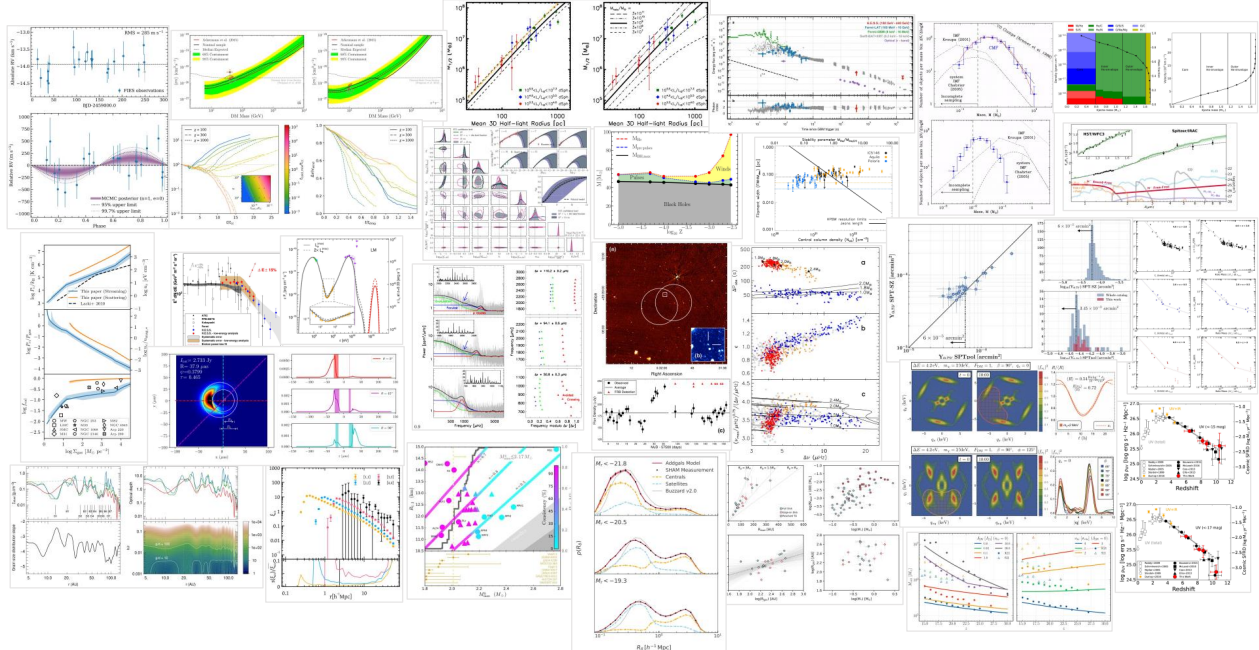


Figure 9: Example chart with high CCV score (8–10): Highly complex layout with rich annotations, multiple axes, and diverse data encodings.

B. Gibbs sampling

We employ a Gibbs sampling strategy to construct a representative set of charts for FQA generation. The detailed procedure is presented below.

Algorithm 1: Gibbs sampling for chart selection in FQA pairs

Require: Chart dataset D with $CCV(c)$ for each $c \in D$

Ensure: Selected benchmark charts S

```
1: Initialize: Randomly select initial  $S \subset D$  of size target_size
2: repeat
3:   for each chart  $c^* \in S$  do
4:     Select aspect  $\alpha$  in  $CCV$ 
5:     Fix other aspects, sample  $v \sim P(\alpha | S, D)$ 
6:     Find  $c_{\text{new}} \in D$  with  $\alpha(c_{\text{new}}) = v$ 
7:     if  $CCV(S \cup \{c_{\text{new}}\} - \{c^*\})$  is valid then
8:       Replace  $c^*$  with  $c_{\text{new}}$  in  $S$ 
9:     end if
10:   end for
11: until distribution stabilizes
12: return  $S$ 
```

C. COT&VOT

To identify the most representative chart for generating Advanced Question-Answer (AQA) pairs, we design a CoT&VoT-based selection framework. CoT (Chain-of-Thought) reasoning enables models to summarize chart content in a structured manner, while VoT (Voting over Thought) aggregates multiple model outputs to ensure robust selection. The algorithm below outlines how we utilize multiple LLMs to assess the alignment between each chart and the paper's core scientific narrative (abstract and conclusion), ultimately selecting the most relevant chart via majority voting.

Algorithm 2: CoT and VoT for chart selection in AQA pairs

[:1]

Require: Paper P with charts $\{C_1, \dots, C_N\}$; models $\{M_1, \dots, M_k\}$

Ensure: Selected chart abstract C^*

```
1: for each  $m_j \in \{M_1, \dots, M_k\}$  do
2:   Extract abstract and conclusion, generate  $P_j$ 
3:   for each chart  $C_i$  do
4:     Extract caption/description
5:     Generate summary  $S_{ij}$  using  $M_j$ 
6:     Compute relevance  $R_{ij}$  with  $P_j$ 
7:   end for
8:   Select chart  $C_j^*$  with highest  $R_{ij}$ 
9: end for
10: Identify  $C^*$  by majority vote of  $C_j^*$  return  $C^*$ 
```

D. Prompts for question-answer pair generation in AstroChart

We employed Claude 3.5 to generate question-answer pairs, designing distinct prompts for each category of questions. Specifically, for the two primary types: FQA pair and AQA pair. We implemented different input configurations. For the FQA pair, the input consisted of the chart along with its corresponding caption. For the AQA pair, the input additionally included descriptive content from the associated paper. This differentiation was essential, as knowledge-based questions often require contextual background derived from the broader content of the paper.

To generate different question-answer pair types, we formulated targeted prompts:

- **FQA pairs:**

- *Visual questions-answer pair* (fig. 10) The questions should focus on the graphical elements of the chart, including colors, labels, text, formulas, and chart types.
- *Data questions-answer pair* (fig. 11) The questions should require retrieving specific data points or a range of values from the chart.
- *Inference questions-answer pair* (fig. 12) The questions should involve numerical calculations, comparisons, or analytical reasoning beyond direct data extraction from the chart.
- *Chart Description questions-answer pair* (fig. 13) The task is to generate a comprehensive summary describing all visual elements of the chart, including colors, labels, texts, formulas, chart types, and structural components.

- **AQA pairs:**

- *KB-Inference questions-answer pair* (fig. 14) The question requires astronomical domain knowledge and analytical reasoning, with a focus on explaining chart relationships using scientific insights, without directly referencing the article's conclusion.

Example For Prompt

Visual Question-Answer Pair

Role:

You are an AI visual assistant who can analyze a scientific paper graph.

Task:

You are provided with an image. Generate three visual questions based solely on the provided image and information.

For each question, provide the following:

Question: The question itself.

Answer: The final, concise answer.

Requirements:

The questions should focus on the graphical elements of the chart, including colors, text, formulas, and chart types. Avoid questions related to identifying maximum or minimum values. Instead, emphasize the interpretation and analysis of visual components, ensuring the questions assess the model's ability to understand and describe chart elements accurately. Avoid questions related to the data range problem. Answers should be within 10 words.

Figure 10: Prompt for visual question-answer pair generation.

Example For Prompt

Data Question-Answer Pair

Role:

You are an AI visual assistant who can analyze a scientific paper graph.

Task:

You are provided with an image. Generate three data questions based solely on the provided image and information.

For each question, provide the following:

Question: The question itself.

Answer: The final, concise answer.

Requirements:

The question should require retrieving specific data points or a range of data points from the chart. Avoid questions that simply read numbers directly from the image or involve identifying maximum or minimum values. Emphasize numerical data retrieval and interpretation to assess the model's ability to extract meaningful information from the chart. Answers should be within 10 words.

Figure 11: Prompt for data question-answer pair generation.

Example For Prompt

Inference Question-Answer Pair

Role:

You are an AI visual assistant who can analyze a scientific paper graph.

Task:

You are provided with an image, caption, and description. Generate two inference questions based solely on the provided image and information.

For each question, provide the following:

Question: The question itself.

Answer: The final, concise answer.

Requirements:

The question requires numerical calculations, comparisons, or analytical reasoning beyond direct data extraction from the image. Ensure the questions involve identifying patterns, relationships, or trends within the chart. Only include questions that have clear, verifiable answers. Answer should be within 20 words.

Figure 12: Prompt for inference question-answer pair generation.

Example For Prompt

Chart Description Question-Answer Pair

Role:

You are an AI visual assistant who can analyze a scientific paper graph.

Task:

You are provided with an image and its caption. Generate a chart summary based solely on the provided image and information.

For each question, provide the following:

Question: The question itself.

Answer: The final, concise answer.

Requirements:

Generate a Chart description that describes all visual elements of the chart, including colors, labels, text, formulas, chart types, and structural components. The summary should provide a clear and structured overview. Answers should be within 100 words.

Figure 13: Prompt for chart description question-answer pair generation.

Example For Prompt

KB-Inference Question-Answer Pair

Role:

You are an AI visual assistant who can analyze a scientific paper graph.

Task:

You are provided with an image which can reveal the conclusion of the article, and the conclusion of the article that related for the figure.

Generate one kb-inference question and the answer based solely on the provided image and information.

For each question, provide the following:

Question: The question itself.

Answer: The final, concise answer.

Requirements:

The question requires astronomical domain knowledge and analytical reasoning. The questions should be answerable based on the given conclusion of the related article while avoiding direct references to 'the paper's conclusion' or similar phrases. Focus on explaining relationships in the chart using relevant scientific insights. The answer should be within 50 words.

Figure 14: Prompt for KB-inference question-answer pair generation.

E. Prompt for GPT4-o filter

To ensure the quality of generated QA pairs, we employ a GPT-4o based filtering mechanism. This appendix provides the exact prompt used to instruct GPT-4o to identify and remove low-quality QA pairs. The goal is to retain only those questions that are clearly grounded in the given chart and, in the case of AQA pairs, necessitate domain-specific knowledge to answer. This filtering step is crucial for maintaining the relevance and rigor of our benchmark.

Example For Prompt

GPT4-o filter

Role: You are an AI visual assistant specialized in analyzing scientific paper graphs.

Task 1: Determine whether answering the given question requires external astronomical domain knowledge beyond what is shown in the chart. Output 1 if external knowledge is necessary, otherwise output 0. Also provide a brief explanation.

Task 2: Determine whether answering the question requires information from the chart itself (e.g., numerical values, labels, or text in the chart). Output 1 if the chart is needed, otherwise output 0. Also provide a brief explanation.

Question: {question}

Output format:

Task 1: <score>, <reason>; Task 2: <score>, <reason>

Figure 15: This is the prompt for gpt4-o filter.

F. Subdomains of astronomy

To ensure the domain diversity and scientific rigor of AQA pairs, we identify six major subdomains within the field of astronomy: High Energy, Earth & Planetary, Solar & Stellar, Cosmology & Nongalactic, Galaxies, and Instrumentation & Methods. From each subdomain, we select the top 1% most-cited papers annually as the source material for question generation. This figure summarizes the distribution of these high-impact papers across subdomains, reflecting the relative volume of influential literature in each area.

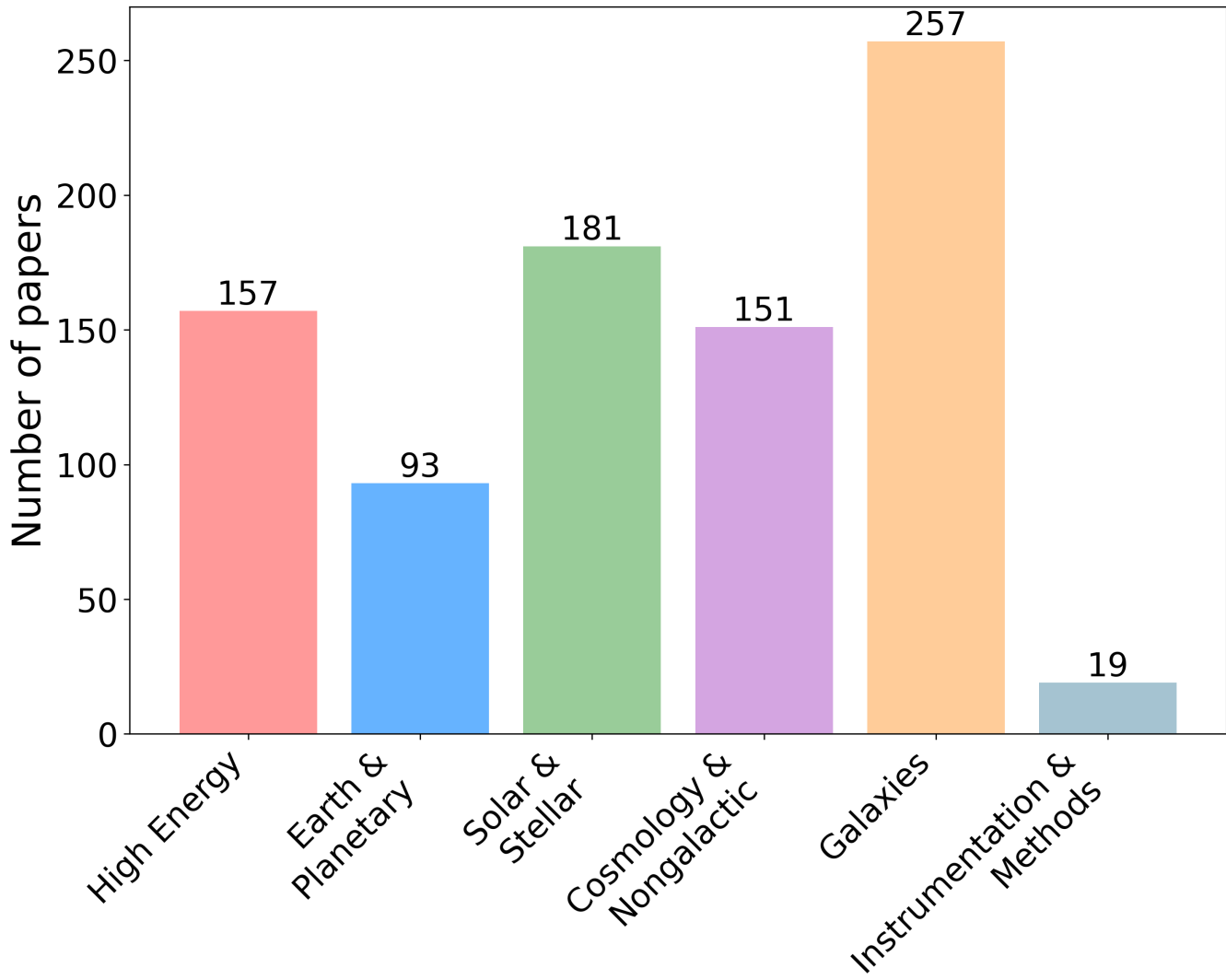


Figure 16: Top 1% most-cited papers selected from six major subdomains of astronomy

G. Visualization of Samples in AstroChart

Fig. 17 visualizes sample charts from the AstroChart benchmark, illustrating its diversity and complexity.

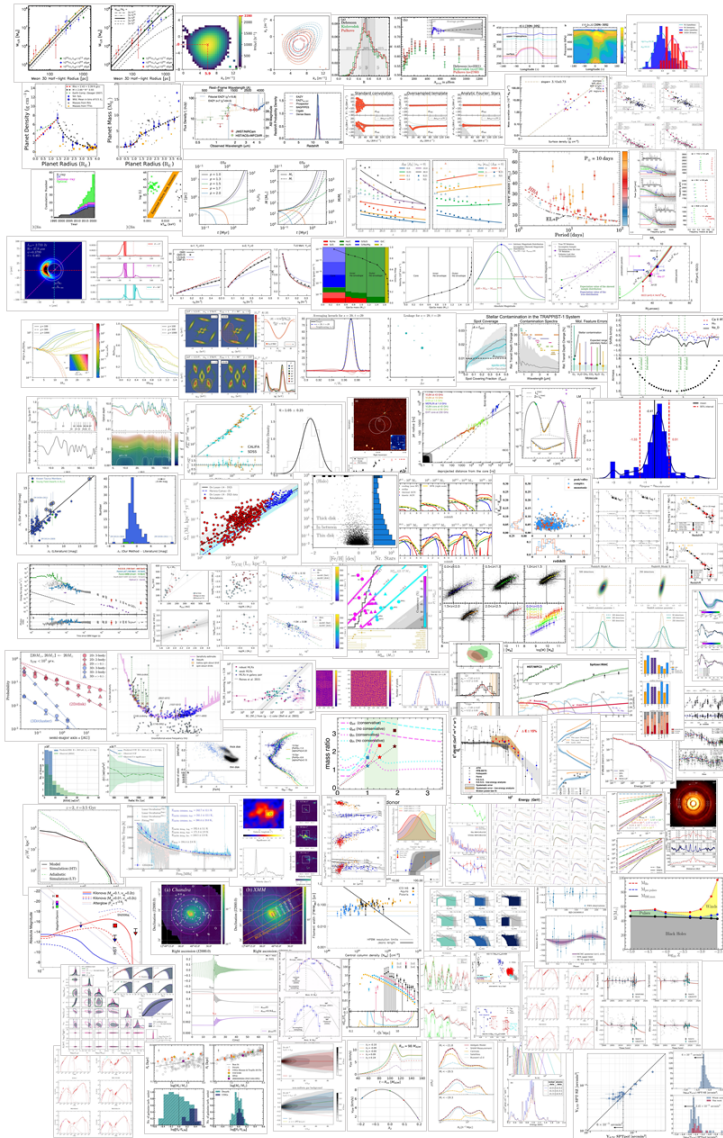


Figure 17: Visualization of Sample Charts in AstroChart

H. Reliability of Automated Filtering with GPT-4o

To evaluate the reliability of the automated filtering step in identifying low-quality QA pairs, we conduct a manual verification experiment on a randomly selected set of 200 KB-Inference QA pairs. Among these, GPT-4o filters out 19 QA pairs. Human annotators then independently re-evaluate the same 200 pairs using the identical filtering criteria.

We find that GPT-4o and human judgments disagree on 7 cases: in 6 instances, GPT-4o marked the pair for deletion while human experts judged them to be valid (false positives); in 1 instance, the human annotators identified a pair for deletion that GPT-4o retained (false negative). The remaining 193 pairs are consistent across both methods.

Based on this comparison, GPT-4o achieves an overall accuracy of 96.5%, a precision of 68.4%, and a recall of 92.9% in identifying deletable QA pairs. Notably, most disagreements are conservative false positives, suggesting that GPT-4o tends to over-filter rather than under-filter. These results indicate that GPT-4o serves as a reasonably reliable filter for large-scale QA dataset curation, with minor manual corrections recommended for high-stakes benchmarks.

GPT-4o also demonstrates substantial agreement with human annotators, with a Cohen’s Kappa coefficient of 0.77, indicating strong consistency in identifying deletable items. These results indicate that GPT-4o serves as a reasonably reliable filter for large-scale QA dataset curation, with minor manual corrections recommended for high-stakes benchmarks.

	Human: Delete	Human: Keep
GPT-4o: Delete	13 (True Positive)	6 (False Positive)
GPT-4o: Keep	1 (False Negative)	180 (True Negative)

Table 7: Confusion matrix for GPT-4o filtering decisions on 200 QA pairs.

I. Examples of AstroChart

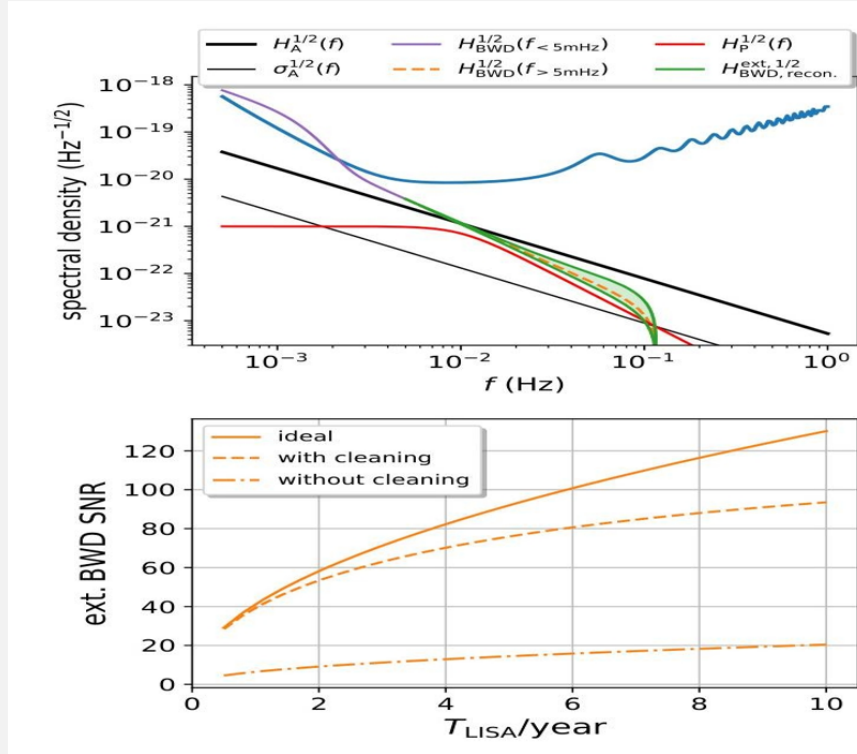
We generated a total of 1890 question-answer pairs, consisting of 1,509 FQA pairs and 381 AQA pairs. The FQA pairs are further divided into four subcategories:

- **Visual question-answer pairs:** 603 in total, covering four Types—Text (fig. 18), Color (fig. 19), Style (fig. 20), and Layout (fig. 21, fig. 22).
- **Data question-answer pairs:** 315 in total, categorized into Calculation (fig. 23, fig. 24), Point (fig. 25), and Interval (fig. 26, fig. 27).
- **Inference questions-answer pair:** 289 pairs (fig. 28, fig. 29, fig. 30, fig. 31, fig. 32).
- **Summary questions-answer pair:** 302 pairs (fig. 33, fig. 34, fig. 35, fig. 36, fig. 37).

The AQA pairs are divided into two types:

- **KB-Inference questions-answer pair:** 200 pairs (fig. 38, fig. 39, fig. 40, fig. 41, fig. 42).

Visual Example



Question:

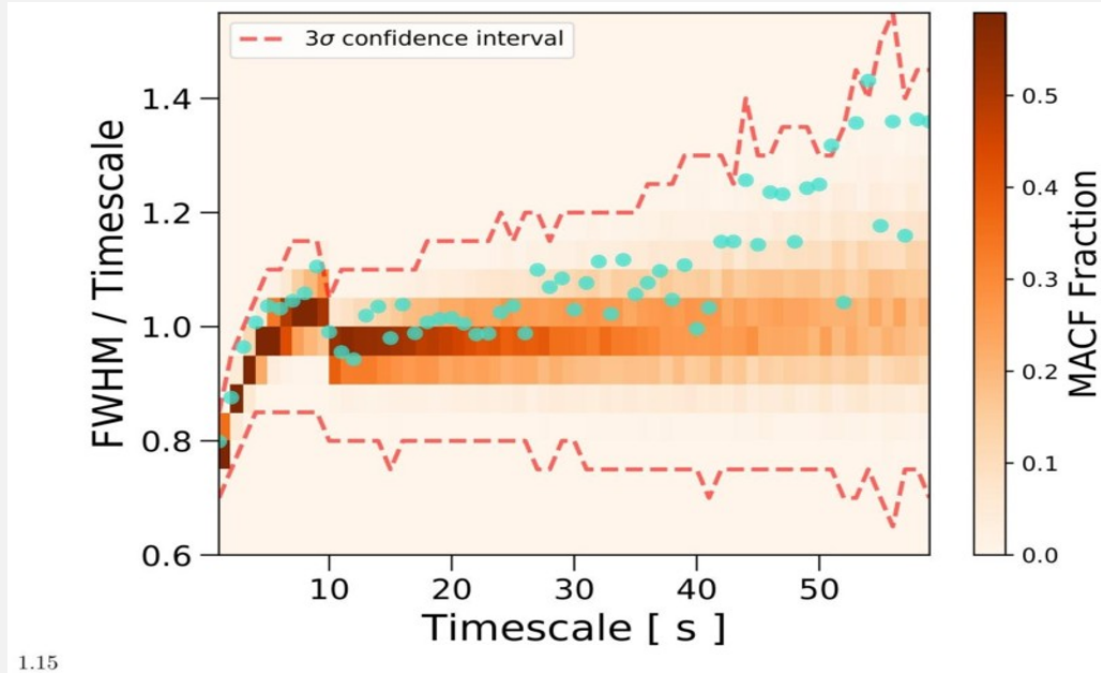
What is the y-axis label for the lower panel?

Answer:

ext. BWD SNR.

Figure 18: Example for visual question-answer pair.

Visual Example

**Question:**

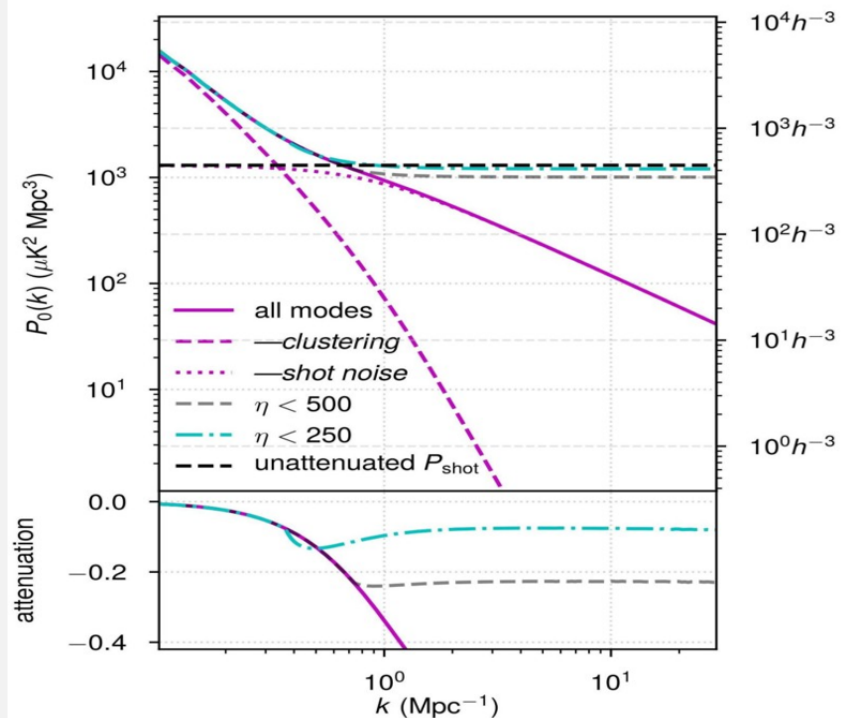
What color are the data points representing VERITAS observations in the graph?

Answer:

The VERITAS observation data points are turquoise or light blue.

Figure 19: Example for visual question-answer pair.

Visual Example



Question:

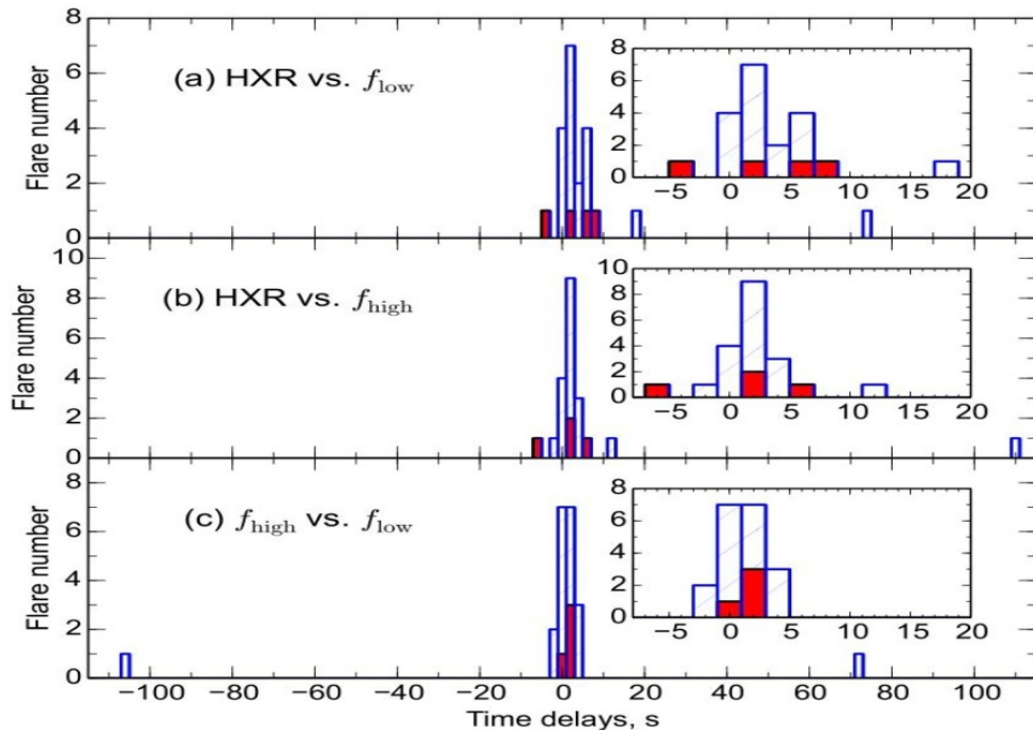
How many different line styles are used in the upper panel of the graph?

Answer:

Four: solid, dashed, dotted, and dash-dotted.

Figure 20: Example for visual question-answer pair.

Visual Example



Question:

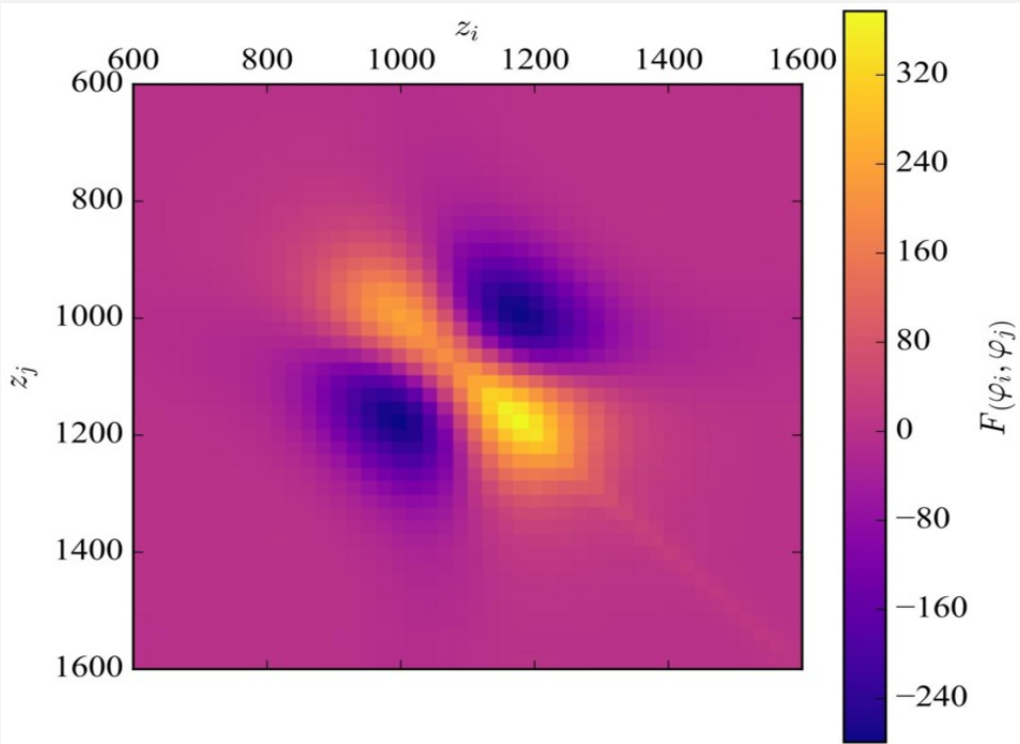
How many subplots are present in the main figure?

Answer:

There are three main subplots labeled (a), (b), and (c).

Figure 21: Example for visual question-answer pair.

Visual Example



Question:

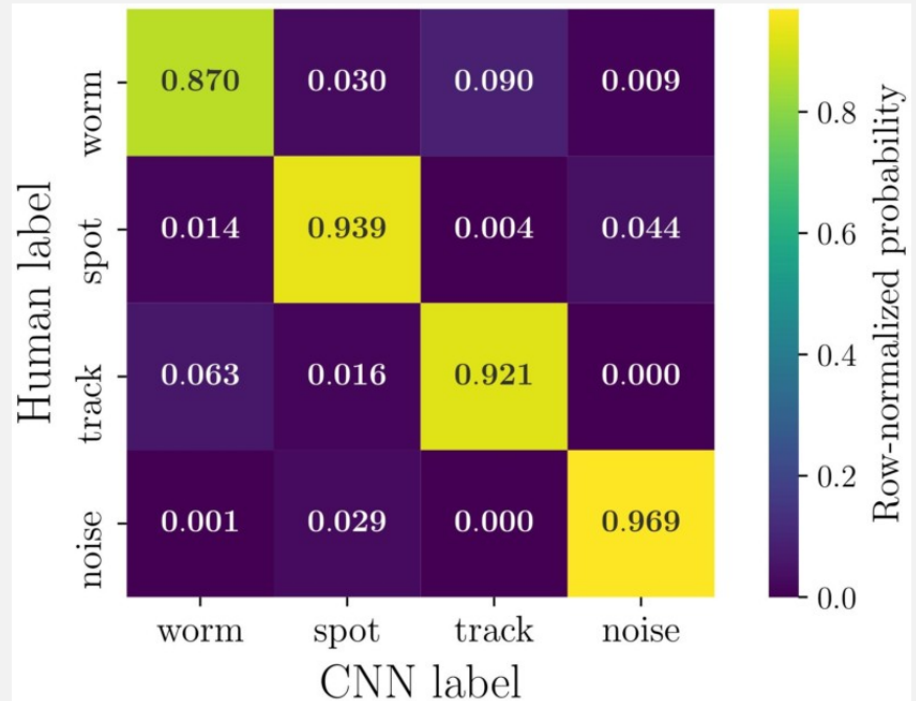
What type of chart is used to represent the data in this image?

Answer:

A marginalised matrix plot or heatmap.

Figure 22: Example for visual question-answer pair.

Data Example

**Question:**

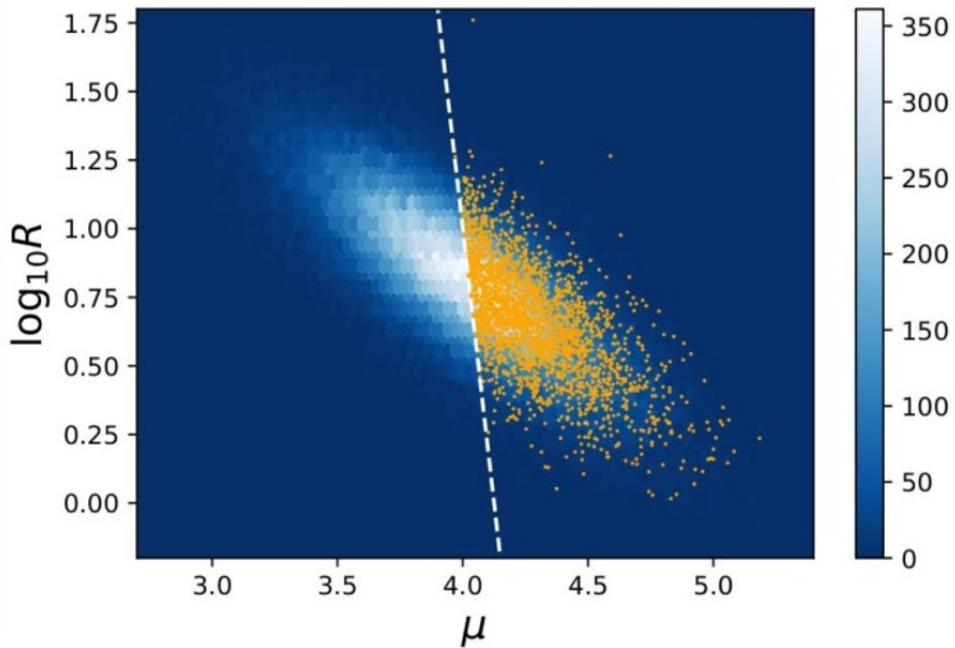
What is the total misclassification rate for the "worm" category?

Answer:

The total misclassification rate for "worm" is 0.13.

Figure 23: Example for data question-answer pair.

Data Example



Question:

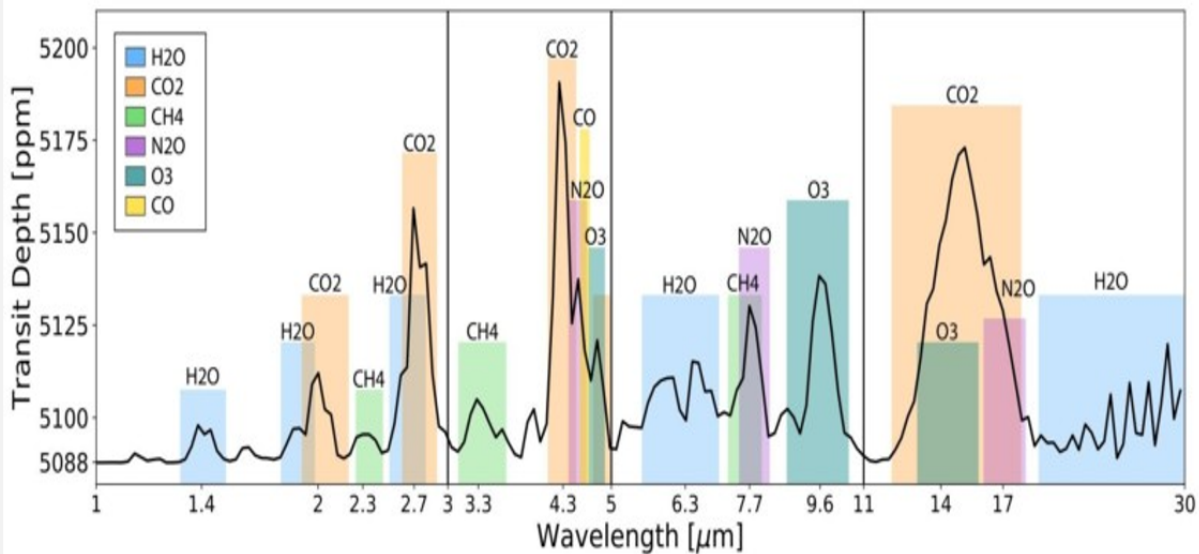
If the selection boundary slope (a_1) was increased by 50%, how would this affect the number of selected galaxies?

Answer:

Increasing the slope would likely reduce the number of selected galaxies, as fewer would fall above the steeper selection line.

Figure 24: Example for data question-answer pair.

Data Example



Question:

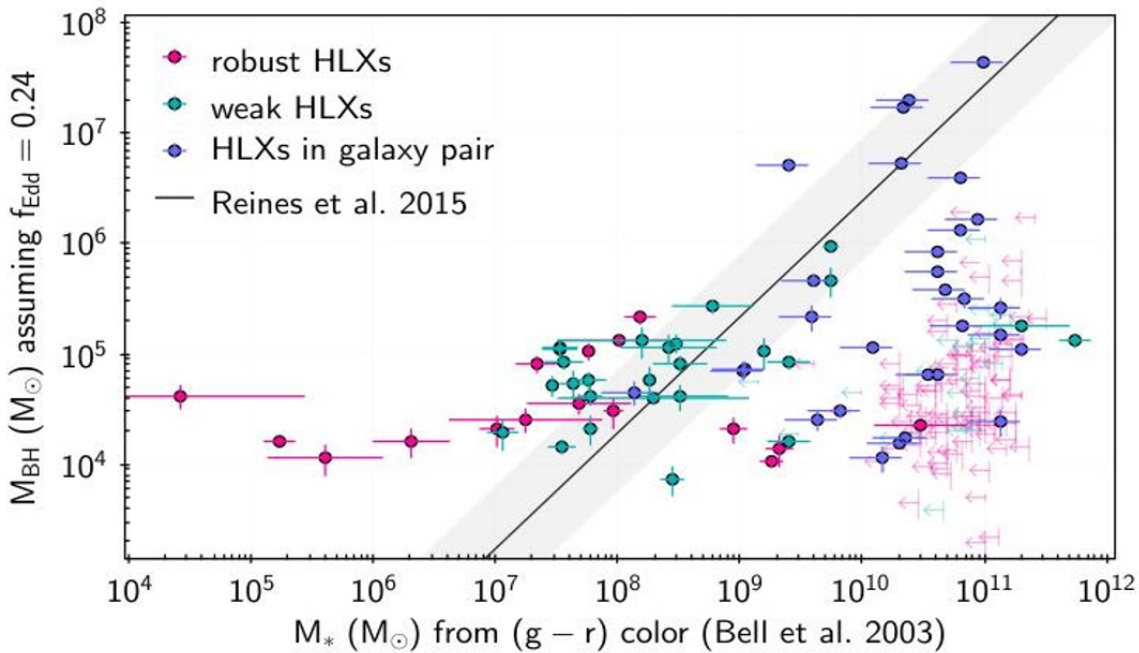
At which transit depth does the first CO₂ band appear in the chart?

Answer:

Approximately 5142 ppm.

Figure 25: Example for data question-answer pair.

Data Example



Question:

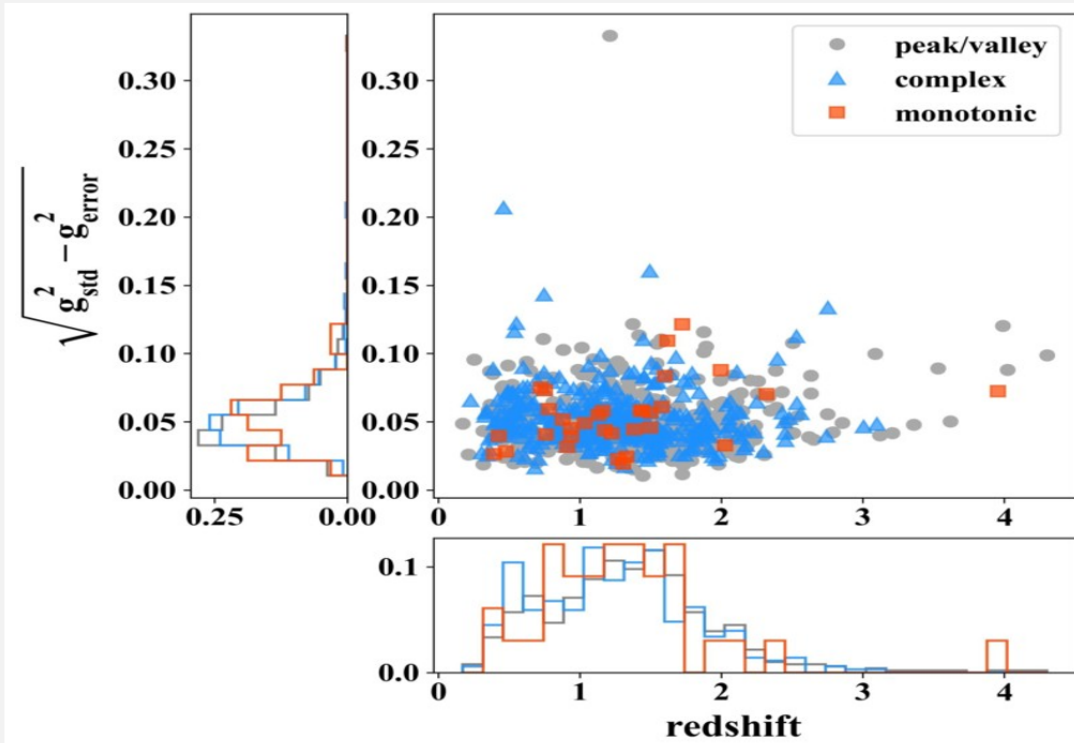
What is the range of the black hole mass among all data points?

Answer:

From 10^3 to 10^8 solar masses.

Figure 26: Example for data question-answer pair.

Data Example



Question:

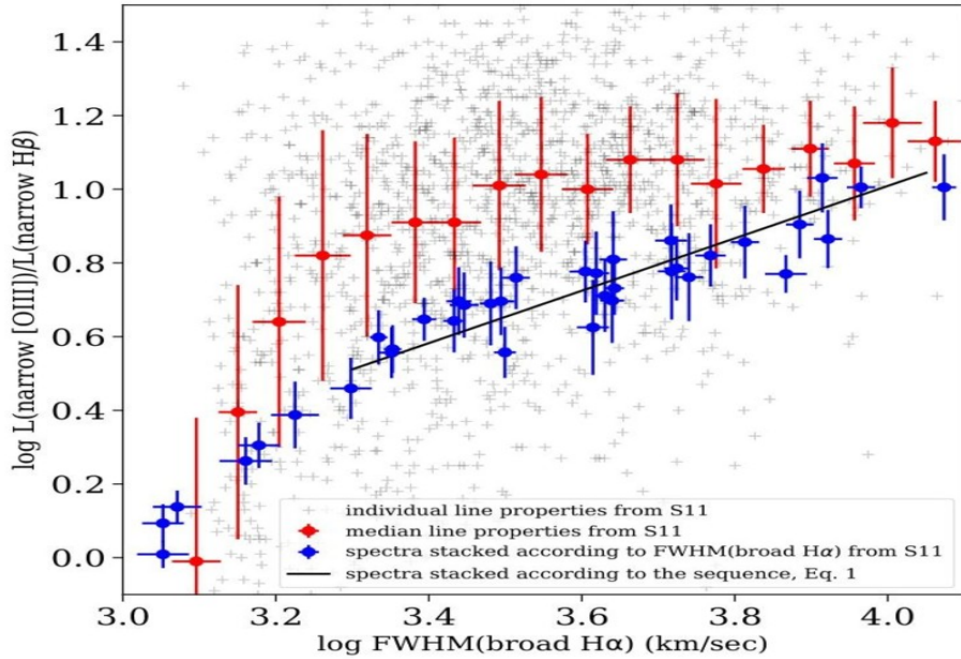
What is the approximate range of redshift values shown in the main scatter plot?

Answer:

From approximately 0.1 to about 4.3.

Figure 27: Example for data question-answer pair.

Inference Example



Question:

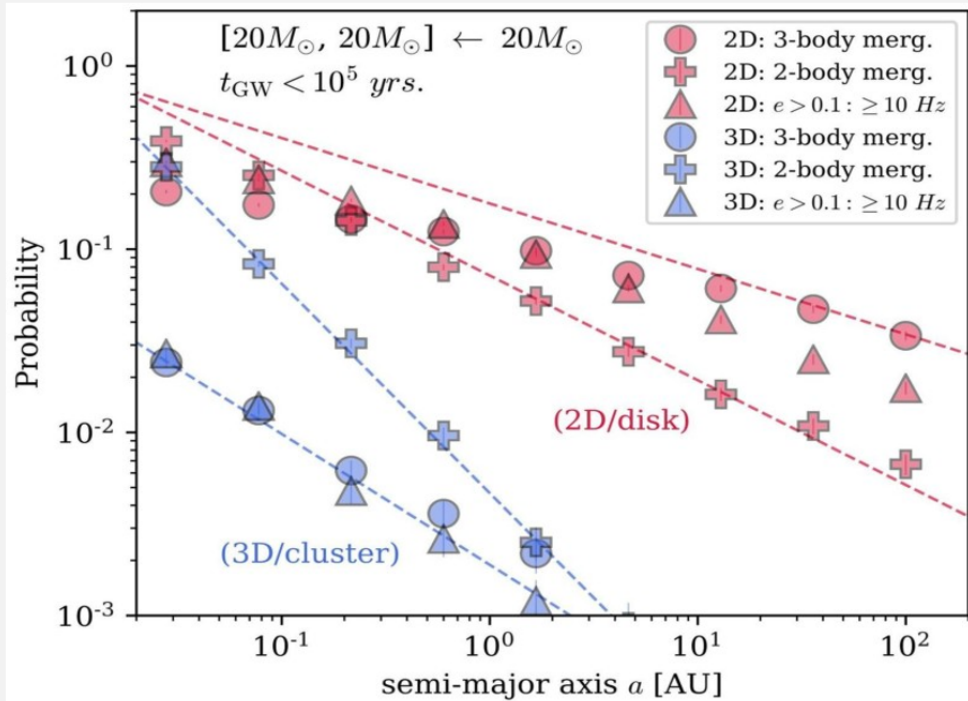
How does the trend of blue data points compare to the black line?

Answer:

The blue points follow the black line closely, with some fluctuations around it.

Figure 28: Example for inference question-answer pair.

Inference Example

**Question:**

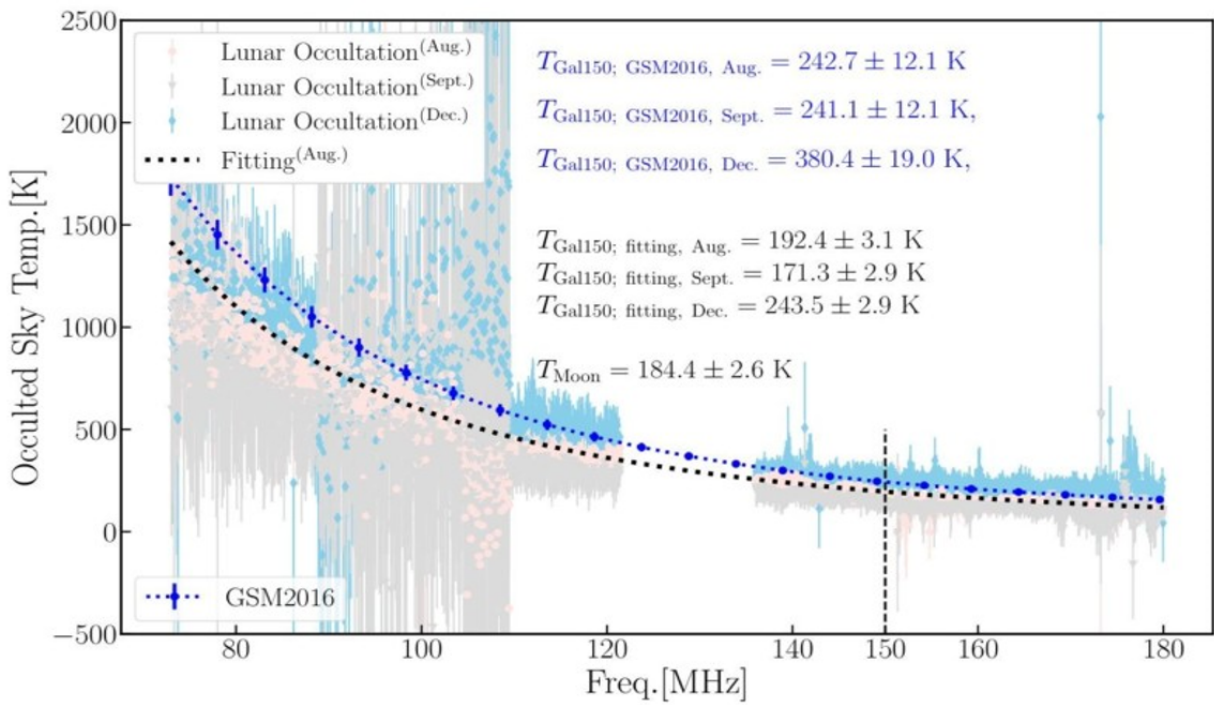
What trend can be observed in merger probabilities as the semi-major axis increases?

Answer:

Merger probabilities generally decrease as the semi-major axis increases for both 2D and 3D interactions.

Figure 29: Example for inference question-answer pair.

Inference Example



Question:

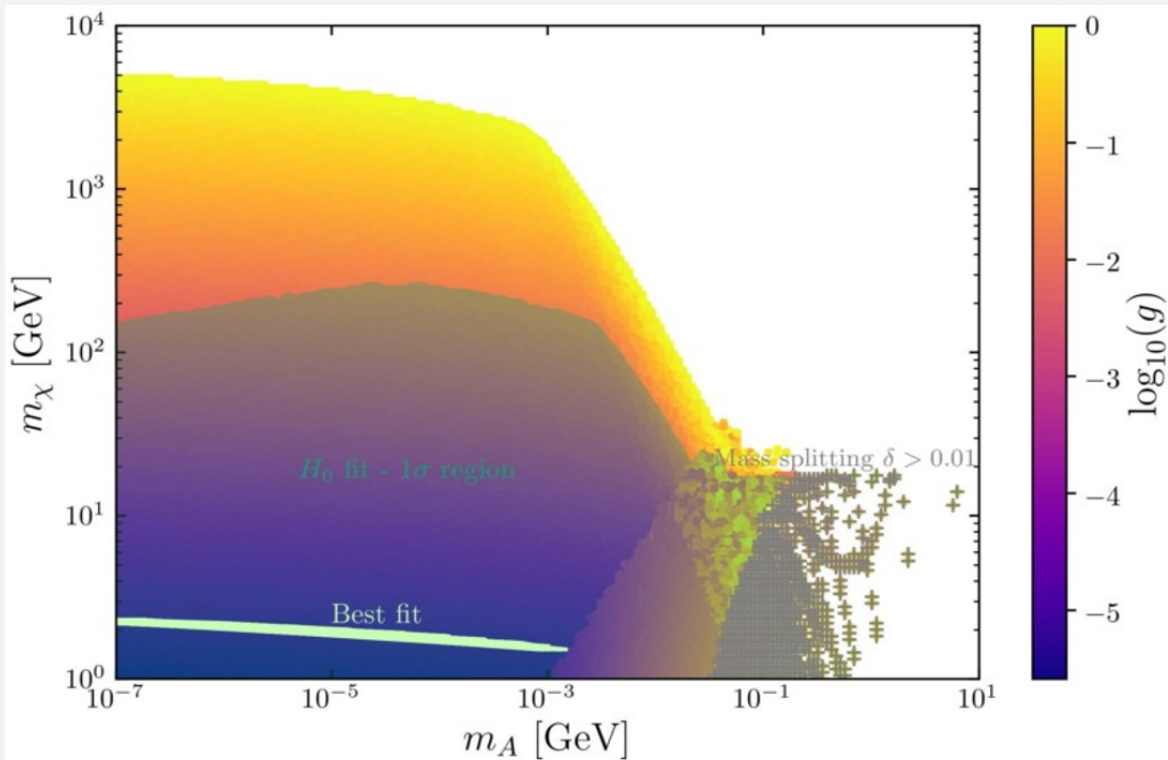
How does the fitted temperature for August compare to the GSM2016 temperature for August?

Answer:

The fitted temperature (192.4 K) is lower than the GSM2016 temperature (242.7 K).

Figure 30: Example for inference question-answer pair.

Inference Example

**Question:**

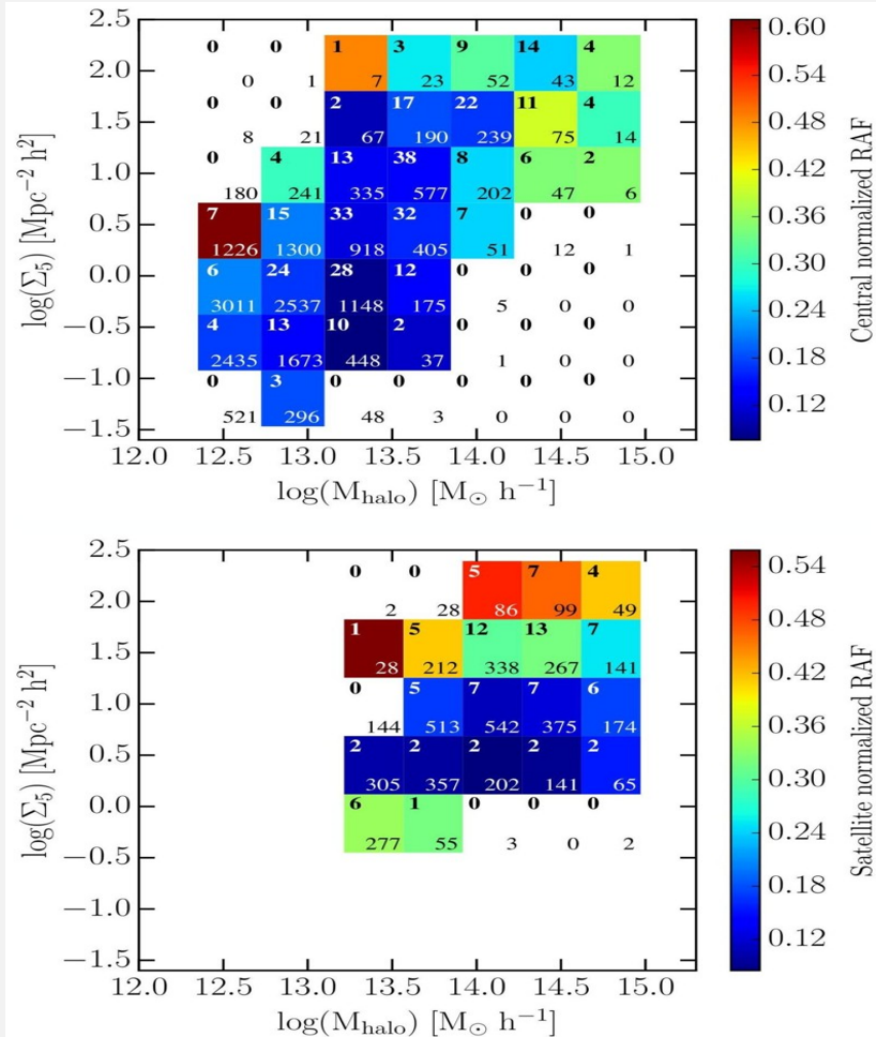
If the mediator mass m_A increases from 10^{-7} GeV to 10^{-3} GeV, how does the maximum allowed dark matter mass m_χ change?

Answer:

The maximum allowed m_χ decreases from about 5000 GeV to approximately 2000 GeV, a reduction of roughly 60%.

Figure 31: Example for inference question-answer pair.

Inference Example



Question:

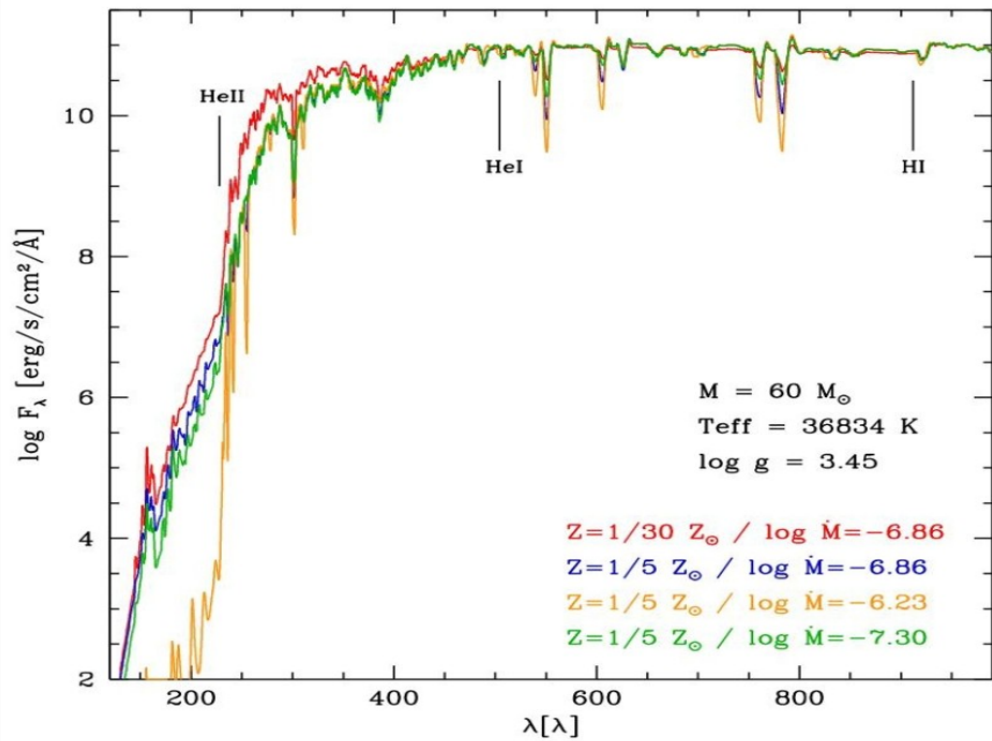
How does the dependence of RAF on local density differ between central and satellite galaxies?

Answer:

Satellite RAF depends on local density, while central RAF shows little dependence.

Figure 32: Example for inference question-answer pair.

Chart Description Example



Question:

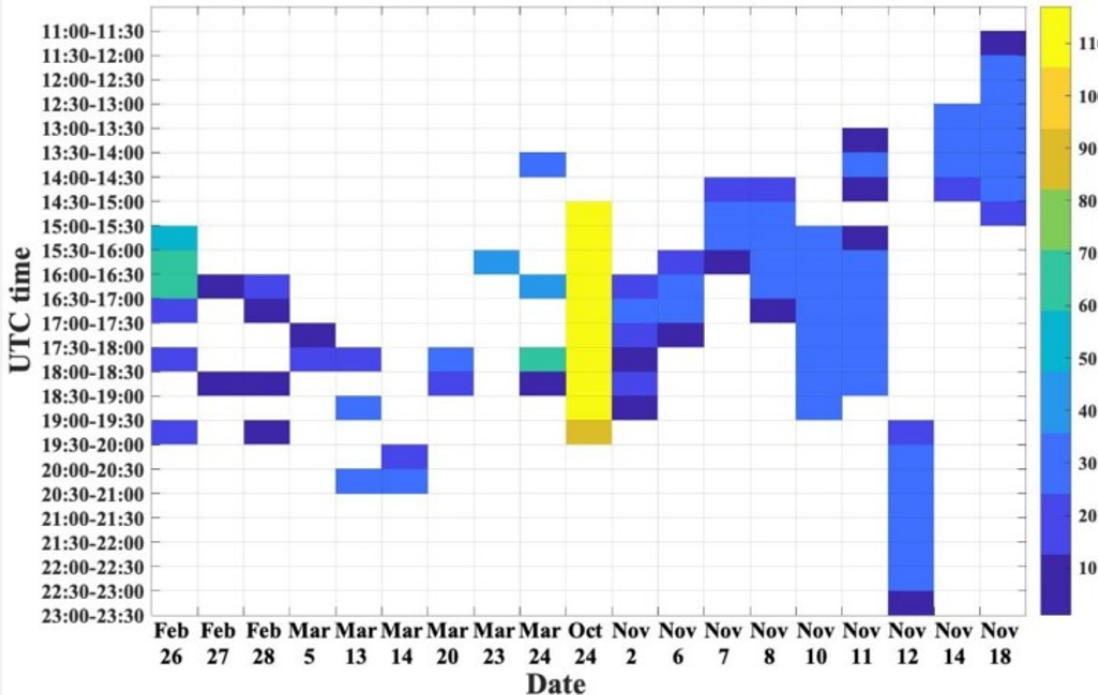
Generate a chart description that aims at presenting all the visual elements of the plot. Answers should be within 100 words.

Answer:

This chart displays spectral energy distributions (SEDs) for a $60 M_\odot$ star model at different metallicities and mass-loss rates. It shows $\log F_\lambda$ versus wavelength (λ) in Angstroms. Four colored lines represent different scenarios: red ($Z=1/30 Z_\odot$), blue ($Z=1/5 Z_\odot$), orange ($Z=1/5 Z_\odot$ with increased mass-loss), and green ($Z=1/5 Z_\odot$ with reduced mass-loss). The graph includes labels for HeII, HeI, and HI ionization edges. Additional model parameters like Teff, $\log g$, and mass are provided. The chart illustrates how metallicity and mass-loss rates affect the star's spectral properties.

Figure 33: Example for chart description question-answer pair.

Chart Description Example



Question:

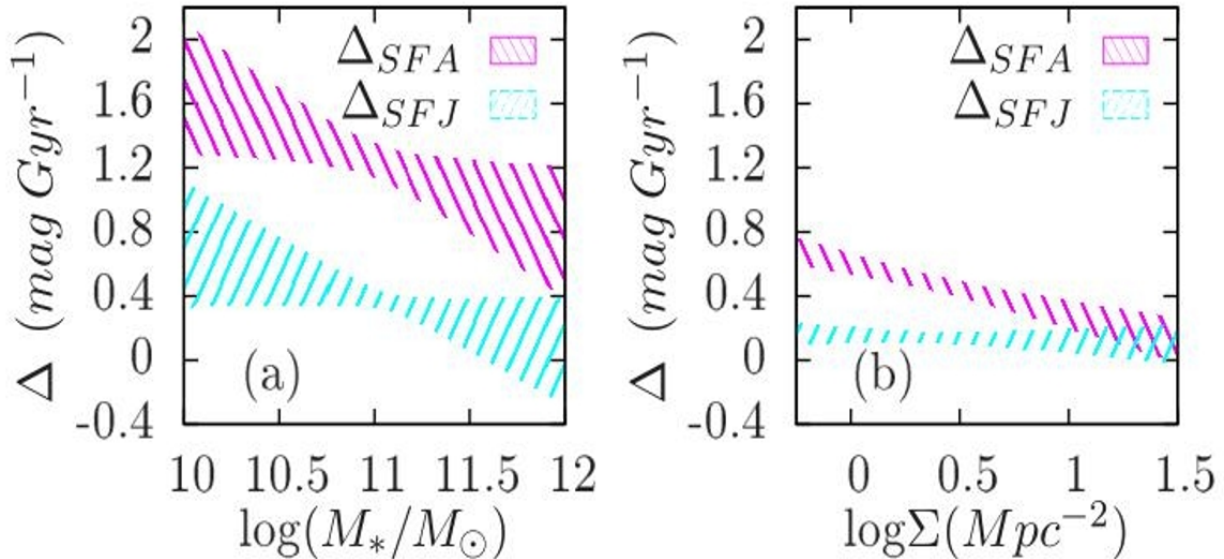
Generate a chart description that aims at presenting all the visual elements of the plot. Answers should be within 100 words.

Answer:

The chart is a heat map showing sodium lidar data availability. The x-axis displays dates from February to November, while the y-axis shows UTC time in half-hour increments from 11:00 to 23:30. Colored grid cells represent data quantity collected in each time slot. Colors range from dark blue (least data) to yellow (most data). The chart reveals patterns in nightly observation periods and data collection intensity across different dates and times.

Figure 34: Example for chart description question-answer pair.

Chart Description Example



Question:

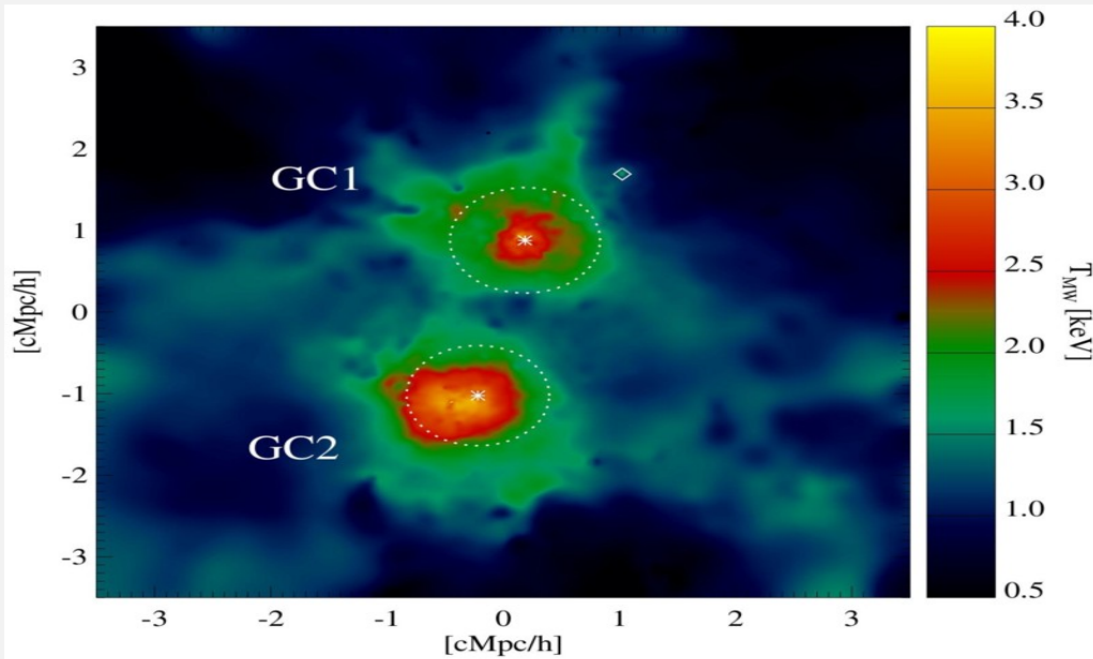
Generate a chart description that aims at presenting all the visual elements of the plot. Answers should be within 100 words.

Answer:

The image contains two side-by-side panels, (a) and (b), showing shaded area plots. Panel (a) displays Δ_{SFA} and Δ_{SFJ} as a function of log stellar mass, while panel (b) shows them as a function of log local environment density. Both use pink/magenta for Δ_{SFA} and light blue/cyan for Δ_{SFJ} . The y-axis represents Δ in mag Gyr^{-1} for both panels. Δ_{SFA} consistently shows higher values than Δ_{SFJ} in both graphs, with both metrics generally decreasing as x-axis values increase.

Figure 35: Example for chart description question-answer pair.

Chart Description Example



Question:

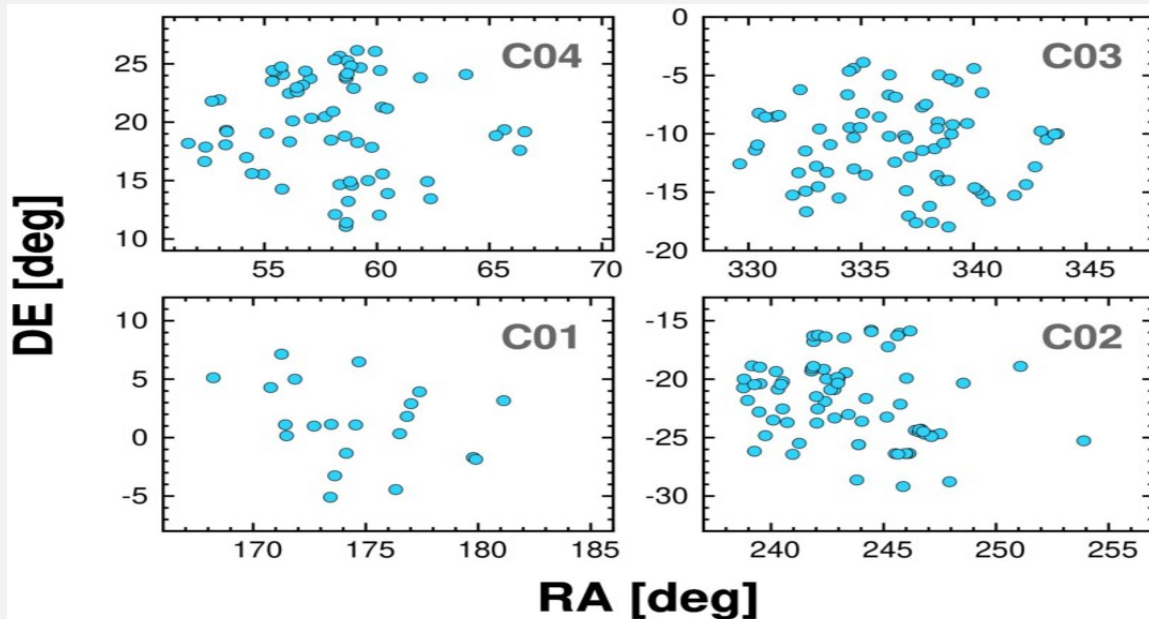
Generate a chart description that aims at presenting all the visual elements of the plot. Answers should be within 100 words.

Answer:

The image shows a projected mass-weighted temperature map of a galaxy cluster pair at $z=0.07$. The map spans 7 cMpc per side, centered on the system's center of mass. Two distinct galaxy clusters, GC1 and GC2, are visible, marked by white dotted circles indicating their r_{500} radii. GC1 is located in the upper half, while GC2 is in the lower half of the image. Both clusters show high-temperature cores (red-orange) surrounded by cooler regions (green-blue). A small diamond symbol in the upper right quadrant marks the position of group B. The temperature scale ranges from 0.5 to 4.0 keV, represented by a color gradient from dark blue to yellow.

Figure 36: Example for chart description question-answer pair.

Chart Description Example



Question:

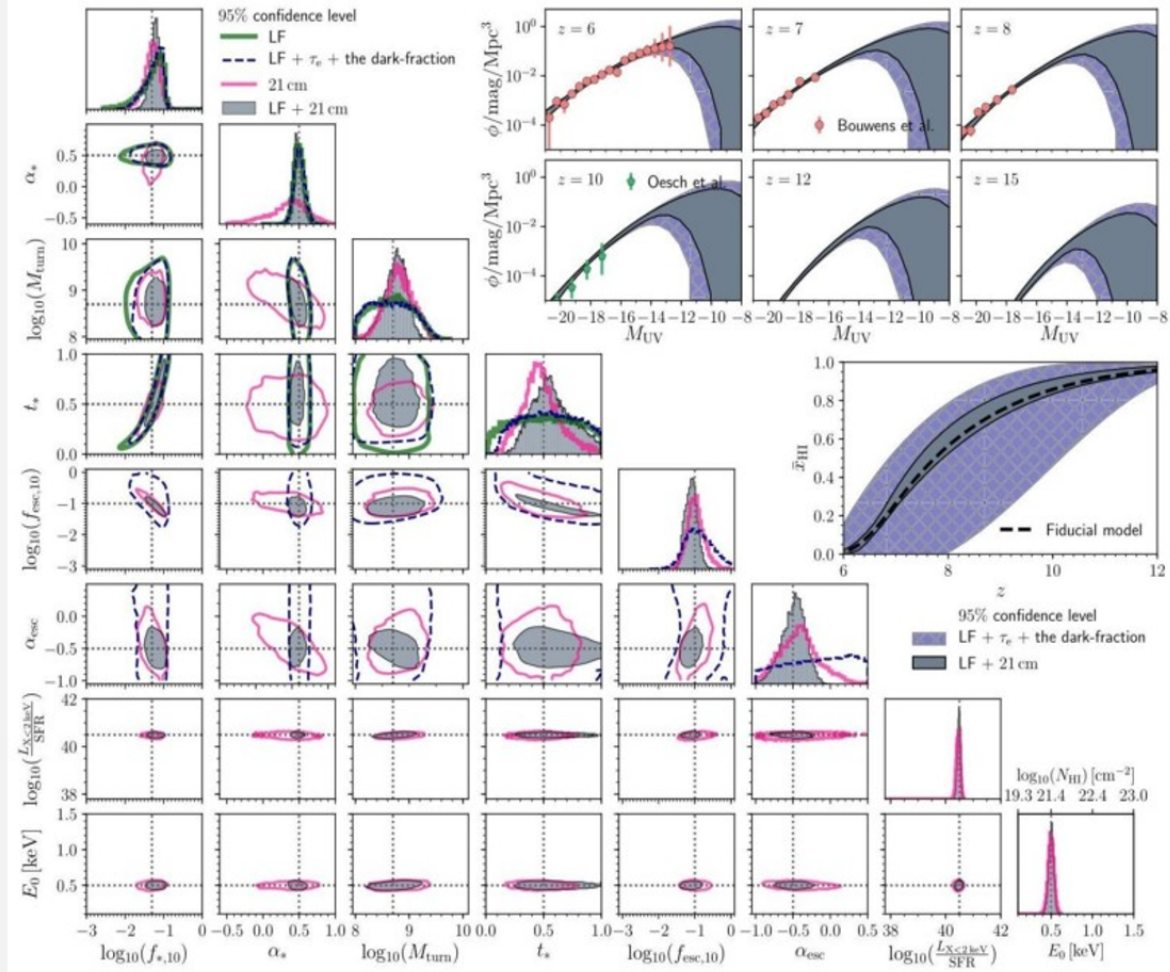
Generate a chart description that aims at presenting all the visual elements of the plot. Answers should be within 100 words.

Answer:

The image consists of four scatter plots arranged in a 2x2 grid, labeled C04, C03, C01, and C02. Each subplot shows light blue data points plotted on axes labeled RA [deg] (x-axis) and DE [deg] (y-axis). The plots display different ranges for both RA and DE values, with C04 and C03 on the top row, and C01 and C02 on the bottom row. The data points in each subplot show varying distributions and densities.

Figure 37: Example for chart description question-answer pair.

KB-Inference Example



Question:

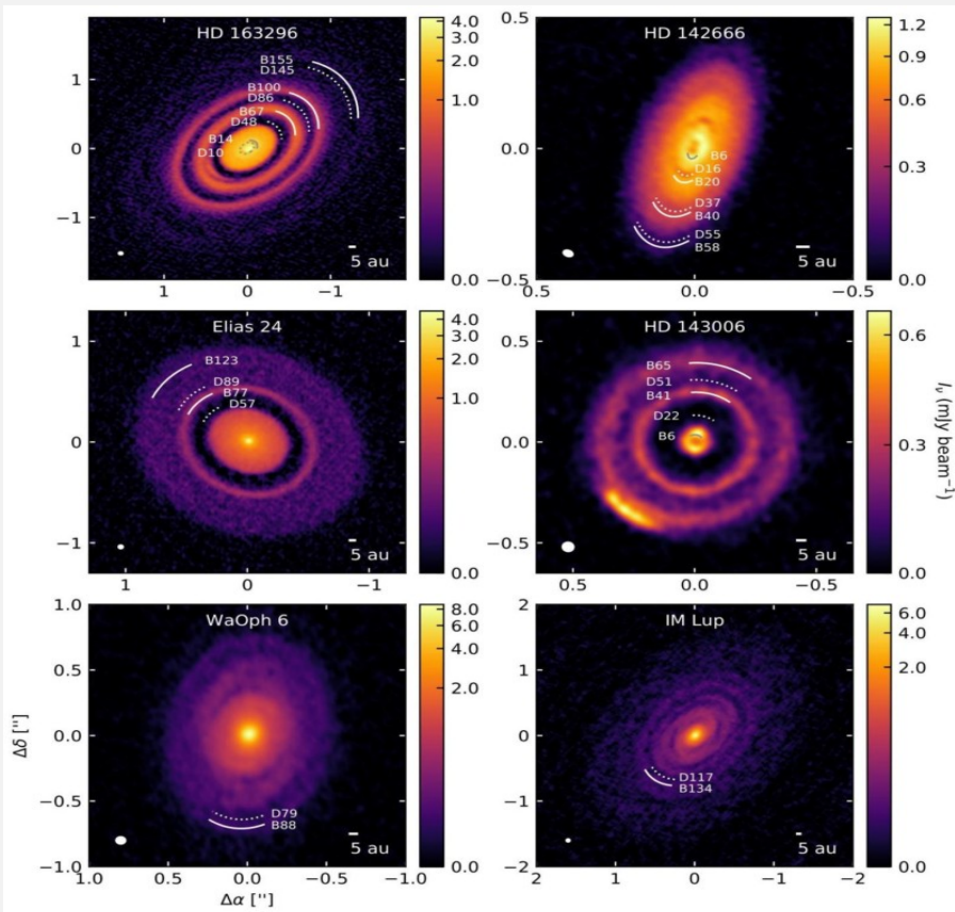
How does the combination of UV luminosity functions and 21-cm data affect the constraints on astrophysical parameters across different redshifts, as shown in the figure?

Answer:

The figure demonstrates that combining UV luminosity functions (LF) with 21-cm data (gray shaded areas) significantly narrows the confidence intervals for astrophysical parameters compared to using LF alone (green contours). This improved constraint is consistent across various redshifts ($z=6$ to $z=15$) shown in the upper right panels.

Figure 38: Example for KB-inference question-answer pair.

KB-Inference Example



Question:

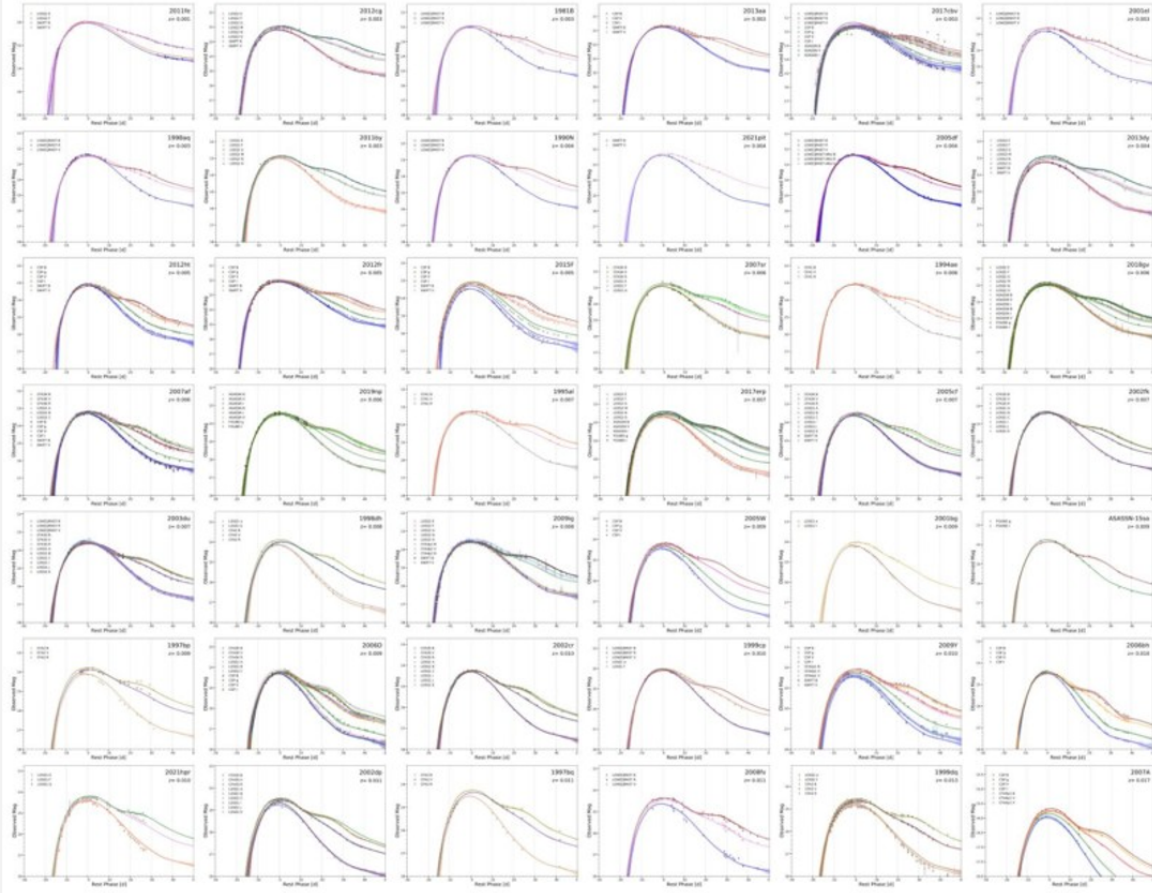
How do the annular substructures in protoplanetary disks vary across different stellar systems, as shown in the image?

Answer:

The image reveals diverse ring and gap patterns in protoplanetary disks around different stars. The structures vary in number, width, intensity, and radial distance from the central star. Some disks, like HD 163296, show multiple distinct rings, while others, like WaOph 6, have fewer visible substructures.

Figure 39: Example for KB-inference question-answer pair.

KB-Inference Example



Question:

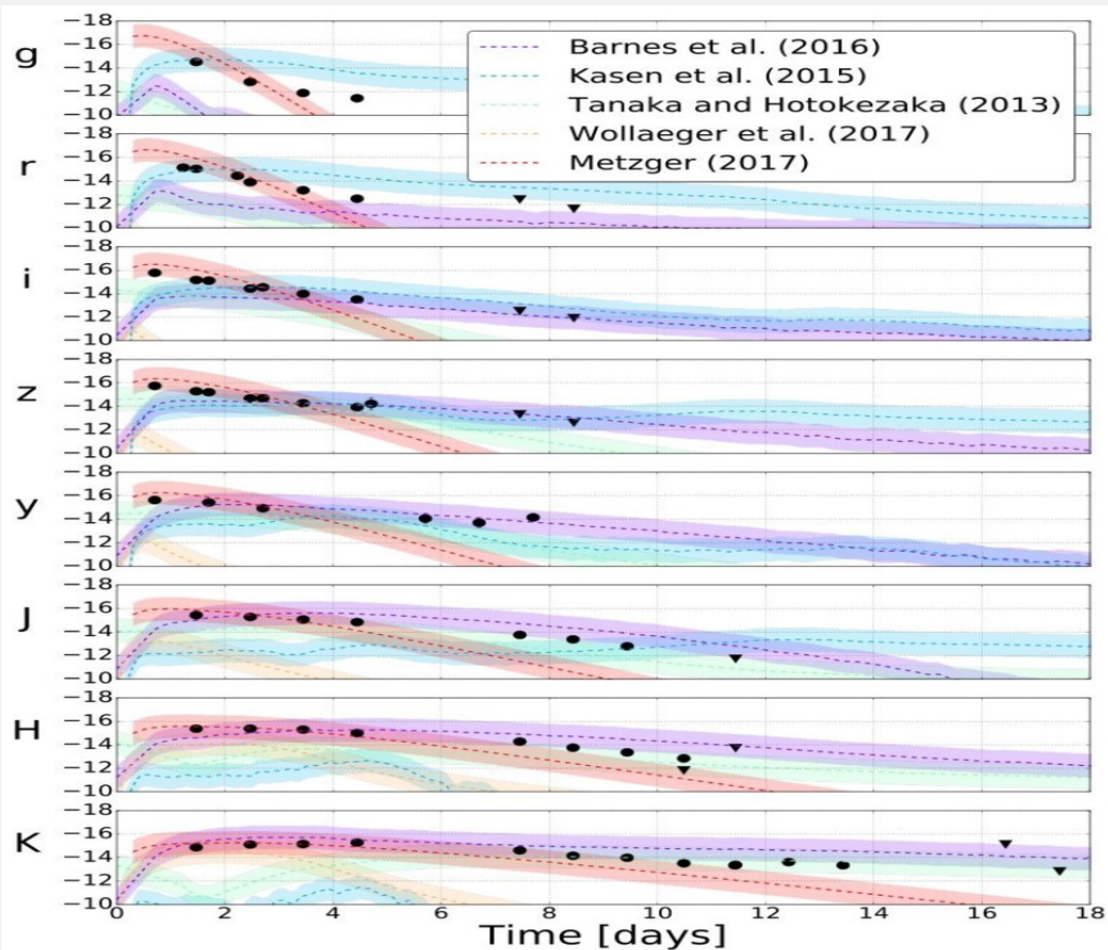
How does the diversity in light curve shapes across different Type Ia supernovae observations contribute to improving the measurement of cosmological parameters?

Answer:

The varied light curve shapes shown in the image reflect the diversity of Type Ia supernovae observations. This diversity, when analyzed across a large dataset, helps refine measurements of cosmological parameters by providing a more comprehensive understanding of supernova behavior and reducing systematic uncertainties.

Figure 40: Example for KB-inference question-answer pair.

KB-Inference Example



Question:

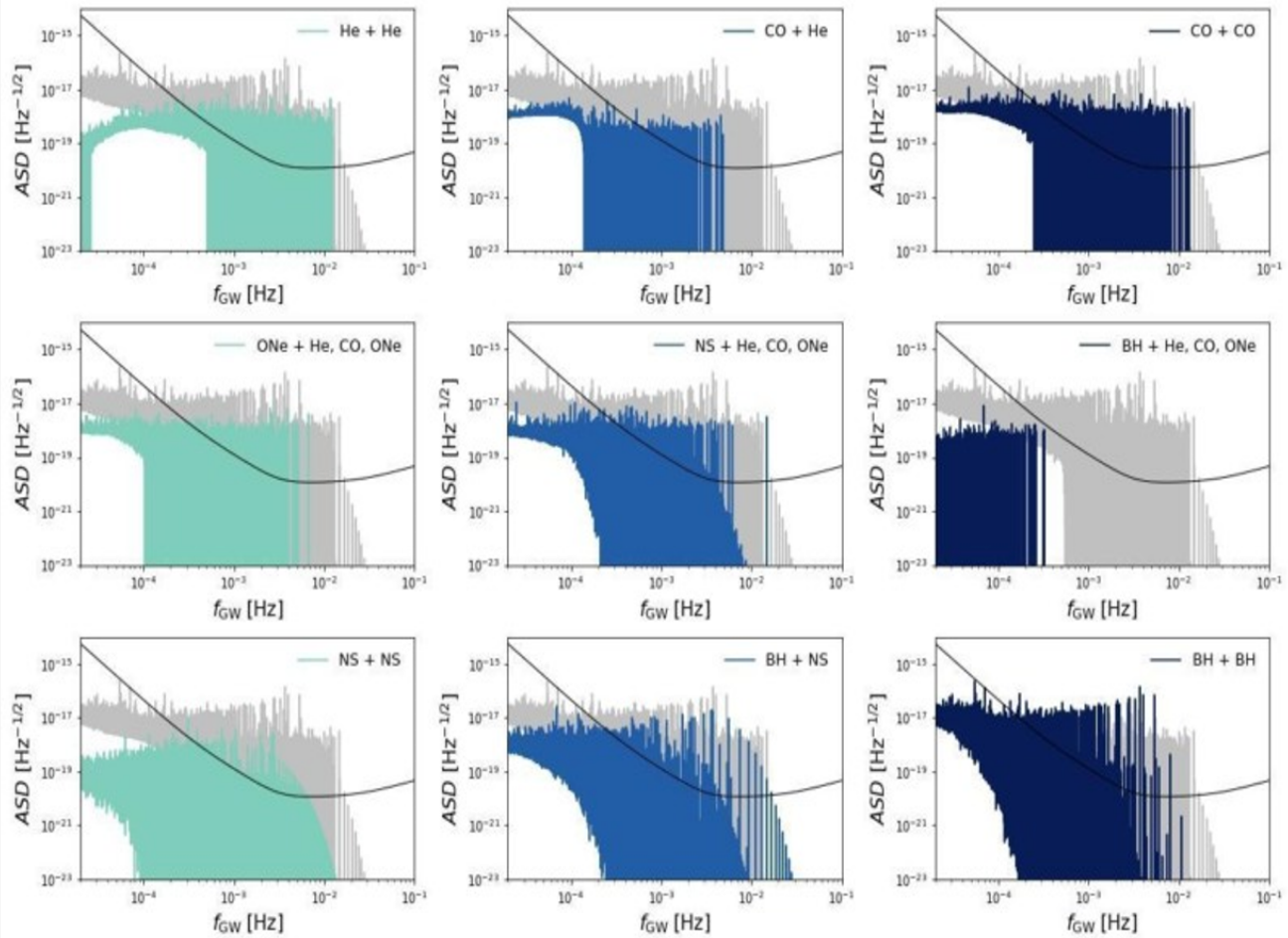
How does the observed data (black dots) in the figure compare to the theoretical models across different wavelength bands, and what does this comparison suggest about the nature of the observed event?

Answer:

The observed data closely follows the theoretical models, particularly those by Barnes et al. and Metzger, across multiple wavelength bands (g, r, i, z, y, J, H, K). This alignment suggests that the observed event exhibits characteristics consistent with kilonova models, supporting the connection between gravitational waves and kilonovae from neutron star mergers.

Figure 41: Example for KB-inference question-answer pair.

KB-Inference Example



Question:

How does the gravitational wave frequency range differ between binary systems containing at least one black hole compared to those without black holes?

Answer:

Binary systems with at least one black hole (BH + He, CO, ONE; BH + NS; BH + BH) show stronger signals at lower frequencies (10^{-4} to 10^{-3} Hz) compared to systems without black holes. This indicates that black hole binaries emit more powerful low-frequency gravitational waves.

Figure 42: Example for KB-inference question-answer pair.

J. Expert Proofreading Website Screenshot

We developed a website (fig. 43) for question-answer pair validation. Validators can log into the website to review the question-answer pairs along with the corresponding research paper excerpts. They can assess the professionalism and accuracy of the pairs by providing scores. If any errors are found, validators can input the correct information as a comment.

AstroCQA Proofreading Annotation

Enter Question ID
0

Question Id: 2527

url

field

title

Massive binaries as the source of abundance anomalies in globular clusters

abstract

Abundance anomalies observed in globular cluster stars indicate pollution with material processed by hydrogen burning. Two main sources have been suggested: asymptotic giant branch (AGB) stars and massive stars rotating near the break-up limit (spin stars). We propose massive binaries as an alternative source. We compute the evolution of a 20 M_{\odot} star in a close binary and find that it sheds about 10 M_{\odot} . The ejecta are enriched in He, N, Na, and Al and depleted in C and O, similar to the abundance patterns observed in globular cluster stars. In contrast to the fast, radiatively driven winds of massive stars, this material is typically ejected with low velocity. We expect that it remains inside the potential well of a globular cluster and becomes available for the formation or pollution of a second generation of stars. We estimate that the amount of processed low-velocity material ejected by massive binaries is greater than the contribution of AGB stars and spin stars combined, assuming that the majority of massive stars in a post-globular cluster interact. If we take the possible contribution of intermediate mass stars in binaries into account and assume that the ejecta are diluted with an equal amount of unprocessed material, we find that this scenario can provide enough material to form a second generation of low-mass stars, which is as numerous as the first generation of low-mass stars. In this scenario there is no need to make commonly adopted assumptions, such as preferential loss of the first generation of stars, external pollution of the cluster, or an anomalous initial mass function. [Abridged]

summary

We propose massive binaries as a source for the internal pollution of globular clusters. The majority of massive stars are expected to be members of interacting binary systems. These return most of the envelope of their primary star to the interstellar medium during non conservative mass transfer. We show that there may be more polluted material ejected by binaries than by the two previously suggested sources: massive AGB stars and the slow winds of fast-rotating massive stars. After dilution with pristine material, as lithium observations suggest, binaries could return enough material to form a chemically enriched second generation that is as numerous as the first generation of low-mass stars, without the need to assume a highly anomalous IMF, external pollution of the cluster or a significant loss of stars from the unenriched first generation.

In addition to providing a new source of slowly-ejected enriched material, binary interaction also affects the previously proposed scenarios. Binary mass transfer naturally produces a large number of fast-rotating massive stars that may enrich their surroundings even more. Binary interaction will also affect the yields of intermediate-mass stars. Premature ejection of the envelope in 4-9 M_{\odot} stars will result in ejecta with less pronounced anti-correlations, as suggested in the AGB scenario. On the other hand, we expect that binary-induced mass loss may also prevent the dredge-up of helium-burning products.

For a detailed comparison of the chemical predictions of this scenario, binary models (for a range of masses and orbital periods) are needed and population synthesis models are essential to fully evaluate the mass budget of the different sources. [Finally, some peculiar feature, such as the apparent presence of distinct, chemically homogeneous subpopulations in ω_{Cen} and ω_{Cen} deserves further attention.]

\begin{begin}

caption

\caption{Composition of the slow ejecta of the modeled binary system (Sec.-3) as a function of the ejected amount of mass. The mass fraction X of the main stable isotope of each element is given relative to the initial mass fraction X_i , except for Mg where we added ^{24}Mg , ^{25}Mg and ^{29}Mg . The average X_{av} and the most extreme mass fraction X_{ext} are given in each panel on a logarithmic scale: $[X] \equiv \log_{10}(X/X_i)$. For helium we show the absolute mass fraction Y instead. Mass ejected during the first and second mass transfer phases is separated by a thin vertical line. \label{fig:chem}}

related conclusion for figure

The figure supports the conclusion that massive binary stars can eject large amounts of processed material with low velocity, which remains within the cluster's potential well. This material is enriched in He, N, Na, and Al, and depleted in C and O, matching observed patterns in globular cluster stars. The figure provides direct evidence for the chemical composition changes proposed in the paper's conclusion, supporting the idea that massive binaries could be a significant source of abundance anomalies in globular clusters.

question

How does the abundance of nitrogen in the ejected material change as the ejected mass increases, and what implications does this have for globular cluster composition?

answer

The graph shows nitrogen abundance increasing significantly with ejected mass, reaching $[X_{\text{av}}] = 0.98$ and $[X_{\text{ext}}] = 1.44$. This indicates that as massive binary stars eject more material, it becomes increasingly enriched in nitrogen, potentially contributing to the nitrogen enhancement observed in globular cluster stars.

Professionalism (Does the question reflect the perspective of an astronomer? 1 = least professional, 5 = most professional)

null 1 2 3 4 5

Accuracy

null Correct Unknown Incorrect

Submit

Figure 43: Screenshot of the expert proofreading website for QA validation, where validators review question-answer pairs with research excerpts, rate professionalism, and accuracy, and provide corrections or comments.

K. Details of Evaluation Metrics

In this appendix, we detail the evaluation framework used to assess both numerical responses and open-ended responses, as described in the main text.

K.1. Evaluation of Numerical Responses

For numerical responses, we categorize evaluation into data retrieval and data derivation. Data retrieval focuses on extracting specific data points or value ranges from charts. Data derivation involves structural element prediction (e.g., number of bars, colors, legends) and math reasoning.

Data Retrieval Evaluation. To ensure a scale-aware evaluation, we normalize the relative error using the axis range. The scoring process follows algorithm 3.

Algorithm 3: Numerical Value Extraction and Scoring

Require: Reference values, Predicted values

Ensure: Final Score as S_{final}

```

1: procedure SCOREVALUES(Reference, Prediction)
2:   Extract numerical values from both Reference and Prediction
3:   if Number of reference values > Number of predicted values then
4:     return  $S_{final} = 0$ 
5:   else if Number of predicted values > Number of reference values then
6:     Compute the mean of predicted values
7:   end if
8:   Construct pairs  $V_i = \{(Predict_i, True_i)\}$ 
9:   if Chart axis is logarithmic then
10:    Apply logarithmic transformation (or retain exponent)
11:   end if
12:   Initialize  $S_{final} = 0$ 
13:   for each pair  $V_i$  do
14:     Compute relative error  $R_i$ :
```

$$R_i = \frac{|True_i - Predict_i|}{D_{range}}$$

where D_{range} is length of the axis.

15: Compute Score S_i :

$$S_i = (1 - R_i) \times I((1 - R_i) > 0.9)$$

16: Accumulate Score

17: **end for**

18: Compute Final Score:

$$S_{final} = \frac{1}{N} \sum_{i=1}^N Score_i$$

19: **return** S_{final}

20: **end procedure**

Data Derivation Evaluation. For data derivation, an LLM extracts numerical values, and correctness is determined by exact numerical matching, ensuring that only fully correct answers are considered accurate.

K.2. Evaluation of Open-ended Responses

We employ an LLM-based judging framework to evaluate open-ended responses. A dedicated judging model assigns a score between 0 and 1 based on predefined criteria, ensuring consistency and scalability. Our approach first extracts key points from both the generated and reference answers, then performs fine-grained matching to assess correctness. The final score is computed using an averaging strategy, providing a more nuanced evaluation. The evaluation prompt design is illustrated in fig. 44.

Prompt for Evaluation MLLM

You will receive a question, a standard answer, and a model's response. Your task is to assess whether the model's response is correct.

Criteria:

Accuracy (0-1): Evaluate how closely the model's response matches the standard answer.

Final Score: Calculate the average score for all key points.

Steps:

- 1. Understand the Question:** Read and comprehend the question.
- 2. Analyze the Answers:** Read the standard answer and the model's response. Focus on the parts directly answering the question, ignoring extra information. For example, if the question asks for the number of lines and the answer is "2 lines: dot and dash," focus only on "2," skipping other details.
- 3. Compare Responses:** Evaluate similarities and differences between the model's response and the standard answer. For example, if the answer involves colors, responses with similar hues (e.g., blue vs. purple) should be rated higher.
- 4. Assign Accuracy Scores (0-1) for Each Key Point:**
 - 1:** Identical or nearly identical.
 - 0.8-0.9:** Thematically aligned with minor differences.
 - 0.5-0.7:** Partially correct with errors.
 - 0.3-0.4:** Loosely related with some relevant information.
 - 0.1-0.2:** Minimal relevant information.
 - 0:** Completely inaccurate; numerical/OCR responses must match exactly.
- Omitted Key Points:** If a key point is completely missing from the model's response, it receives a score of 0.
- 5. Compute the Final Score:** Calculate the average accuracy score for all key points.

Example 1:

Question: What line styles are used for A and B?

Standard answer: Blue dash-dot line and red dot line.

Model's response: Dash-dot line style for A and dot line for B.

You should response: 1

Another model's response: Dashed and dot.

You should response: 0.5

Example 2:

Question: What is the title used for the y-axis in the chart?

Standard answer: The y-axis is labeled as E(v_n).

Model's response: E(r_n)

You should response: 0

Another model's response: E(v).

You should response: 0

Now start the evaluation:

Question:

{question}

Standard Answer:

{answer}

Model's Response:

{pred}

Your response (score ONLY without reason):

Figure 44: Prompt for evaluation MLLMs.

Other Evaluation Metrics and Results

We further evaluate the models using L3Score(table 8), BLEU-4(table 9), and ROUGE-L(table 10), which are commonly used metrics for assessing text generation quality. L3Score captures semantic alignment in long-form answers, BLEU-4 evaluates n-gram precision, and ROUGE-L measures lexical overlap. In the following tables, bold numbers indicate the best-performing model among proprietary and open-source MLLMs, respectively.

Model	FQA												AQA			
	Visual						Data						Inference	Chart Desc.	KB-Infer.	Overall
	All	color	style	text	layout	All	point	interval	calculation							
Proprietary Multimodal Large Language Models																
Gemini-2.5-pro	89.18	85.97	85.82	93.76	92.50	72.15	78.22	71.72	63.29	80.24	94.94	75.82	84.07			
Gemini-2.5-flash	86.06	83.69	86.46	89.30	82.03	64.88	65.32	63.86	65.45	80.86	95.18	73.41	81.49			
GPT-4o	85.90	85.48	82.53	87.11	91.12	52.03	50.72	59.86	44.57	73.80	93.16	71.84	77.29			
Qwen-VL-Max	82.29	83.97	69.84	86.41	89.35	51.76	50.74	58.87	44.71	71.17	87.71	66.84	74.00			
Open-source Multimodal Large Language Models																
TinyChart-3B	24.99	38.65	20.89	14.84	18.45	12.61	18.47	9.38	7.44	14.20	0.33	3.73	14.15			
Llava1.5-7B	23.02	33.48	19.12	15.20	20.20	8.06	8.11	8.47	7.48	34.75	0.00	26.17	18.45			
Llava1.6-mistral-7B	37.54	46.12	30.67	32.49	38.14	14.97	17.76	14.64	11.04	36.66	1.94	27.08	25.69			
Qwen-VL-Chat-7B	37.02	41.70	32.47	33.35	42.56	11.23	15.34	7.68	9.18	29.89	0.82	22.35	22.94			
deepseek-janus-pro-7B	62.22	65.42	61.55	58.04	67.85	31.73	35.11	39.96	16.49	49.97	35.66	36.16	46.89			
MiniCPM-V2.6-8B	67.06	68.72	53.05	76.14	56.68	33.61	32.71	44.64	21.59	46.33	46.67	40.04	50.72			
InternVL3-8B	63.19	65.87	54.05	64.27	69.46	34.92	37.73	43.80	19.77	47.68	35.58	43.04	48.16			
mPLUG-Owl2-8.2B	21.57	26.45	20.79	16.73	21.77	10.00	10.39	11.26	7.86	27.86	0.00	18.08	16.25			
Pixtral-12B	76.73	76.30	71.72	79.61	76.76	50.12	51.40	61.55	34.26	69.10	87.80	61.80	70.83			
Llava1.6-vicuna-13B	41.81	51.19	33.95	38.25	34.10	13.69	16.31	11.35	12.49	34.46	2.13	31.91	27.14			
SPHINX-v2-13B	26.14	34.57	23.65	21.19	14.77	6.83	12.65	1.47	4.36	26.11	0.00	21.32	17.34			
Llama-4-Maverick-17B	82.04	80.05	73.37	88.43	85.49	56.75	53.72	61.56	55.61	73.92	85.07	69.83	75.16			
CogVLM2-19B	61.51	70.16	45.00	63.81	58.24	26.59	27.63	35.52	14.16	43.97	34.81	31.60	44.01			
Gemma-3-27B	67.18	64.81	61.15	69.81	80.38	35.66	34.10	49.48	21.30	52.94	53.19	52.70	54.80			
Llava1.6-34B	45.17	52.36	37.01	43.61	39.01	18.19	16.18	24.85	13.23	39.38	8.38	42.14	32.24			
Qwen2.5-VL-72B	81.92	82.16	72.06	88.16	78.01	52.87	51.53	60.09	46.17	68.73	89.09	65.01	73.70			
Pixtral-large-124B	85.30	83.13	79.31	90.85	84.23	56.96	59.22	65.84	42.66	77.66	91.25	70.05	78.12			
Fine-tuned																
MiniCPM-V2.6-8B-fine-tuned	74.82	72.47	70.52	78.00	81.38	37.68	37.70	50.59	21.97	52.64	52.23	41.20	56.45			

Table 8: Accuracy (%) on AstroChart benchmark using L3Score.

Model	FQA										AQA			
	Visual					Data					Inference	Chart Desc.	KB-Infer.	Overall
	All	color	style	text	layout	All	point	interval	calculation					
Proprietary Multimodal Large Language Models														
Gemini-2.5-pro	19.48	20.91	15.64	21.71	12.54	12.97	14.16	13.98	9.89	7.16	9.32	9.88	13.31	
Gemini-2.5-flash	25.14	30.61	20.86	23.51	18.58	12.81	12.87	13.54	11.81	7.93	9.46	10.66	15.54	
GPT-4o	21.26	23.42	20.64	21.61	11.07	10.83	11.91	11.10	8.84	11.41	12.69	15.00	15.43	
Qwen-VL-Max	21.34	22.91	20.32	23.27	7.27	11.90	12.61	13.26	9.12	12.34	11.83	11.15	15.25	
Open-source Multimodal Large Language Models														
TinyChart-3B	3.00	6.20	1.81	1.05	0.77	0.61	0.24	1.30	0.34	3.99	1.61	4.52	2.64	
Llava1.5-7B	2.47	5.18	0.44	1.39	0.62	0.95	0.86	1.05	0.96	15.36	2.83	9.00	5.15	
Llava1.6-mistral-7B	5.40	8.11	1.83	5.45	2.90	6.12	6.24	3.49	9.14	2.69	2.98	3.44	4.43	
Qwen-VL-Chat-7B	2.87	2.35	0.69	5.02	1.36	0.55	0.37	1.20	0.04	14.06	5.06	8.39	5.33	
deepseek-janus-pro-7B	10.57	9.98	11.01	11.49	7.09	11.39	11.32	8.82	14.62	11.66	10.26	11.85	10.99	
MiniCPM-V2.6-8B	14.09	14.43	12.10	17.33	2.40	5.67	5.22	8.12	3.39	9.23	8.25	10.84	10.29	
InternVL3-8B	16.95	20.52	13.58	17.36	8.90	11.10	11.21	12.61	9.11	9.96	7.33	9.04	12.10	
mPLUG-Owl2-8.2B	2.42	3.56	0.62	2.11	3.87	0.90	0.59	1.49	0.66	15.50	2.78	8.65	5.10	
Pixtral-12B	14.37	13.30	13.44	16.49	11.78	8.25	7.75	8.05	9.25	7.99	10.78	11.64	11.20	
Llava1.6-vicuna-13B	5.33	7.55	1.26	5.75	4.78	0.78	0.58	1.23	0.56	12.71	4.61	8.88	5.99	
SPHINX-v2-13B	1.52	2.12	0.39	1.82	0.58	0.06	0.09	0.07	0.01	13.17	2.70	9.39	4.29	
Llama-4-Maverick-17B	14.05	13.92	11.09	16.73	10.05	9.27	10.29	9.28	7.66	8.54	12.64	14.10	11.97	
CogVLM2-19B	11.43	9.09	7.65	16.91	7.19	6.64	5.40	6.34	8.93	13.25	8.22	9.60	10.08	
Gemma-3-27B	14.49	14.52	16.05	15.49	5.67	7.19	7.26	6.23	8.23	7.85	10.07	8.72	10.58	
Llava1.6-34B	5.57	8.27	1.51	5.69	4.14	1.53	1.06	2.63	0.91	13.60	5.38	10.49	6.68	
Qwen2.5-VL-72B	19.83	20.42	18.61	22.27	9.81	12.61	14.91	13.37	8.13	11.14	12.10	12.51	14.83	
Pixtral-large-124B	21.52	24.57	19.46	21.52	12.74	15.46	15.06	15.29	16.27	10.51	15.01	16.02	16.75	
Fine-tuned														
MiniCPM-V2.6-8B-fine-tuned	31.09	33.14	32.58	31.19	15.03	11.52	12.78	11.52	9.57	10.02	14.77	14.56	19.14	

Table 9: Accuracy (%) on AstroChart benchmark using BLEU-4.

Model	FQA												AQA			
	Visual						Data						Inference	Chart Desc.	KB-Infer.	Overall
	All	color	style	text	layout	All	point	interval	calculation							
Proprietary Multimodal Large Language Models																
Gemini-2.5-pro	41.97	41.04	39.87	46.33	32.23	38.72	37.21	44.23	34.36	31.41	40.92	36.73	38.81			
Gemini-2.5-flash	46.98	50.29	43.98	48.76	31.42	39.27	37.65	44.37	35.57	33.72	40.36	37.94	41.12			
GPT-4o	44.65	44.85	44.57	48.79	25.72	36.90	36.22	41.72	32.09	38.27	44.00	42.52	41.76			
Qwen-VL-Max	44.61	45.75	44.00	48.35	23.65	37.36	36.18	42.96	32.36	37.63						
Open-source Multimodal Large Language Models																
TinyChart-3B	13.95	23.82	9.14	7.62	11.38	10.95	9.05	17.63	5.79	21.11	20.95	28.36	17.41			
Llava1.5-7B	12.16	22.85	3.67	8.49	4.07	12.45	9.31	18.25	10.26	39.58	24.97	36.37	21.78			
Llava1.6-mistral-7B	20.05	27.59	10.87	18.75	17.82	21.54	17.78	22.18	26.60	23.06	30.91	31.06	23.96			
Qwen-VL-Chat-7B	16.03	17.90	8.48	17.95	19.96	12.27	11.16	17.45	7.68	35.91	32.91	34.62	23.74			
deepseek-janus-pro-7B	28.79	25.57	27.79	33.46	24.80	32.27	28.19	31.93	38.98	36.79	41.81	39.66	34.30			
MiniCPM-V2.6-8B	37.61	39.26	34.47	42.21	17.80	27.72	25.21	39.70	17.04	32.81	37.57	37.30	34.90			
InternVL3-8B	38.40	41.11	35.81	40.74	23.18	32.94	29.46	39.10	30.83	34.40	36.44	34.81	35.96			
mPLUG-Owl2-8.2B	12.61	19.31	5.77	9.30	17.77	12.47	10.54	17.71	9.12	39.82	25.91	34.39	21.95			
Pixtral-12B	37.48	36.87	33.98	41.47	32.59	28.65	24.49	31.00	32.24	33.43	43.82	41.05	36.65			
Llava1.6-vicuna-13B	21.96	30.53	10.08	21.44	19.94	13.01	11.00	20.26	7.33	37.53	32.31	36.90	26.40			
SPHINX-v2-13B	10.92	14.84	4.02	11.68	9.15	7.55	8.39	8.69	4.88	35.04	24.94	36.74	19.69			
Llama-4-Maverick-17B	33.77	31.29	29.12	40.88	25.63	30.51	28.54	30.49	33.57	34.28	42.89	41.37	35.69			
CogVLM2-19B	30.34	26.26	22.80	40.25	23.90	28.50	23.20	34.74	29.13	38.47	38.42	36.84	33.53			
Gemma-3-27B	36.28	36.12	38.20	38.98	19.84	29.71	28.08	31.41	30.19	31.90	40.04	34.11	34.74			
Llava1.6-34B	24.74	31.99	15.05	24.30	21.31	18.34	15.00	29.43	10.04	38.59	34.45	38.02	29.07			
Qwen2.5-VL-72B	42.76	43.45	42.14	46.43	25.32	37.63	36.91	42.63	32.67	36.65	42.22	40.83	40.45			
Pixtral-large-124B	43.92	45.55	42.41	46.81	27.67	39.96	36.15	44.38	40.49	37.22	47.57	43.84	42.68			
Fine-tuned																
MiniCPM-V2.6-8B-fine-tuned	53.13	54.87	54.33	54.05	36.48	38.00	37.46	43.01	32.77	35.41	46.77	41.54	44.89			

Table 10: Accuracy (%) on AstroChart benchmark using Rouge-L.

M. Details of MLLMs in Evaluation

Table 11 summarizes the architecture configurations of the current mainstream open-source MLLMs used for evaluating AstroChart, including model names, Hugging Face checkpoints (HF Checkpoint), LLM branches, and visual branches.

Models	HF Checkpoint	LLM Branch	Visual Branch
TinyChart-3B	mPLUG/TinyChart-3B-768	Phi-2	TinyChart-3B-768-siglip
Deepseek-Janus-Pro-7B	deepseek-ai/Janus-Pro-7B	DeepSeek-LLM-7b	SigLIP-L-384
Llava1.5-7B	liuhaotian/llava-v1.5-7b	Vicuna-13B	CLIP ViT-L-14-336
Llava1.6-Mistral-7B	liuhaotian/llava-v1.6-mistral-7b	Mistral-7B	CLIP ViT-L-14-336
Qwen-VL-Chat-7B	Qwen/Qwen-VL-Chat	Qwen-7B	Openclip ViT-bigG
MiniCPM-Llama3-V2.6-8B	openbmb/MiniCPM-V-2.6	Qwen2-7B	SigLip-400M
InternVL3-8B	OpenGVLab/InternVL3-8B	internlm3-8b-chat	InternViT-300M-448px
mPLUG-Owl2-8.2B	MAGAer13/mplug-owl2-llama2-7b	LLaMA-7B	ViT-L-0.3B
Llava1.6-Vicuna-13B	liuhaotian/llava-v1.6-vicuna-13b	Vicuna-13B	CLIP ViT-L-14-336
SPHINX-v2-13B	Alpha-VLLM/LLaMA2-Accessory	LLaMA2-13B	DINOv2 ViT-g14 & OpenCLIP ConvNeXt-XXL
Llama-4-Maverick-17B	meta-llama/Llama-4-Maverick-17B-128E-Instruct	Llama-4	MetaCLIP
Cogvlm2-19B	THUDM/cogvlm2-llama3-chat-19B	Meta-Llama-3-8B-Instruct	EVA2-CLIP-E
Gemma-3-27B	google/gemma-3-27b-it	Gemma3CausalLM	SigLIP-400M
Llava1.6-Yi-34B	liuhaotian/llava-v1.6-34b	Nous-Hermes-2-Yi-34B	CLIP ViT-L-14-336
Qwen2.5-VL-72B	Qwen/Qwen2.5-VL-72B-Instruct	Qwen2.5 LLM	SwiGLU
Pixtral-large-124B	mistralai/Pixtral-Large-Instruct-2411	Mistral-Large-Instruct-2407	PixtralViT

Table 11: Open-source MLLM architecture

N. Failure cases of AstroChart

Failure cases of Visual question-answer pair

Common errors in visual question-answer pair include incorrect color or pattern recognition and errors in counting or tallying (fig. 45,fig. 46, fig. 47).

Failure cases of Data question-answer pair

Common errors in data question-answer pair include misreading the numbers. (fig. 48,fig. 49, fig. 50).

Failure cases of Inference question-answer pair

Common errors in inference question-answer pairs include misinterpreting the question, providing incorrect answers, and making errors in identifying trends or comparisons. (fig. 51,fig. 52, fig. 53).

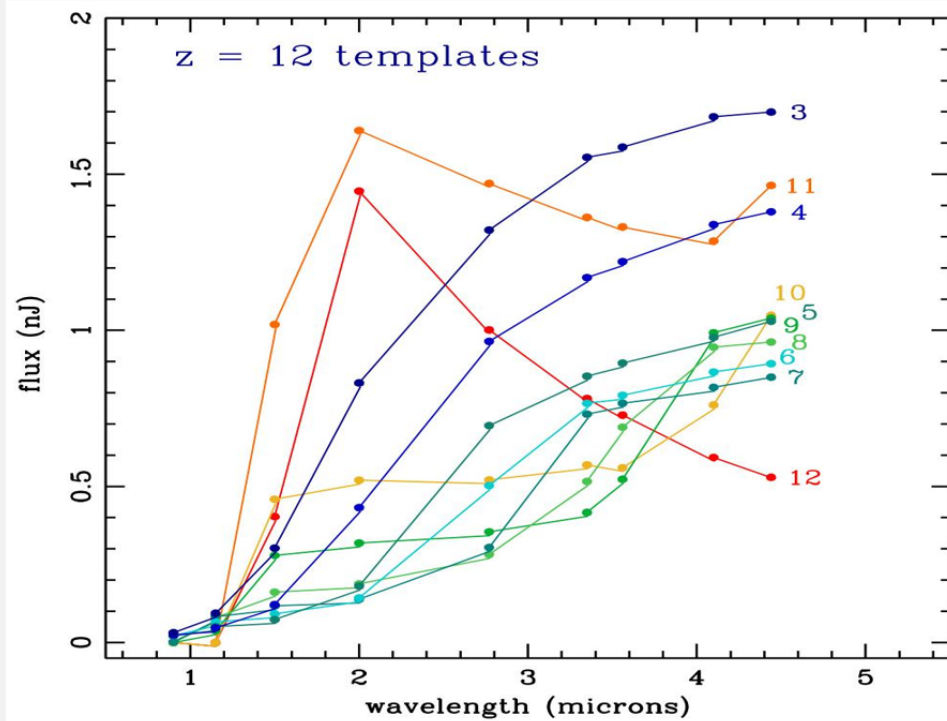
Failure cases of Chart Description question-answer pair

Common errors in chart description question-answer pair include incorrect descriptions of the chart's patterns and insufficiently comprehensive descriptions of the chart. (fig. 54,fig. 55, fig. 56).

Failure cases of KB-Inference question-answer pair

Common errors in KB-Inference question-answer pairs include incomplete or incorrect summaries of the chart content and errors or omissions in the inferred conclusions. (fig. 57,fig. 58, fig. 59).

Example



Question:

How many different colored lines are present in the graph?

Answer:

There are 10 different colored lines in the graph.

GPT-4o: There are **eight** different colored lines in the graph.

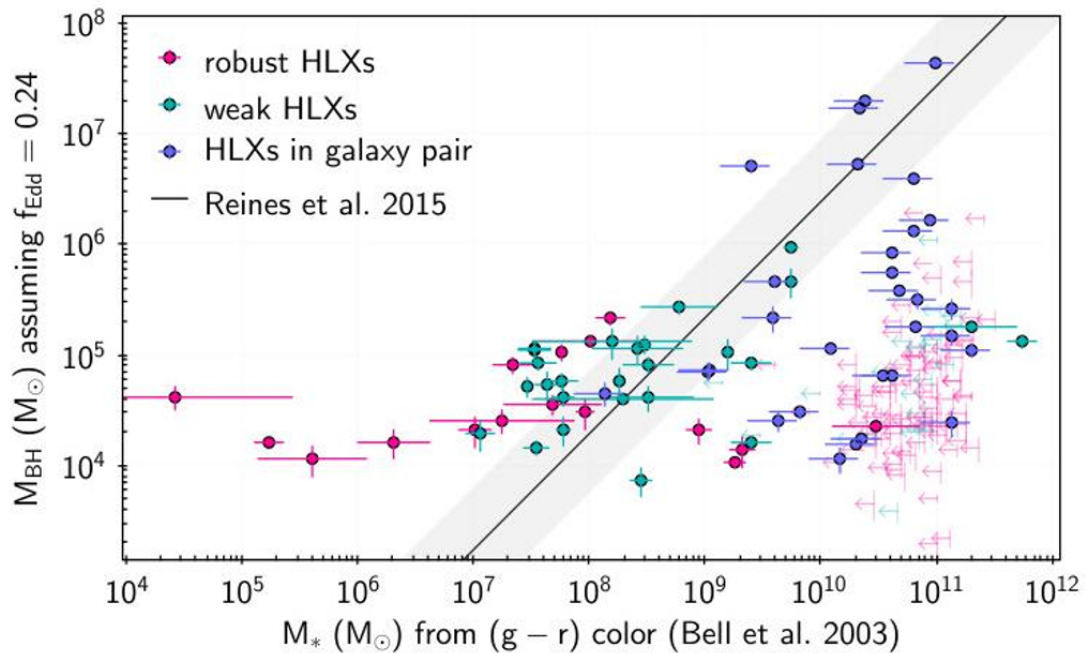
Gemini-2.5-Pro-Preview: **Nine** different colors of lines are present.

Llama-4-Maverick: There are 10 different colored lines present.

Pixtral-large: There are **12** different colored lines.

Figure 45: Failure case for visual question-answer pair generation.

Example



Question:

What are the three main colors used to represent different types of HLX candidates?

Answer:

Pink, teal, and purple.

GPT-4o: Pink, teal, **blue**.

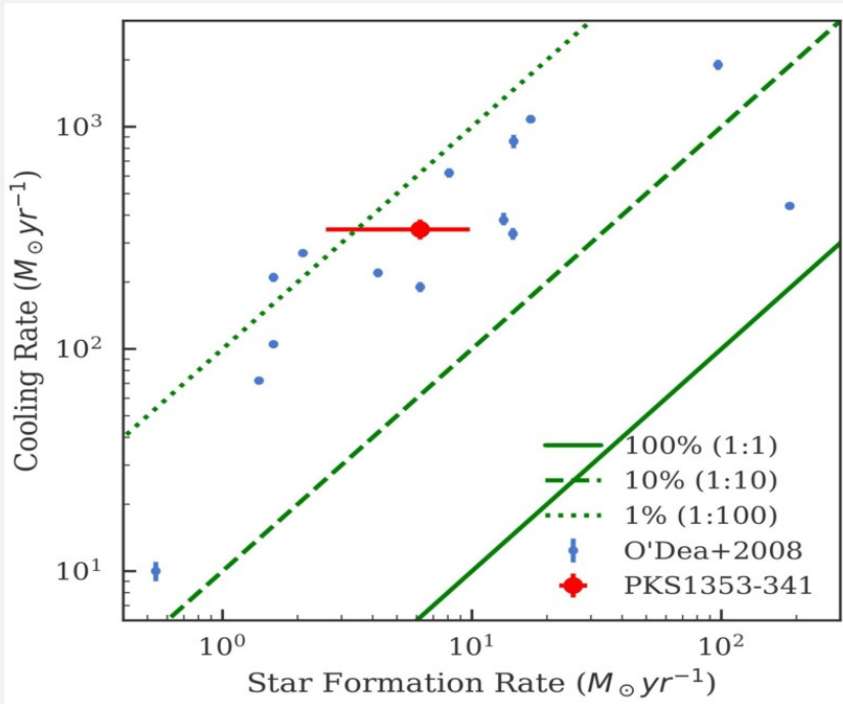
Gemini-2.5-Pro-Preview: **Magenta**, teal, and blue.

Llama-4-Maverick: The three main colors are **magenta**, teal, and blue.

Pixtral-large: Pink, teal, blue.

Figure 46: Failure case for visual question-answer pair generation.

Example



Question:

What symbols are used to represent the data points in the chart?

Answer:

Blue dots for O'Dea+2008 data, red filled circle for PKS1353-341.

GPT-4o: Blue dots and a red diamond.

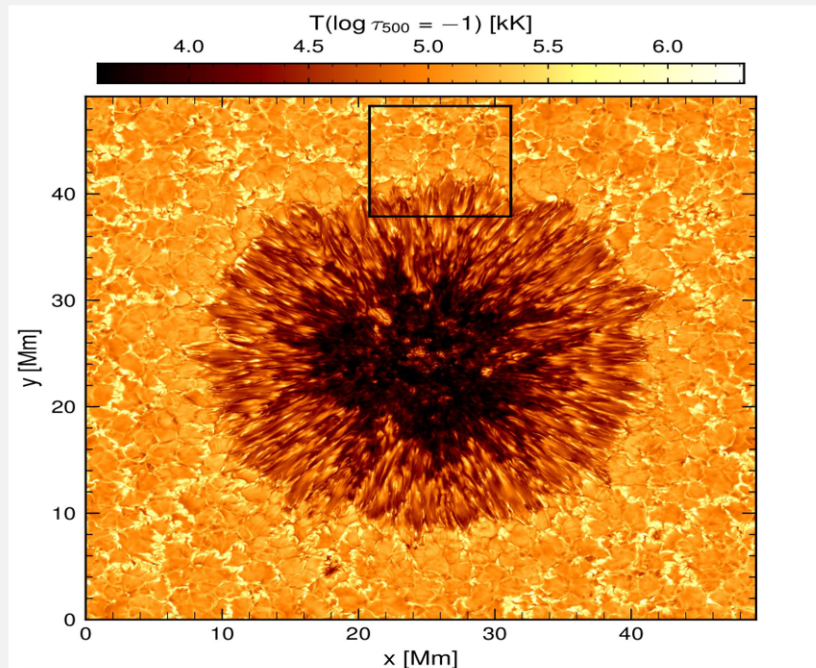
Gemini-2.5-Pro-Preview: Blue circles and red diamonds are used for data points..

Llama-4-Maverick: The data points are represented by blue dots and a red circle.

Pixtral-large: Crosses, circles and square.

Figure 47: Failure case for visual question-answer pair generation.

Example



Question:

What is the approximate temperature range in the central dark region of the sunspot?

Answer:

Between 3.7 and 4.5 kK.

GPT-4o: Approximately 4,000 to 4,500 K in the central region.

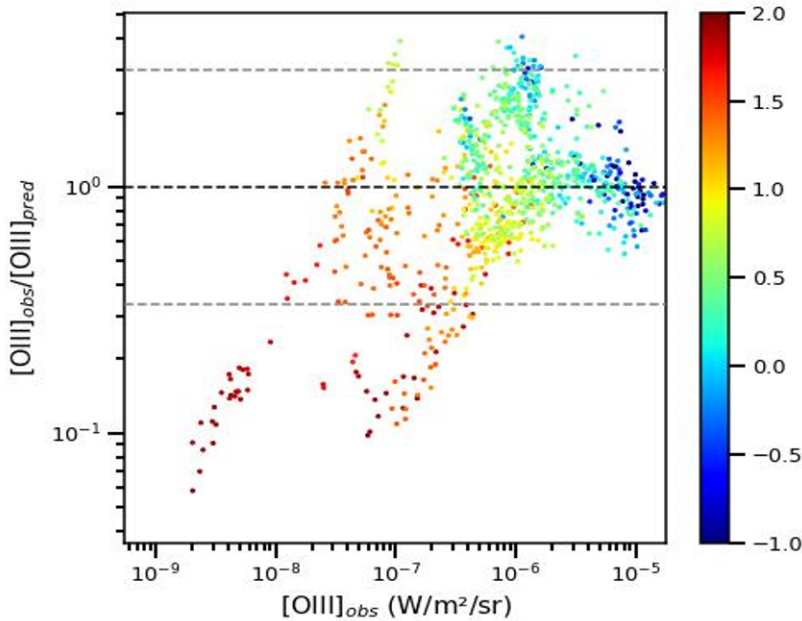
Gemini-2.5-Pro-Preview: Approximately 4.0 to 4.5 kK.

Llama-4-Maverick: The temperature range is approximately 4.0 to 4.5 kK.

Pixtral-large: Approximately 4.0 to 4.5 kK.

Figure 48: Failure case for data question-answer pair generation.

Example



Question:

What is the approximate range of values of the $[OIII]_{obs}/[OIII]_{pred}$ among all data?

Answer:

The $[OIII]_{obs}/[OIII]_{pred}$ ranges from approximately 0.05 to 40.

GPT-4o: Approximately 0.1 to 2.0.

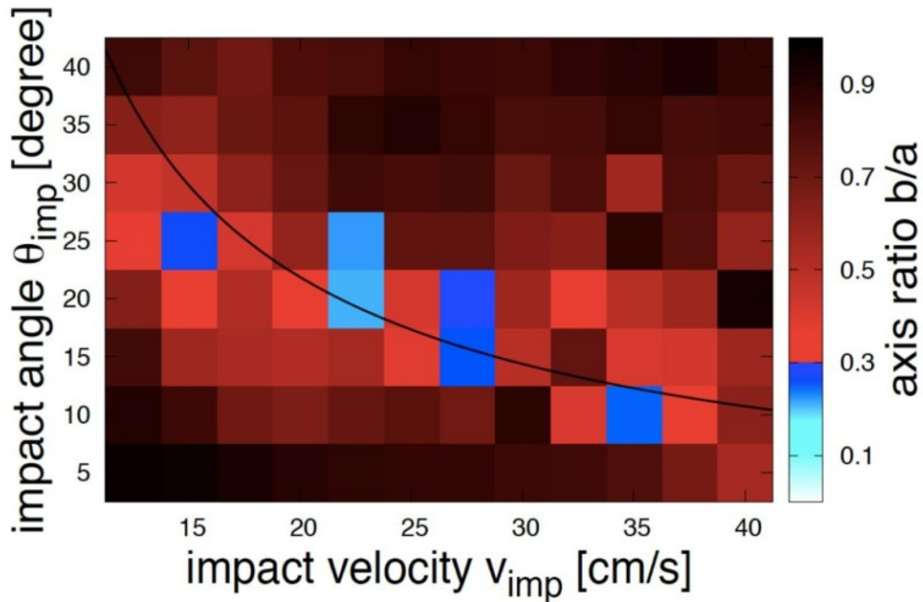
Gemini-2.5-Pro-Preview: Approximately 0.05 to 2.0.

Llama-4-Maverick: The approximate range is between 0.1 and 3.0.

Pixtral-large: Approximately 10^{-1} to 10^1 .

Figure 49: Failure case for data question-answer pair generation.

Example



Question:

At what combination of impact velocity and impact angle does the axis ratio b/a reach its lowest values?

Answer:

The axis ratio b/a reaches its lowest values at an impact angle of around 20 degrees and an impact velocity of 22.5 cm/s.

GPT-4o: The axis ratio b/a reaches its lowest values at an impact velocity of approximately 25 cm/s and an impact angle of around 25 degrees, as indicated by the darkest blue regions on the heatmap.

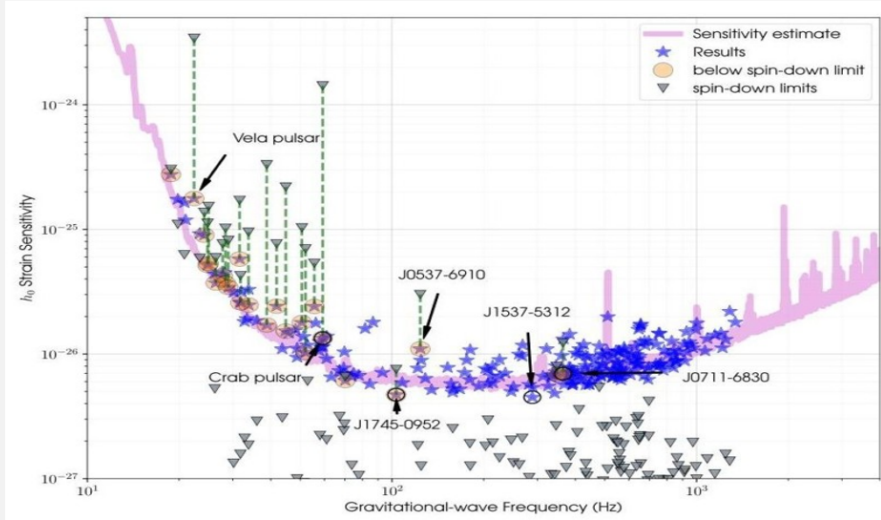
Gemini-2.5-Pro-Preview: Velocities 20 and 25 cm/s, angle 20 degrees.

Llama-4-Maverick: The lowest axis ratio b/a is achieved at moderate impact velocity and angle. Specifically, around 20-25 cm/s and 20-25 degrees.

Pixtral-large: The axis ratio b/a reaches its lowest values at an impact velocity of approximately 20-25 cm/s and an impact angle of around 20-25 degrees, as indicated by the blue regions in the heatmap.

Figure 50: Failure case for data question-answer pair generation.

Example



Question:

How does the sensitivity estimate curve compare to the majority of the results?

Answer:

The sensitivity estimate curve (pink) and the majority of the results (blue stars) essentially overlap.

GPT-4o: The sensitivity estimate curve (pink) generally **lies above** the majority of the results (blue stars), indicating that the actual results are more sensitive than the estimated sensitivity across most of the gravitational-wave frequency range.

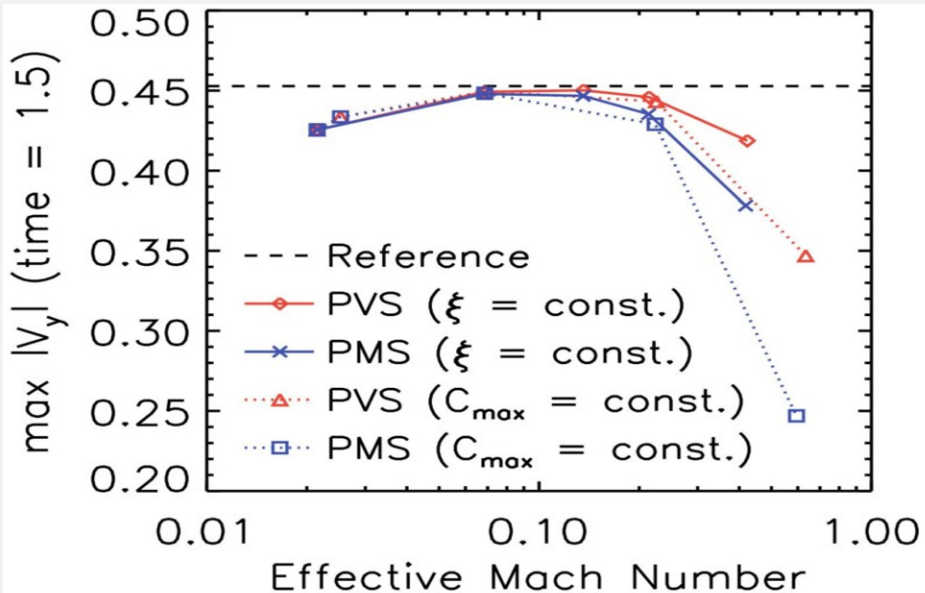
Gemini-2.5-Pro-Preview: The sensitivity estimate curve generally aligns with the lower boundary of the majority of the results, indicating it represents a good approximation of the achieved sensitivity, with most results falling at or slightly above this curve.

Llama-4-Maverick: The sensitivity estimate curve generally follows the lower boundary of the majority of the results (blue stars), indicating that it is a reasonable representation of the minimum strain sensitivity achieved. The curve closely tracks the lowest values among the results across the frequency range.

Pixtral-large: The sensitivity estimate curve generally lies **above** the majority of the results, indicating that the actual measurements (blue stars) achieved better sensitivity than the estimated limits. This is particularly evident at frequencies between 10^1 and 10^3 Hz.

Figure 51: Failure case for inference question-answer pair generation.

Example



Question:

How do the PVS and PMS curves compare at the highest Mach number?

Answer:

PVS curves have higher values than PMS curves at the highest Mach number.

GPT-4o: At the highest Mach number, both PVS and PMS curves show a significant drop, with PMS ($\xi = \text{const.}$) and PMS ($C_{\max} = \text{const.}$) having lower values compared to their PVS counterparts.

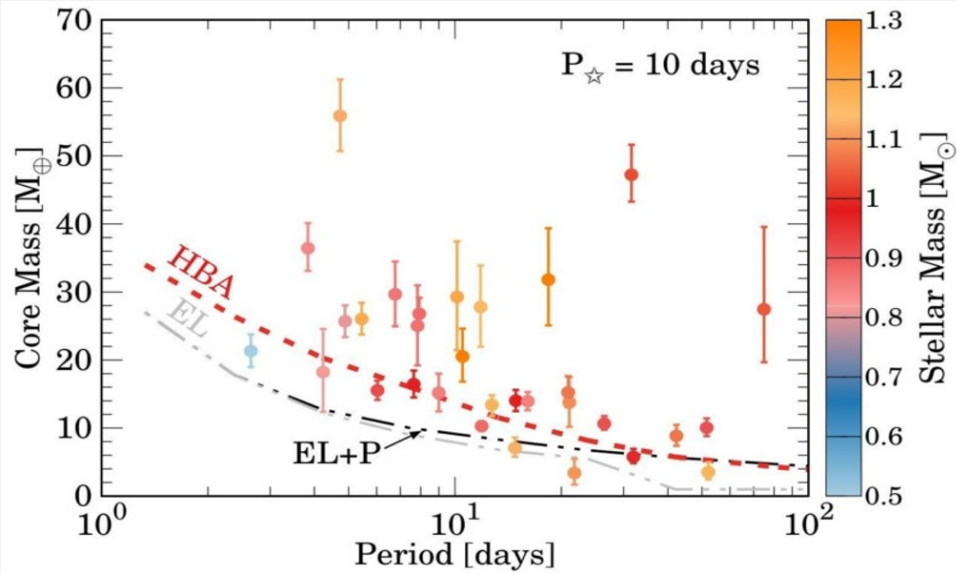
Gemini-2.5-Pro-Preview: At the highest Mach number (1.00), both PVS curves (solid red diamond and dotted red triangle) show higher $\max |V_y|$ values compared to their corresponding PMS curves (solid blue 'x' and dotted blue square). PVS ($\xi = \text{const.}$) is ~ 0.42 , while PMS ($\xi = \text{const.}$) is ~ 0.38 . PVS ($C_{\max} = \text{const.}$) is ~ 0.35 , while PMS ($C_{\max} = \text{const.}$) is ~ 0.25 .

Llama-4-Maverick: At the highest Mach number, the PVS curve is above the PMS curve. The PVS ($C_{\max} = \text{const.}$) curve is higher than the PMS ($C_{\max} = \text{const.}$) curve, indicating a difference in their behavior at high Mach numbers.

Pixtral-large: At the highest Mach number, both PVS and PMS curves show a significant drop in the maximum absolute value of velocity ($|V_y|$). The PVS curve (red triangles) drops to approximately 0.35, while the PMS curve (blue squares) drops to around 0.25, indicating that PMS experiences a more pronounced decrease. (Missing the comparison between PVS and PMS)

Figure 52: Failure case for inference question-answer pair generation.

Example



Question:

How does the EL+P model compare to the HBA model at orbital periods greater than 40 days?

Answer:

The EL+P model agrees with the HBA model at orbital periods greater than 40 days, where mass loss is mostly due to boil-off.

GPT-4o: At orbital periods greater than 40 days, the EL+P model **predicts lower core** masses compared to the HBA model, as indicated by the black dashed line being below the red dashed line.

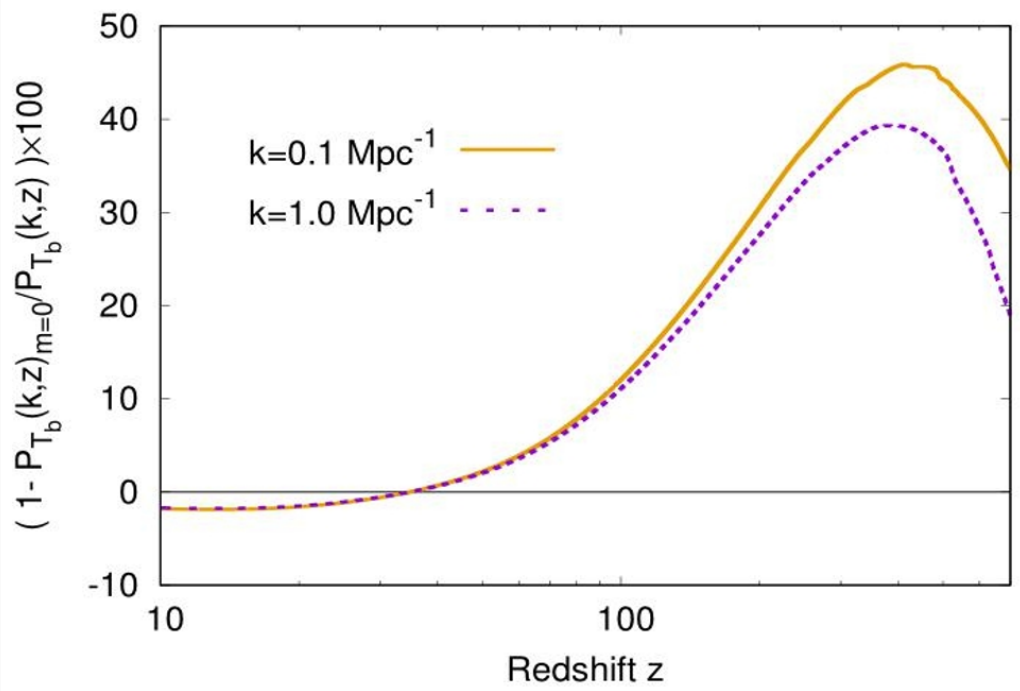
Gemini-2.5-Pro-Preview: At orbital periods greater than 40 days, the EL+P model (black dash-dotted line) **predicts lower core** masses compared to the HBA model (red dashed line). The HBA model consistently shows higher core mass predictions in this period range.

Llama-4-Maverick: The EL+P model **is below** the HBA model at orbital periods greater than 40 days, indicating that EL+P **predicts lower** core masses than HBA for longer orbital periods. The difference between the two models becomes more apparent beyond 40 days.

Pixtral-large: At orbital periods greater than 40 days, the EL+P model **predicts lower core** masses compared to the HBA model. The EL+P model's curve (black dashed line) remains below the HBA model's curve (red dashed line), indicating smaller core masses for longer periods.

Figure 53: Failure case for inference question-answer pair generation.

Example



Question:

Generate a chart description that aims at presenting all the visual elements of the plot.

Answer:

This line graph shows the redshift evolution of changes in the HI 21-cm power spectrum due to inhomogeneous CMBR heating. It compares two k -modes: 0.1 and 1.0 Mpc^{-1} . Both curves start negative at low redshifts, rise steeply after $z=100$, peak around $z=300-400$, and then decline. The lower k -mode (0.1) shows a higher amplitude and peaks later than the higher k -mode (1.0). The y-axis represents percentage change, while the x-axis uses a logarithmic scale for redshift.

GPT-4o: The chart displays the relationship between redshift (z) and the quantity $((1 - \frac{P_{T_b}(k, z)}{P_{T_b}(k, z)_{m=0}}) \times 100$). The x-axis represents the redshift (z) on a logarithmic scale from **10 to 100**, while the y-axis ranges from -10 to 50. Two curves are plotted: a solid yellow line for $(k = 0.1 \text{ Mpc}^{-1})$ and a purple dashed line for $(k = 1.0 \text{ Mpc}^{-1})$. Both curves rise from **near zero**, peak, and then decline, with the yellow curve peaking higher and later than the purple one.

Figure 54: Failure case for chart description question-answer pair generation.

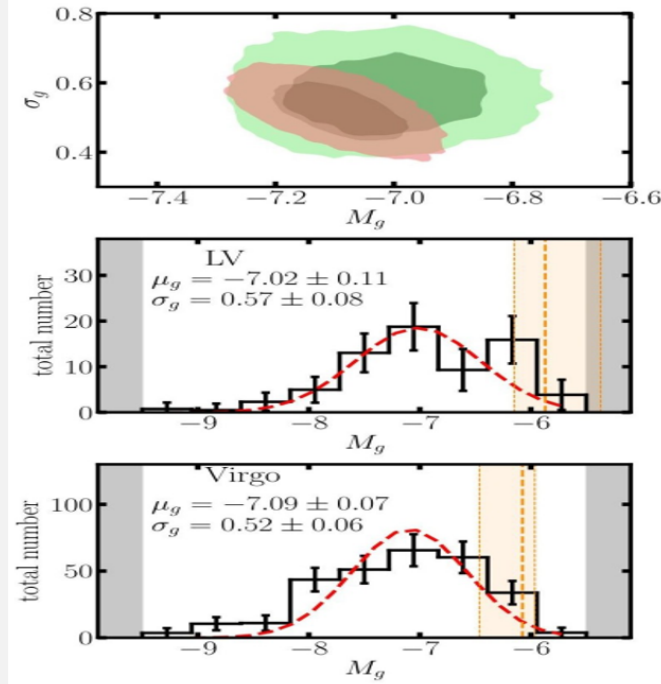
Gemini-2.5-Pro-Preview: This line plot displays two curves on a white background with black axes. The x-axis, labeled "Redshift z," is on a logarithmic scale from 10 to over 100. The y-axis, labeled "(1 - $P_{T,b}(k,z)/m=0$) * 100" ranges linearly from -10 to 50. A solid orange line represents " $k=0.1 \text{ Mpc}^{-1}$ " and a dotted purple line represents " $k=1.0 \text{ Mpc}^{-1}$ ". Both lines show a similar trend, rising from below zero, peaking, and then declining, with the orange line reaching a higher peak. A horizontal black line marks y=0.

Llama-4-Maverick: The chart displays the percentage deviation of monopole from the full power spectrum against redshift z. The x-axis represents redshift z, while the y-axis represents the percentage deviation. Two curves are shown: a solid orange curve for $k=0.1 \text{ Mpc}^{-1}$ and a dotted purple curve for $k=1.0 \text{ Mpc}^{-1}$. **Both curves start at 0%,** increase to a maximum, and then decrease. The chart provides a visual representation of the relationship between redshift and percentage deviation for different values of k within 100 words. **(Incomplete answer, missing the curve colors, line styles, or the y=0 reference line.)**

Pixtral-large: The chart is a line graph depicting the percentage change in a quantity, denoted as $(1 - P_{T,b}(k,z)/m=0) * 100$, multiplied by 100, as a function of redshift (z) on a logarithmic scale. The x-axis represents redshift (z) ranging from 10 to 1000, while the y-axis shows **the percentage** change from -10 to 50. Two data series are plotted: a solid yellow line for $k=0.1 \text{ Mpc}^{-1}$ and a dashed purple line for $k=1.0 \text{ Mpc}^{-1}$. Both lines show an increasing trend, peaking **around a redshift of 500**, and then decreasing. The chart indicates that the percentage change is more pronounced at higher redshifts and varies with the value of k.

Figure 54: Failure case for chart description question-answer pair generation. (Continued)

Example



Question:

Generate a chart description that aims at presenting all the visual elements of the plot.

Answer:

The image consists of three panels. The top panel shows overlapping contour plots for LV (green) and Virgo (red) samples, representing confidence regions for GCLF parameters. The middle and bottom panels are histograms with Gaussian fits for LV and Virgo samples respectively, showing the distribution of globular cluster magnitudes. Each histogram includes statistical information and vertical dashed lines. The overall layout compares GCLF characteristics between the two samples.

GPT-4o: The chart consists of three panels. The top panel is a contour plot showing the relationship between M_g and σ_g with three nested regions in green, brown, and red. The middle and bottom panels are histograms of M_g for LV and Virgo, respectively, with total number on the y-axis. Both histograms feature black bars with error lines, red dashed Gaussian fits, and shaded regions on the left and right. The middle panel includes text annotations for μ_g and σ_g values. The x-axis is labeled M_g and the y-axis is labeled "total number." **(Incomplete answer, missing the description of the vertical dashed lines in the histogram.)**

Figure 55: Failure case for chart description question-answer pair generation.

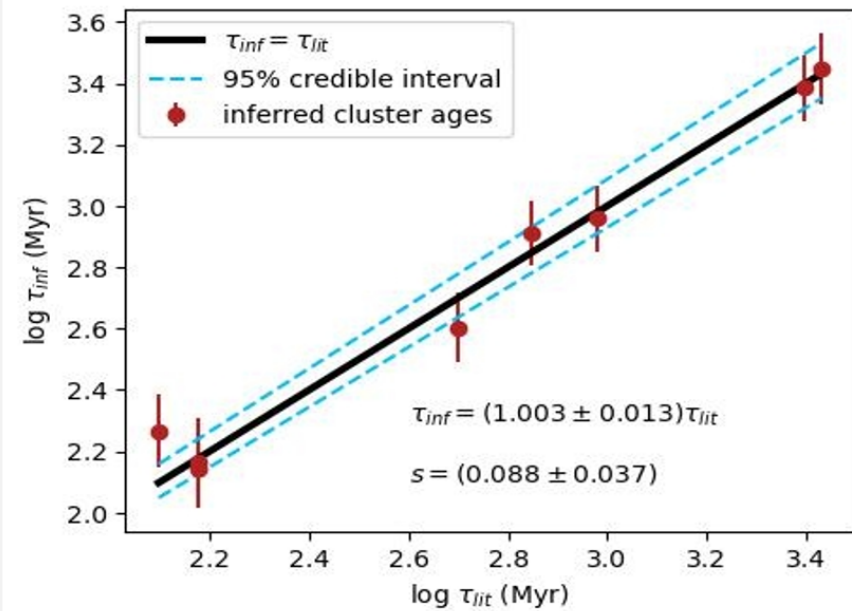
Gemini-2.5-Pro-Preview: The image contains three plots. The top plot is a 2D contour plot with `"Mg"` on the x-axis and `"\u03c3g"` on the y-axis, displaying two overlapping sets of nested, filled contours: one green, one reddish-brown. Below are two histograms, titled `"LV"` and `"Virgo."` Both plot `"total number"` against `"Mg,"` featuring black histogram bars with error bars, an overlaid red dashed curve, and text indicating `\u03bc` and `\u03c3` values. Each histogram also has grey shaded regions at its horizontal extremes and a light orange vertical band with two dashed orange lines on the right. (Incomplete answer, did not clearly indicate which samples correspond to the three panels; did not explicitly mention the purpose of comparing GCLF parameters.)

Llama-4-Maverick: The chart is a multi-panel figure showing various astronomical data. The top panel is a contour plot with green and brown contours. The middle and bottom panels are histograms with red dashed curves and error bars, displaying data for `"LV"` and `"Virgo"` respectively. The histograms have shaded regions and orange dashed lines, with annotations indicating mean and standard deviation values. The chart presents a comprehensive visual representation of the data. (Incomplete answer, did not explicitly mention the purpose of comparing GCLF parameters; did not specify the meaning of the x- and y-axes; did not explain the nested contours or their significance as confidence regions.)

Pixtral-large: The chart consists of three panels. The top panel is a contour plot showing the relationship between the absolute magnitude (Mg) and the standard deviation (σ g) for a dataset, with overlapping **green and brown** contours indicating density regions. The middle and bottom panels are histograms displaying the distribution of Mg for two different datasets labeled "LV" and "Virgo," respectively. Each histogram includes a red dashed line representing a fitted Gaussian distribution. The mean (μ g) and standard deviation (σ g) values with uncertainties are provided for each dataset. Vertical orange lines with shaded regions indicate specific ranges of interest. The histograms show the total number of occurrences for each Mg bin, with error bars indicating variability. (Incomplete answer, not clearly defining the confidence regions for the GCLF parameters.)

Figure 55: Failure case for chart description question-answer pair generation. (Continued)

Example



Question:

Generate a chart description that aims at presenting all the visual elements of the plot.

Answer:

The figure shows the accuracy of inferred cluster ages versus literature ages. The black line represents a 1:1 relationship, with the 95% credible interval in blue dashed lines and inferred cluster ages as red points.

GPT-4o: The chart is a scatter plot with a linear regression line. The x-axis represents "log τ_fit (Myr)" ranging from 2.2 to 3.4, and the y-axis represents "log τ_inf (Myr)" ranging from 2.0 to 3.6. Red dots with error bars indicate inferred cluster ages. A solid black line represents the linear fit ($\tau_{\text{inf}} = \tau_{\text{fit}}$), and two dashed blue lines show the 95% credible interval. The equation of the fit is $\tau_{\text{inf}} = (1.003 \pm 0.013)\tau_{\text{fit}}$, with a scatter (s) of 0.088 ± 0.037 . A legend in the top left corner explains the visual elements.

Figure 56: Failure case for chart description question-answer pair generation.

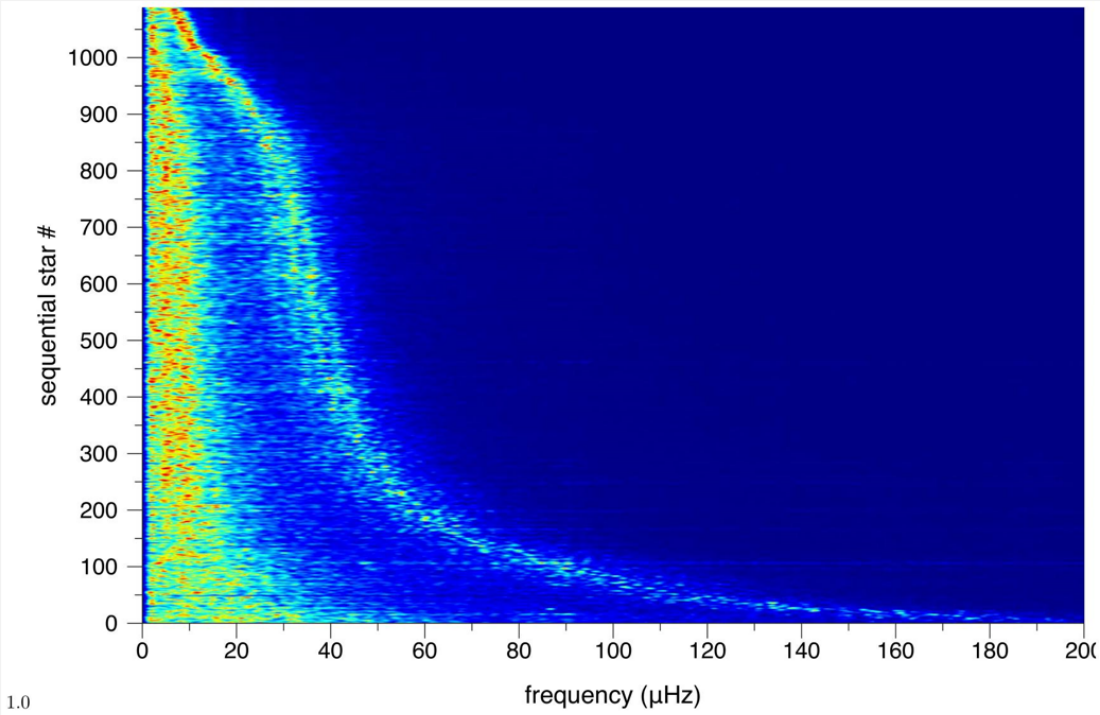
Gemini-2.5-Pro-Preview: This scatter plot presents $\log \tau_{\text{inf}}$ (Myr) on the y-axis versus $\log \tau_{\text{lit}}$ (Myr) on the x-axis, with both axes ranging from approximately 2.0 to 3.6. Six red circular markers, representing "inferred cluster ages," each feature vertical error bars. A solid black line, labeled $\tau_{\text{inf}} = \tau_{\text{lit}}$, runs diagonally. This line is flanked by two dashed cyan lines indicating the "95% credible interval." Most data points cluster near the black line. The plot also includes equations for τ_{inf} and s , and a legend in the top-left corner details these visual elements.

Llama-4-Maverick: The chart displays the relationship between $\log \tau_{\text{inf}}$ and $\log \tau_{\text{lit}}$, with a black line representing $\tau_{\text{inf}} = \tau_{\text{lit}}$. Red dots indicate inferred cluster ages, accompanied by error bars. A 95% credible interval is shown by blue dashed lines. The chart's equation, $\tau_{\text{inf}} = (1.003 \pm 0.013)\tau_{\text{lit}}$, is displayed, along with the standard deviation, $s = (0.088 \pm 0.037)$. The plot illustrates a strong positive correlation between the two variables within the 95% credible interval. (Incomplete answer, missing the details about the image structure, such as axis ranges and legend position.)

Pixtral-large: The chart is a scatter plot comparing inferred cluster ages ($\log \tau_{\text{inf}}$ in Myr) to literature ages ($\log \tau_{\text{lit}}$ in Myr). The x-axis represents the logarithm of literature ages, while the y-axis represents the logarithm of inferred ages. Red dots indicate the inferred cluster ages with error bars showing uncertainties. A solid black line represents the line of equality ($\tau_{\text{inf}} = \tau_{\text{lit}}$), and dashed blue lines denote the 95% credible interval. The plot includes an equation ($\tau_{\text{inf}} = (1.003 \pm 0.013)\tau_{\text{lit}}$) and a slope value ($s = 0.088 \pm 0.037$), indicating a close agreement between inferred and literature ages, with a slight positive bias.

Figure 56: Failure case for chart description question-answer pair generation. (Continued)

Example



Question:

How does the distribution of stellar oscillation frequencies in this image demonstrate Kepler's ability to study a wide range of stars, particularly cool main-sequence and subgiant stars?

Answer:

The image shows a concentration of oscillation frequencies between 0-60 μHz for a large number of stars (up to 1000+), indicating Kepler's capability to detect solar-like oscillations in numerous cool main-sequence and subgiant stars, which typically exhibit frequencies in this range.

GPT-4o: The image shows a wide range of stellar oscillation frequencies, indicating Kepler's capability to study diverse stars, including cool main-sequence and subgiant stars, by capturing their varied oscillation patterns effectively. (Missing the key detail that the oscillation frequencies are concentrated in the 0–60 μHz range. It also omits the scale (number of stars) and fails to mention solar-like oscillations)

Figure 57: Failure case for KB-Inference question-answer pair generation.

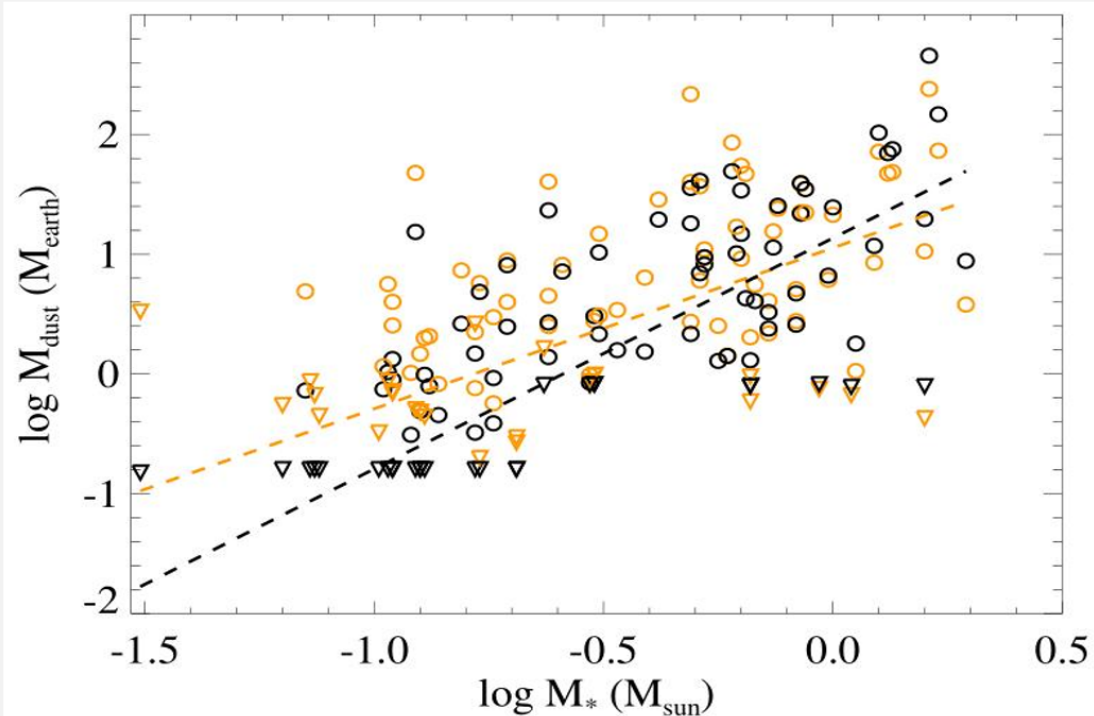
Gemini-2.5-Pro-Preview: The image displays a broad distribution of stellar oscillation frequencies across numerous stars. This continuous spread, particularly at lower frequencies characteristic of cool main-sequence and subgiant stars, demonstrates Kepler's sensitivity to detect these subtle oscillations in a diverse stellar population. **(Lacking specific details like the 0–60 μ Hz range, the number of stars observed, and the term “solar-like oscillations”.)**

Llama-4-Maverick: The image shows a diverse range of stellar oscillation frequencies, indicating Kepler's capability to study various stars. The distribution spans a wide frequency range, demonstrating its ability to analyze cool main-sequence and subgiant stars with varying oscillation characteristics. **(Overgeneralization or Lack of Specificity: Noted "various stars" without linking to cool stars.)**

Gemma-3-27B: Here's an answer within 50 words, based on the image:
The broad distribution of oscillation frequencies spanning from ~0 to 180 μ Hz shows Kepler detected signals from stars with varying sizes & temperatures. Lower frequencies indicate larger, cooler stars (subgiants/main-sequence), demonstrating Kepler's capability beyond just Sun-like stars. **(Misinterpretation of Data Trends or Ranges: Claimed "0-180 μ Hz" for stellar oscillations without distinguishing star types.)**

Figure 57: Failure case for KB-Inference question-answer pair generation. (Continued)

Example



Question:

How does the relationship between dust disk mass and stellar mass in this graph support the concept of a fragmentation-limited regime in protoplanetary disks?

Answer:

The graph shows a steeper than linear relationship between $\log M_{\text{dust}}$ and $\log M_*$, with a slope greater than 1. This indicates that dust mass increases more rapidly with stellar mass, suggesting faster radial drift in disks around lower-mass stars, consistent with a fragmentation-limited regime.

GPT-4o: The graph shows a positive correlation between dust disk mass and stellar mass, suggesting that more massive stars have more massive disks. This supports the fragmentation-limited regime concept, where disk mass is constrained by gravitational instability, leading to fragmentation in more massive disks around more massive stars. (Misinterpretation of Data Trends or Ranges: omits the key detail that the slope is greater than 1.)

Figure 58: Failure case for KB-Inference question-answer pair generation.

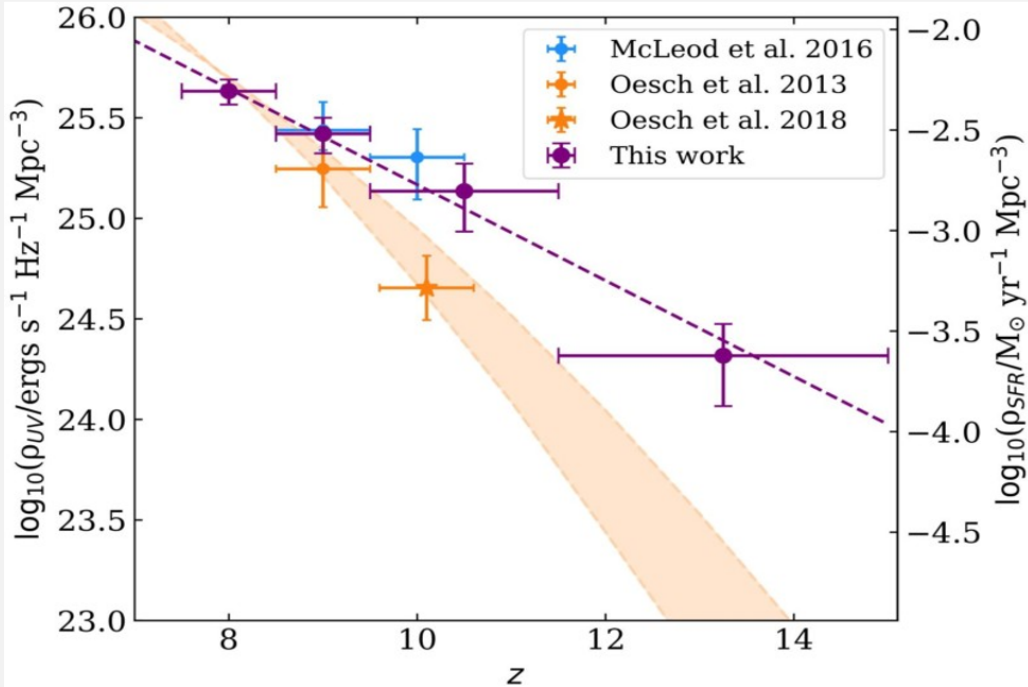
Gemini-2.5-Pro-Preview: The positive correlation between dust disk mass and stellar mass suggests that more massive stars can support more massive disks. This is consistent with a fragmentation-limited regime, where the disk's ability to accumulate mass before fragmenting is linked to the central star's properties .
(Misinterpretation of Data Trends or Ranges: omits the key detail that the slope is greater than 1.)

qwen-vl-max: The graph shows a positive correlation between stellar mass and dust disk mass, suggesting that as stellar mass increases, so does the mass of the associated dust disk. This supports a fragmentation-limited regime where disk fragmentation is influenced by the mass of the central star, affecting planet formation. **(Confusing Mechanisms or Terminology: Confused gas fragmentation with dust disk limits.)**

glm-4v-plus: The graph shows a positive correlation between dust disk mass and stellar mass, suggesting that larger stars tend to have more massive dust disks. This supports the concept of a fragmentation-limited regime, where higher stellar masses allow for more massive disks, potentially enabling planet formation through gravitational fragmentation. **(Misinterpretation of Data Trends or Ranges: Misinterpreted dust disk mass vs. stellar mass slope as "square root" instead of >1 .)**

Figure 58: Failure case for KB-Inference question-answer pair generation. (Continued)

Example



Question:

How does the trend in star formation rate density at high redshifts ($z > 8$) in this study compare to previous findings, and what implications does this have for our understanding of early galaxy evolution?

Answer:

The new data shows a more gradual decline in star formation rate density at high redshifts compared to earlier studies, particularly Oesch et al. 2018. This suggests a more continuous and steady evolution of early galaxies, rather than a rapid drop-off, providing new insights into the process of galaxy formation in the early universe.

GPT-4o: This study shows a higher star formation rate density at high redshifts ($z > 8$) compared to previous findings, suggesting **more active** early galaxy formation. This implies that galaxies formed and evolved earlier than previously thought, impacting our understanding of cosmic reionization and early universe structure formation. (Misinterpretation of Data Trends or Ranges: Does not mention comparative studies (e.g., Oesch et al. 2018))

Figure 59: Failure case for KB-Inference question-answer pair generation.

Gemini-2.5-Pro-Preview: This study finds a shallower decline in star formation rate density at $z>8$, particularly beyond $z\sim 10$, compared to some previous works. This suggests **more vigorous or earlier galaxy** formation and star buildup in the very early universe than previously anticipated. **(Overgeneralization or Lack of Specificity: The inference is somewhat vague, lacking a specific reference to "more continuous evolution.)**

Llama-4-Maverick: The trend in star formation rate density at high redshifts ($z>8$) in this study is consistent with previous findings, but with a shallower decline. This suggests that early galaxy evolution may **be more gradual than previously thought**, with implications for our understanding of cosmic reionization and galaxy formation. **(The comment mentions a discussion of GW170817 and neutron star mass limits, but this content does not appear in the answer.)**

glm-4v-plus: The trend in star formation rate density at high redshifts ($z>8$) in this study shows a decrease, consistent with previous findings. This implies that star formation was more intense in the early universe, shaping the rapid evolution of early galaxies. The consistency across studies supports the understanding of early galaxy formation processes. **(Overgeneralization or Lack of Specificity: Overemphasized age differences in clusters without explaining spatial distribution.)**

Figure 59: Failure case for KB-Inference question-answer pair generation. (Continued)

O. Expert Scoring Guidelines

Experts are provided with a chart and a corresponding QA (Question-Answer) pair, along with the domain label (e.g., Astronomy, Biochemistry). Their task is to evaluate the QA pair along two dimensions:

Domain Relevance

Assess whether the QA pair meaningfully incorporates domain-specific knowledge beyond what is explicitly presented in the chart.

- The QA should not merely restate chart labels, numbers, or trends. It should demonstrate a reasonable application of domain knowledge—such as scientific principles, expert terminology, or technical context—that complements and extends the chart’s information.
- The use of domain knowledge must be appropriate and relevant. Introducing unrelated or incorrect domain knowledge should result in a lower score.

Scoring Rubric (1–5):

- **1** – No domain knowledge, or domain knowledge is clearly incorrect.
- **2** – Slight or superficial domain knowledge; weakly relevant or only marginally extends the chart.
- **3** – Moderately appropriate domain knowledge with some depth; basic insights or moderate integration with chart content.
- **4** – Deep and precise domain knowledge, tightly connected to chart content; reflects strong understanding and expert-level reasoning.
- **5** – Domain knowledge is overly advanced or unnecessarily complex, reducing clarity or interpretability.

QA Correctness

Assess whether the question is clearly stated and whether the answer is factually correct based on the chart and relevant domain knowledge.

- The question should be unambiguous, well-formed, and directly related to the chart.
- The answer should be logically and factually grounded in the chart content, possibly incorporating appropriate domain knowledge.
- Penalize hallucinated answers, vague questions, or any factual inconsistencies with the visualized data.